STUDIES OF INTERACTIONS WITHIN SILICON AND GERMANIUM DETECTORS

by

VICTOR MARCUS PROZESKY

PROMOTER: D W MINGAY
PHYSICS DEPARTMENT

MAGISTER SCIENTIAE

COPY OF ABSTRACT

Interactions of particles, gamma rays and X-rays in silicon and germanium solid state detectors have been investigated to demonstrate the varied applicability and ease of operation of these detectors. These measurements included the calibration of intrinsic response properties of several detectors and the study of specific nuclear reactions occurring inside these detectors.

The spatial response characteristics and detection efficiency of an intrinsic germanium detector were measured as a function of energy (121-1 408 keV).

Two germanium detectors were used both as target and detector to determine the lifetime of the isomeric 0_2^+ 691 keV level of ^{72}Ge using the autocoincidence method, in which the excitation and de-excitation signals were separated electronically to generate a decay curve.

Silicon surface barrier detectors were used to calibrate 14 MeV neutron fluxes by studying yields from Si(n,particle) reactions. Detectors of different depths were studied to determine edge effects.

Finally the physical and geometric properties of four X-ray detectors were measured, including characteristic spatial dependence of charge collection efficiency.

STUDIES VAN INTERAKSIES BINNE SILIKON EN GERMANIUM DETEKTORE

deur

VICTOR MARCUS PROZESKY

PROMOTOR: D W MINGAY

FISIKA DEPARTEMENT

MAGISTER SCIENTIAE

EKSEMPLAAR VAN SAMEVATTING

Interaksies van deeltjies, gammastrale en X-strale in silikon en germanium vastetoestand detektore is ondersoek om die wye toepasbaarheid en maklike gebruik van die detektore te demonstreer. Die metings sluit die kalibrasie van intrinsieke gedragseienskappe van verskeie detektore, asook die studie van spesifieke kernreaksies wat binne die detektormateriaal plaasvind in.

Die ruimtelike responsie karakteristieke en die effektiwiteit van 'n intrinsiekegermanium(IG) detektor is gemeet as 'n funksie van energie (121 - 1 408 keV).

Twee germaniumdetektore is beide as teiken en detektor gebruik om die leeftyd van die isomeriese 0_2^+ 691 keV vlak van ^{72}Ge te bepaal. Die outokoinsidensie metode is gebruik, en die opwekking- en vervalseine is elektronies geskei om sodoende 'n vervalkurwe te genereer.

Silikonoppervlaksperlaagdetektore is gebruik om 14 MeV neutronvloed te kalibreer waar die opbrengs van Si(n,deeltjie) reaksies bestudeer is. Detektore met verskillende aktiewe diktes is gebruik om randeffekte te bestudeer.

Laastens is die fisiese en geometriese eienskappe van vier X-straal detektore gemeet, wat die karakteristieke ladingsversameling effektiwiteit as 'n funksie van posisie insluit.

ACKNOWLEDGEMENTS

I am very grateful to the following people:

Dr D W Mingay for his leadership, indispensable advice and motivation. His enthusiasm and knowledge of the subject will always be an encouragement to me.

Prof E K H Friedland who acted as promoter of this thesis.

All the members of the **Van de Graaff group** at Pelindaba for all the fruitful discussions, advice and assistance.

Mrs Susan Human for the endless patience and deciphering skills in typing this thesis.

Miss Danielle Mitton for adding the finishing touches to the final typing.

The **AEC** for giving me the opportunity to undertake further study, and for the concession allowing me to attend the lectures during the theoretical part of the degree.

My wife **Frances** for her love, support and enthusiasm throughout the study.

To **God** for the privilege to study such a beautiful subject.

ABSTRACT

Interactions of particles, gamma rays and X-rays in silicon and germanium solid state detectors have been investigated to demonstrate the varied applicability and ease of operation of these detectors. These measurements included the calibration of intrinsic response properties of several detectors and the study of specific nuclear reactions occurring inside detectors.

The spatial response characteristics of an intrinsic germanium (IG) detector were measured. The gamma ray detection efficiency was scanned as a function of position of irradiation from 121 to 1 408 keV for illumination of both the front face and side of the detector using a collimated photon beam (^{152}Eu). Theoretical calculations of intensity profiles of collimated photon beams were used to optimise the choice of thickness of collimator material and aperture diameter. Results showed definite regions of irregular response and also indicated that the active volume of the detector was not situated in the centre of the detector holder. This study included a compilation of precision data relating to the energies and intensities of the ^{152}Eu source used for efficiency calibration. A semi-empirical function was fitted to the efficiency data with excellent results.

A lithium drifted germanium detector (Ge(Li)) and an intrinsic germanium (IG) detector were used each as target and detector to determine the lifetime of the 691 keV 0_2^+ state of ^{72}Ge. The level was excited by inelastic neutron scattering using an Am/Be source. The autocoincidence method of lifetime determination was used in which the time differential between the excitation and de-excitation signals was measured electronically. The time to pulse height converted spectrum was analysed and the decay data fitted with non-linear least squares fits. The measured half life of 437±5 ns compares favourably with values previously obtained.

Silicon surface barrier detectors were used to study 14 MeV neutron induced reactions in silicon. These detectors were used to monitor 14 MeV neutron fluxes by measuring the yields from Si(n,α) and Si(n,p) reactions. Contributions from the different naturally abundant isotopes of silicon were identified and optimisation of the experimental configuration determined. Detectors with different depletion depths were examined and the feasibility of using cheaper (100 µm deep) detectors instead of more expensive (1 000 µm) detectors evaluated. Edge effects related to the escape of charged particles (especially protons) from the active volume of these detectors were theoretically calculated and compared favourably with measured values.

Finally the physical properties of four X-ray detectors were measured to establish the agreement between values specified by manufacturers and measured values as well as the efficiencies of these detectors. These measurements focussed on the determination of the distance from detector window to crystal face, the active areas of detectors which were determined by scanning these detectors with collimated photon beams and the sensitive depths of the two silicon detectors. Measured values were shown to be different in general from nominal values provided by the manufacturers, confirming that experimental verification of physical parameters is essential if precise detector calibration for application in, inter alia, PIXE studies is to be achieved.

SAMEVATTING

Interaksies van deeltjies, gammastrale en X-strale in silikon- en germanium vastetoestand detektore is ondersoek om die wye toepasbaarheid en maklike gebruik van dié detektore te demonstreer. Die metings sluit die kalibrasie van intrinsieke gedragseienskappe van verskeie detektore, asook die studie van spesifieke kernreaksies wat binne die detektormateriaal plaasvind in.

Die ruimtelike responsie karakteristieke van 'n intrinsiekegermanium (IG) detektor is gemeet. Die gammastraaleffektiwitiet is bepaal as 'n funksie van posisie deur die detektor met gamma-energieë van 121 keV tot 1 408 keV te skandeer. Sowel die voorkant as die sy van die detektor is ondersoek. Gekollimeerde fotobundels is gebruik en teoretiese berekenings van die intensiteitsprofiele is gebruik om die dikte van die absorbeerder en grootte van die kollimatoropening te optimeer. Die resultate dui op definitiewe areas waar die responsie onreëlmatig is, en ook dat die kristal nie gesentreer is ten opsigte van die detektorhouer nie. Die studie sluit 'n verwerking in van noukeurige metings van energieë en intensiteite van gammastrale afkomstig van 'n ^{152}Eu-bron wat gebruik is om die effektiwiteit van die detektor te kalibreer. 'n Semi-empiriese passing is gebruik om die data te pas, met uitstekende resultate.

'n Germaniumdetektor, met litium gedryf, (Ge(Li)), en 'n intrinsieke-germanium detektor is gebruik beide as teiken en detektor om die leeftyd van die isomeriese 0_2^+ vlak van ^{72}Ge te bepaal. Die vlak is opgewek deur onelastiese neutronverstrooiing vanaf 'n ^{241}Am/Be-bron. Die outokoinsidensie metode van leeftydbepaling is gebruik waar die tydsverskil tussen opwekkings- en vervalseine elektronies gemeet is. Die spektrum van pulse wat omgeset is van tyd- na- pulshoogte is geanaliseer en die vervaldata gepas met nie-lineêre kleinste kwadraat passings. Die gemete halfveertyd van 437 ± 5 ns vergelyk goed met waardes voorheen gemeet.

Silikonoppervlaksperlaagdetektore is gebruik om reaksies geïnduseer deur 14 MeV neutrone in silikon te bestudeer. Die detektore is gebruik om die 14 MeV neutronvloed te monitor deur die opbrengs van Si(n,α)- en Si(n,p)-reaksies te bestudeer. Bydraes van die verskillende natuurlike isotope van

silikon is identifiseer en die optimering van die opstelling bepaal. Detektore met verskillende verarmingsdiktes is gebruik en die implikasies vir die gebruik van goedkoper (100 µm-) detektore in die plek van duur (1000 µm-) detektore is bestudeer. Randeffekte te wyte aan deeltjies (veral protone) wat uit die kristal ontsnap, is teoreties bereken en het goed vergelyk met gemete waardes.

Laastens is die fisiese eienskappe van vier X-straal detektore gemeet om die geldigheid van waardes verskaf deur die vervaardigers te toets, asook om die effektiwiteit van die detektore te bepaal. Die metings het gefokus op die afstand van die ingangsvenster na die kristal, die aktiewe groottes is bepaal deur middel van skandering met gekollimeerde fotonbundels, en die aktiewe dikte van die twee silikondetektore is bepaal. Resultate verskil in die algemeen van nominale waardes deur die vervaardigers verskaf, en bevestig dat fisiese parameters eksperimenteel getoets moet word alvorens detektore presies gekalibreer kan word vir, onder andere, PIXE studies.

TABLE OF CONTENTS

TABLE OF CONTENTS

TABLE OF FIGURES

Page

TABLE OF TABLES

1 INTRODUCTION

The use of semiconductor detectors has become invaluable in any nuclear or atomic physics laboratory. Knowledge of the detector system is required to determine the regions of applicability, optimal exploitation and associated accuracy of results. At Pelindaba a large range of low energy nuclear and atomic physics studies is pursued, and germanium and silicon detectors feature very prominently as detector systems in low energy experiments. In addition to basic studies, more and more attention is paid to application of these techniques to, inter alia, gammametric scanning of fuel pin elements and neutron flux monitoring. Associated with gamma ray measurements in neutron fluxes are associated detector effects caused by inelastic neutron scattering. It became appropriate to embark on a study of various applications and calibration and characterisation of these detectors.

These studies therefore entail detector characterisation in terms of its pure application for conventional detection of radiation as well as specialised cases where such detectors were used to study nuclear reactions induced in the detector material. These specialised cases are illustrated by results relating to the use of silicon surface barrier detectors for the study of the Si(n,p)Al and Si(n,α)Mg reactions for fast neutron flux determination and by determination of the lifetime of an isomeric state of ^{72}Ge excited within a germanium gamma ray detector. In both these studies the detectors were used both as target and detector.

The efficiency of X-ray and gamma detectors is the most important feature of photon detection in nuclear and atomic physics experiments, and this efficiency was measured for various photon detectors. Besides this efficiency response of such detectors, several other intrinsic parameters of these detectors were studied. It is shown that physical parameters specified by manufacturers of these detectors, such as physical size and position measured of several X-ray and gamma ray detectors, are not always accurate.

2 RESPONSE CHARACTERISTICS OF AN INTRINSIC GERMANIUM DETECTOR

2.1 Introduction

The use of intrinsic germanium (IG) and lithium drifted germanium (Ge(Li)) detectors for the detection of electromagnetic radiation is now standard practice throughout the world. These detectors superseded sodium iodide (NaI(Tl)) detectors primarily because of their improved energy resolution (typically 2 keV rather than 60 keV at 1 MeV). Two disadvantages of these germanium detectors are the smaller efficiency for detecting photons with respect to NaI(Tl) detectors, and the fact that they have to be operated at liquid nitrogen temperatures. In addition, Ge(Li) detectors must be kept cold as the lithium would diffuse from the crystal at higher temperatures. A few years ago Ge(Li) detectors had an advantage with respect to the IG detectors due to the availability of bigger crystals, leading to higher counting efficiency. This situation has changed with time and large volume IG detectors are now available.

In terms of detection efficiency, the germanium detectors are usually[Ie72] quoted in terms of detection efficiency relative to that of a 3" x 3" NaI(Tl) detector for 1,33 MeV gamma rays from a ^{60}Co source for a fixed source-detector distance of 25 cm from the front face of the detector. This distance actually refers to the capsule in which the detector crystal is situated, and not to the distance from the source to the crystal itself. It is however possible to determine the position of the detector crystal with respect to the holder. This efficiency figure is, in addition, a global figure and does not contain any information concerning the response of the detector as a function of position, that is the position of the crystal with respect to holder, or the response from different parts of the crystal, or for that matter, critical dimensions of the ingot.

There are basically two types of detectors, namely co-axial and planar, the former having cylindrical symmetry about the core axis of a cylindrical ingot, and the latter being of the "parallel plate" variety as depicted in Fig. 2.1. While the geometry and field strengths from applied bias voltage of the latter are normally better defined, the first type is frequently selected since it exhibits better fast timing characteristics, which is often a required parameter in measurements.

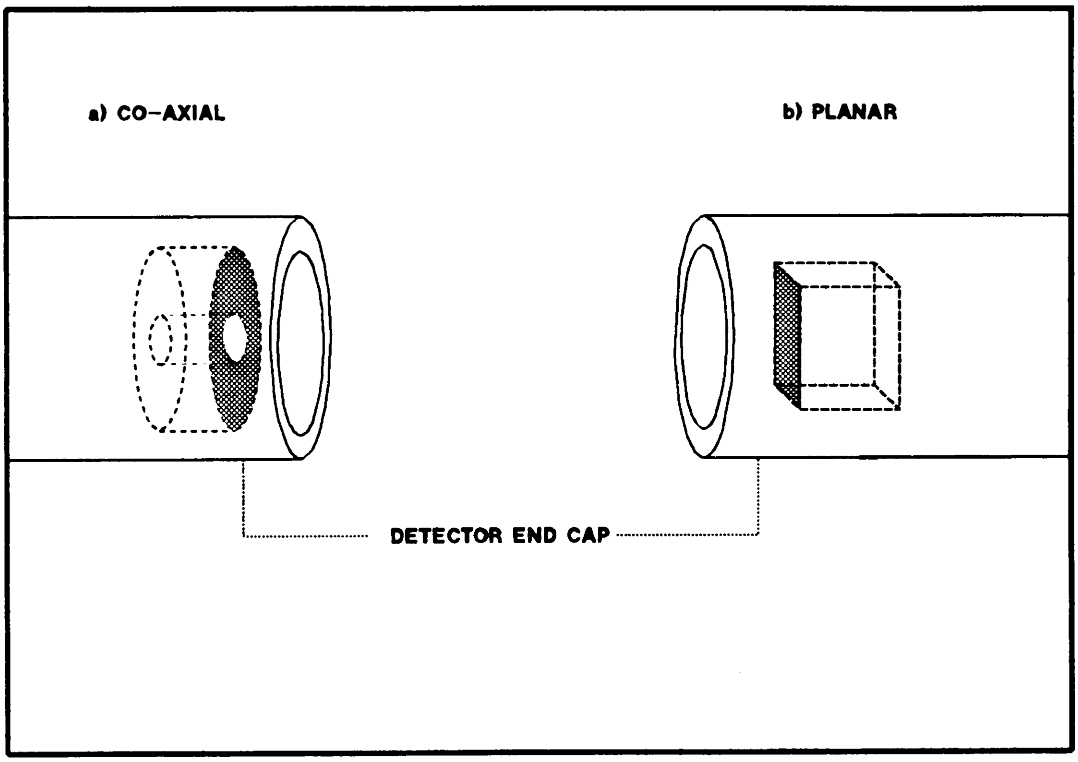

Fig. 2.1

Co-axial and planar geometries in germanium detectors

2.2 Experimental

An IG detector (nominally 18 % efficiency, 1,80 keV resolution at 1,33 MeV) was purchased in order to scan fuel pin assemblies following irradiation at the SAFARI-1 reactor at Pelindaba, for which detection characteristics had to be established prior to application. A requirement was to study the relative efficiencies for detection of gamma rays between 100 keV and 1,5 MeV (these energies are usually the most suitable range for nuclide identification and quantification) for both the side looking and the more conventional front face detector geometry in order to establish the optimum configuration. The experimental arrangement is shown in Fig. 2 where the detector is shown to be used in the side looking configuration. Different parameters required study, which included the fundamental absorption effect of the difference in thickness of the end cap when looking from the side (1,0 mm and θ dependent) and front (0,5 mm) of the detector.

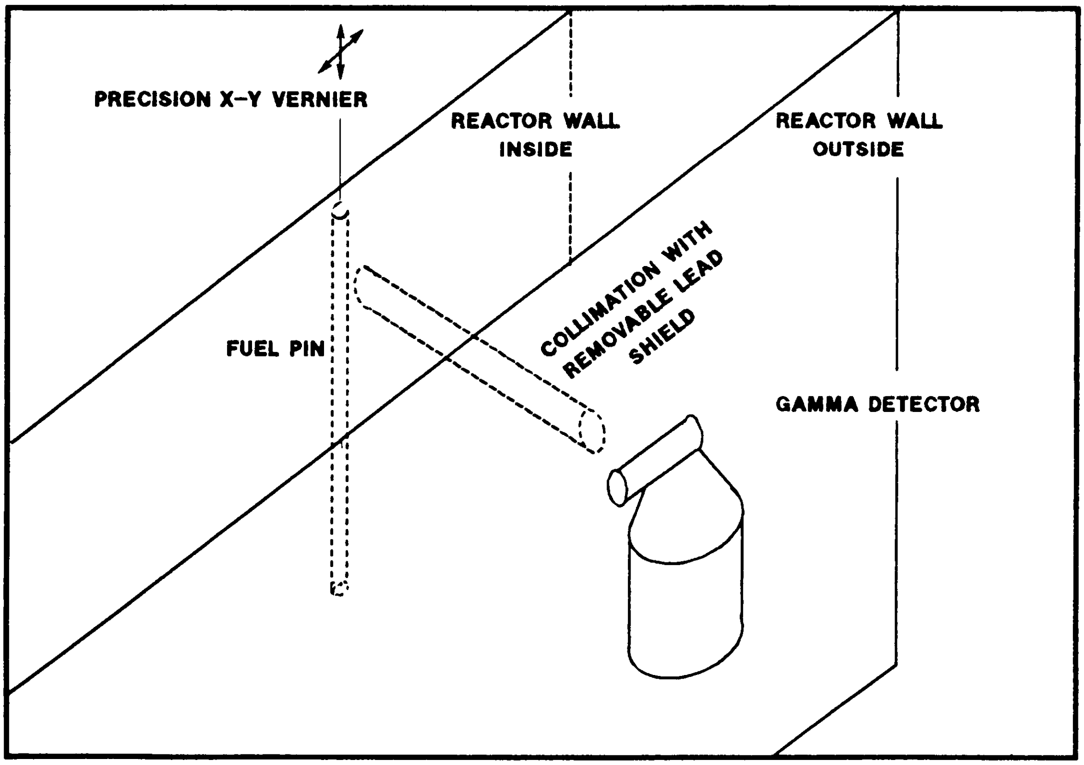

Fig. 2.2

Experimental arrangement to scan fuel pin assemblies

A more detailed study of the energy dependent detection efficiency as a function of position was undertaken using a ^{152}Eu source to establish the exact size and position of the germanium ingot as well as the relative response for different photon energies. The measurement for different photon energies is essential since the mean interaction depth increases with photon energy. The contribution of edge effects was also considered in this endeavour. It was aimed to deduce also any effects of incomplete charge collection at the edges of the detector in the region where the electric field is distorted or non-uniform.

Finally a study of the normal background contribution in the reactor environment was made to identify possible interference between background peaks and peaks in spectra being studied.

The efficiency and background measurements were done in situ at the SAFARI-1 reactor while the spatial measurements of the detector were executed in an area well isolated from the reactor environment.

2.3 Intensities of the ^{152}Eu transition

While ^{60}Co sources are traditionally[Ie72] used for the definition of absolute efficiency and energy resolution, ^{152}Eu sources are usually used for energy and relative efficiency calibration since they provide several well defined intense transitions in the range 121 keV to 1 408 keV. These may be compared with the two well known lines of ^{60}Co (1,173 and 1,332 MeV). This led at the outset to the extended literature study of the relative intensities of the different lines of this source to include the most up to date measurements in order to yield the most accurate calibration. The intensities of the lines in the ^{152}Eu spectrum were measured extensively in the past[La76,Ja77,Le78,De79,Hn79,Yo80] which reflects on the widespread application of the good calibration characteristics of the nuclide for general gamma ray spectroscopy. A typical spectrum which was measured with a 10 μC ^{152}Eu source is shown in Fig. 2.3 and shows the many characteristic lines in the spectrum. Recent new energy measurements made by Warburton and Alburger[Wa86] as well as by Meyer[Me78] have been included in order to establish the most accurate relative energy values of peaks for energy calibration of the IG detector.

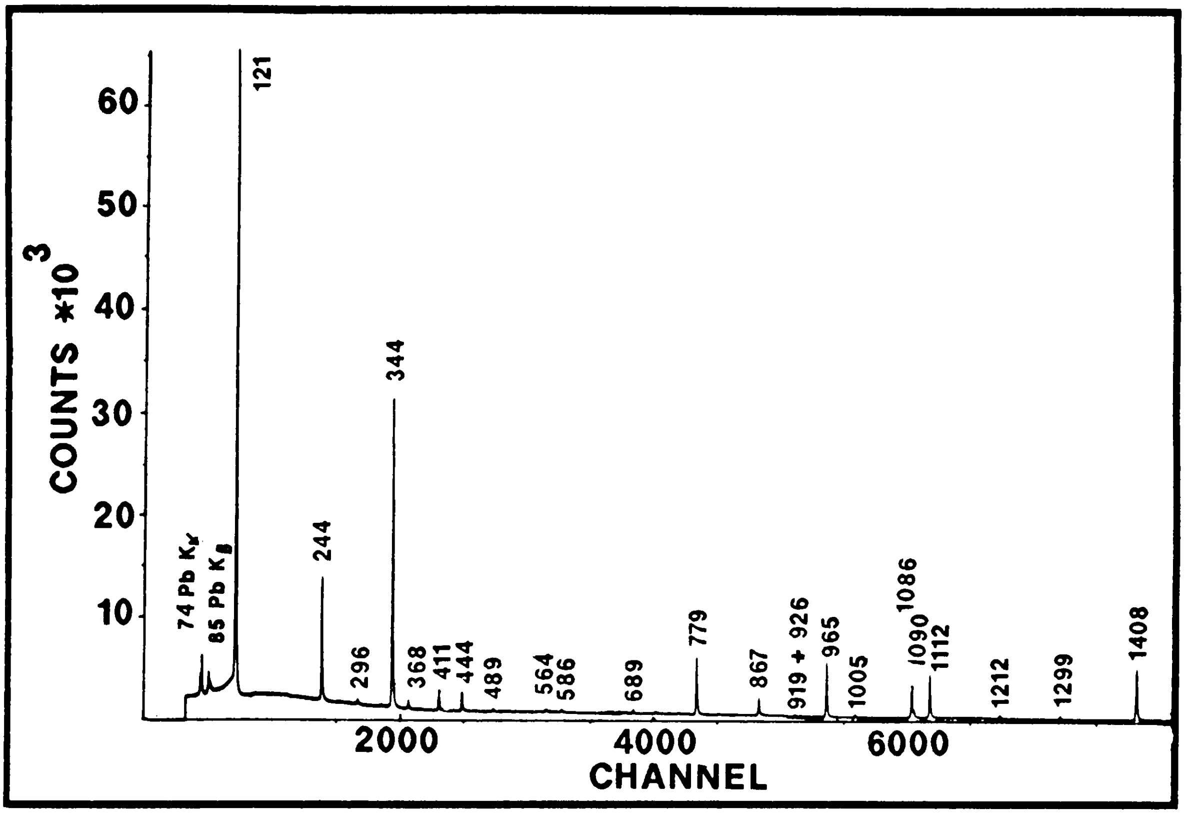

Fig. 2.3

A typical gamma ray spectrum of ^{152}Eu as measured with the IG detector

(Energies in keV)

Tabel 2.1
Relative intensities of the different lines of ^{152}Eu

Energy (keV)			Relative intensities: Normalized to 1 408 keV							
Wa86	Me78	Ave	La76	Ja77	De79	Yo80	Hn79	Le78	Ge77	Ave
		121,78[La76]	136,2	-	136,1	-	136,5	136,2	141	137,2
		244,69[La76]	35,8	-	36,0	-	36,8	35,8	36,6	36,2
251,635(10)	251,628(10)	251,632	-	-	-	-	-	0,30	-	0,30
295,921(15)	295,939(8)	295,930	2,043	2,088	-	2,14(4)	2,06	2,11	-	2,09
		329,4[Ja77]	-	0,702	-	0,711(14)	-	0,59	-	0,67
344,283(3)	344,276(4)	344,280	127,6	126,3	127,5	127,9(6)	127,4	127,5	127,2	127,34
367,797(6)	367,789(5)	367,793	4,06	4,11	-	4,16(4)	4,15	4,05	4,19	4,12
411,126(3)	411,115(5)	411,121	11,11	10,83	10,71	10,90(5)	10,83	10,7	10,71	10,83
		416,04[La76]	-	-	-	-	-	0,53	-	0,53
443,971(3)	443,976(5)	443,974	14,86	15,05	14,97	15,06(6)	14,75	14,8	15,00	14,93
488,684(6)	488,661(39)	488,673	-	2,039	-	2,031(15)	1,96	1,95	1,984	1,99
503,470(9)	503,387(5)	503,429	-	0,774	-	0,768(18)	-	0,73	-	0,76
563,997(7)	564,021(8)	564,009	-	2,436	-	2,43(4)	2,29	2,36	-	2,38
566,439(12)	566,421(8)	566,430	2,96	-	-	0,64(6)	-	0,62	-	0,63
586,273(9)	586,294(6)	586,283	-	2,184	-	2,19(0,08)	-	2,20	2,24	2,20
656,492(5)	656,484(12)	656,488	-	0,703	-	0,71(5)	-	0,69	-	0,70
671,158(18)	671,151(20)	671,155	-	-	-	-	-	-	-	-
674,685(7)	674,678(3)	674,682	-	0,934	-	0,94(5)	-	0,89	-	0,92
678,623(5)	678,578(3)	678,601	-	2,273	-	2,28(5)	2,28	2,21	2,296	2,27
688,674(5)	688,678(6)	688,676	4,10	4,19	-	4,20(4)	4,05	4,00	4,12	4,11
719,355(6)	719,353(6)	719,354	-	1,67	-	1,67(3)	1,52	1,56	-	1,61
		764,8[Ja77]	-	0,952	-	0,95(5)	-	0,84	-	0,91
		778,90[La76]	62,81	62,05	62,16	62,16(22)	60,07	61,9	62,6	61,86
810,458(9)	818,0459(7)	810,459	-	1,566	-	1,56(4)	-	1,52	-	1,55
841,578(10)	841,586(8)	841,582	-	0,838	-	0,836(23)	-	0,78	-	0,82

Energy (keV)			Relative intensities: Normalized to 1 408 keV							
Wa86	Me78	Ave	La76	Ja77	De79	Yo80	Hn79	Le78	Ge77	Ave
867,384(8)	867,388(8)	867,386	20,10	20,30	-	20,33(10)	19,88	19,9	20,54	20,18
		901,2[Ja77]	-	0,402	-	0,40(5)	-	0,44	-	0,41
919,369(19)	919,401(8)	919,385	-	2,07	-	2,08(6)	-	2,09	-	2,08
		926,2[Ja77]	-	1,376	-	1,38(6)	-	1,27	-	1,34
		930,5[Ja77]	-	0,369	-	0,37(6)	-	0,35	-	0,36
964,065(6)	964,131(9)	964,098	70,0	69,8	70,12	70,14(23)	69,66	69,2	70,4	69,90
		1005,1[Ja77]	-	3,43	-	3,078(24)	3,35	3,10	3,57	3,31
1085,846(11)	1085,914(13)	1085,880	57,2	48,1	48,73	48,15(16)	48,29	46,5	48,7	48,08
1089,767(14)	1089,700(15)	1089,734	-	8,32	-	8,35(4)	8,14	8,2	8,26	8,25
		1109,2[Ja77]	-	0,992	-	1,00(5)	-	0,88	-	0,96
1112,089(10)	1112,116(17)	1112,103	65,5	64,4	65,04	64,67(21)	64,24	64,9	65,0	64,82
1212,970(13)	1212,950(12)	1212,960	6,71	6,84	-	6,85(5)	6,69	6,70	6,67	6,74
		1249,9[Ja77]	-	0,876	-	0,875(24)	-	0,88	-	0,88
		1292,86[La76]	8,42	-	-	0,46(3)	-	0,49	-	0,48
1299,152(9)	1299,124(12)	1299,138	-	7,79	-	7,80(5)	7,75	7,8	7,76	7,78
1408,013(6)	1408,011(14)	1408,012	100	100	100	100,0(3)	100	100	100	100
1457,620(21)	1457,628(15)	1459,624	-	-	-	2,391(29)	2,38	2,33	2,52	2,41
		1528,1[Ja77]	-	1,35	-	1,346(13)	1,47	1,27	-	1,36

The results of the intensity analysis are shown in Table 2.1. In total 43 lines are reported with an energy interval between peaks of less than 120 keV in the energy range 121 keV to 1 528 keV. The biggest gap in this range is between the 121 keV and 244 keV peaks. There is no other standard source that provides such an extensive range of energies. It should be noted however that not all of these peaks are suitable for energy calibration as there are doublets (e.g. 1 085 keV and 1 089 keV) low intensities (e.g. 1 292 keV) and interference from ambient background peaks (e.g. 1 457 keV peak with natural background peak of ^{40}K at 1 460 keV), which make using some peaks impractical. Such peaks were excluded from general use.

The most suitable peaks for energy calibration of a gamma ray detector are shown in Table 2.2, with some possible disqualifying remarks. Peaks that were used for energy calibration and efficiency purposes are indicated with an asterisk.

Table 2.2

Peak energies and intensities used for energy calibration purposes

E (keV)	Intensity (Rel)	Remarks
121,78	137,2	*
244,69	36,2	*
295,930	2,09	Low intensity
344,280	127,34	*
411,121	10,83	416,04 keV line interferes
443,974	14,93	*
778,90	61,86	*
867,386	20,18	*
964,098	69,90	*
1112,103	64,82	*
1212,960	6,74	*
1408,012	100,00	*

* Most useful peaks for energy calibration

These results now represent the most recently established standard values in use at the Van de Graaff accelerator facility at Pelindaba for precision efficiency calibration of gamma ray detectors and were used to obtain an accurate relative efficiency calibration of the co-axial IG detector used.

2.4 Counting efficiency calibration of IG detector

The measurements for the determination of energy and efficiency were done with the simple electronic circuit illustrated in Fig. 2.4. No pulse shape rejection was used in order to remove non-standard pulse shapes which are associated with detector edge positions where charge collection is either incomplete or subject to field non-uniformities.

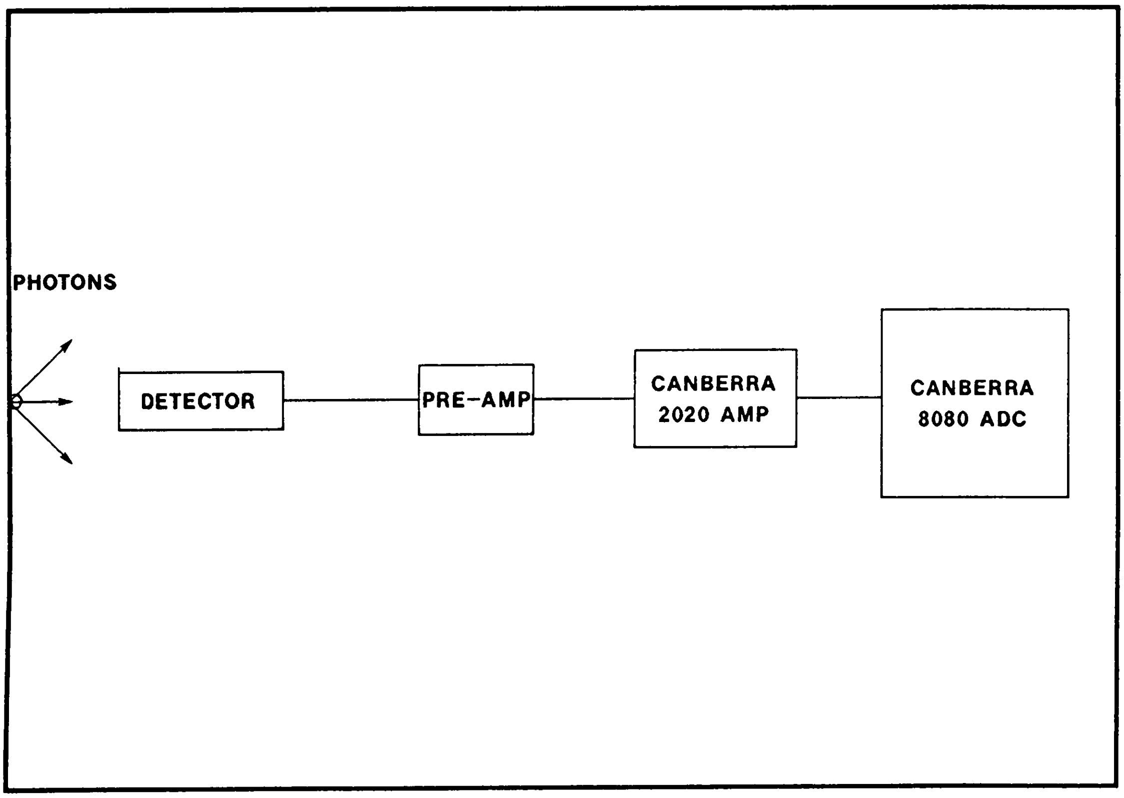

Fig. 2.4

Electronic circuit used for efficiency calibration of gamma ray detector

The omission of pulse shape rejection was based on the fact that it was not to be used under operational conditions. Pile-up rejection was used in the efficiency determination, again to be in line with the operational configuration, although count rates were extremely low (1500 Hz) during measurements. A precision pulse generator was used to determine dead time, which was less than 0,1% during measurements.

Both relative and absolute efficiency were determined for the side looking and front face viewing of the detector respectively.

2.4.1 Relative efficiency

Energy spectra were accumulated using the ^{152}Eu source at the standard distance for both geometries. At least 20 000 net counts were accumulated in each full energy peak used for calibration. The net counts in each peak were calculated after subtraction of the background contribution under the peak, which was obtained by linear interpolation of the background counts on either sides of the peak. The statistical error was determined via the equation

$$\sigma = (2N_i - N_a)^{\frac{1}{2}} \qquad (2.1)$$

where N_i = total counts in peak

N_a = N_i minus background counts in peak

The results obtained are illustrated in Fig. 2.5 on a semi-log scale. Statistical errors are smaller than the experimental points. The differences in efficiency for the two geometries are clear and can be attributed to the difference in thickness of the end cap for the two cases. The attenuation of 121 keV gamma rays in

1,0 mm and 0,5 mm (which are the respective thicknesses of these geometries) is 0,035 and 0,017 respectively while the same numbers for 1 408 keV gamma rays are 0,013 and 0,009 which explains the increase in difference of efficiencies with decreasing energy. The well known turning point in the efficiency curve at low energy, and the continuing decline of efficiency at still lower energies where absorption of photons in the end cap and other entrance windows of the detector starts to dominate, was not reached at 121 keV for these detector configurations.

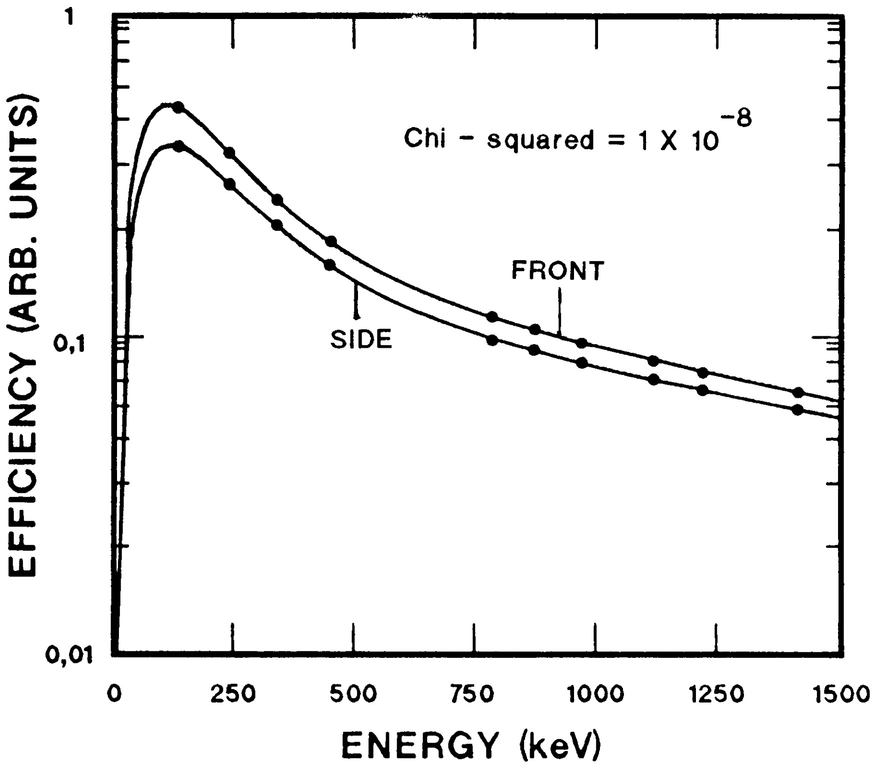

Fig. 2.5

Relative efficiency of IG detector as measured with ^{152}Eu for the two geometries plus non linear least squares fits to the data

A lot of work had been done (e.g. [Gr85],[Sa87], [Jä87] in the past on fitting empirical or semi-empirical functions to efficiencies of gamma ray detectors. An analytical function which yielded extremely good results for the data points obtained in this measurement was the function suggested by Sánchez-Reyes et al[Sa87], namely

$$\varepsilon(E) = \exp(a_1 - (a_2 + a_3\exp(-a_4E))\exp(-a_5E)\ln(E)) \qquad (2.2)$$

The non linear least squares fits to the two sets of data are included in Fig. 2.5 and the analyses of these fits are presented in Table 2.3.

Table 2.3

Statistical data of fits to data points

Parameters	Estimates (front)	Estimates (side)
a_1	6,32 ± 0,48	6,32 ± 0,53
a_2	0,757 ± 0,057	0,716 ± 0,088
a_3	0,775 ± 0,038	0,716 ± 0,043
a_4	$4{,}05\times10^{-3} \pm 1\times10^{-4}$	$3{,}81\times10^{-3} \pm 5\times10^{-4}$
a_5	$2{,}94\times10^{-4} \pm 1{,}8\times10^{-5}$	$2{,}82\times10^{-4} \pm 1{,}9\times10^{-5}$

Fitted efficiency deviation from data points

Energy (keV)	Experimental		Fit		% Deviation	
	Front	Side	Front	Side	Front	Side
121	0,536	0,404	0,5370	0,404	0,2	0,03
244	0,377	0,303	0,378	0,303	0,3	0,008
344	0,269	0,222	0,269	0,223	0,2	0,3
444	0,204	0,174	0,205	0,172	0,4	0,9
778	0,118	0,100	0,118	0,101	0,01	0,9
867	0,107	0,0913	0,107	0,092	0,5	0,7
964	0,0985	0,0843	0,098	0,084	0,5	0,3
1112	0,0854	0,0749	0,086	0,074	1,2	0,5
1212	0,0788	0,0689	0,080	0,069	1,1	0,3
1408	0,0691	0,0602	0,068	0,060	0,8	0,3

Although no experimental measurements were obtained in the lower energy region where the efficiency decreases, the extrapolated fit stayed physically reasonable. This is in contrast with the function suggested by Jäckel et al[Jä87] where this lower energy part of efficiency is described by the arctan function. With no points in this region where the arctan function dominates, it was not possible to obtain a reasonable fit to the data points.

2.4.2 Absolute efficiency calibration

The absolute efficiency measurement was made using a ^{60}Co source and comparing the peak at 1,332 MeV of the germanium detector with that of a 3" x 3" NaI(Tl) detector. Spectra were accumulated for both scintillator and germanium detector and the calibration was performed. The efficiency was measured to be 18,8% compared with the specification as supplied with the detector of 18%.

2.5 Spatial response characteristics

The aim of spatial response measurements was to establish the exact position of the ingot for accurate ultimate placing of the detector, as well as the study of edge effects. To determine spatial response characteristics a collimated source was used, placing a ^{152}Eu source behind a lead collimator. The source was attached to the lead and scanned vertically and horizontally across the detector. Although the full analysis was done for 10 different photon energies, only results for 121 keV, 344 keV and 1 408 keV are presented. No additional information is gained in presenting the results from the full energy spectrum as smooth interpolation is observed for other intermediate photon energies. Several collimators were tested, varying from 2,5 cm to 9,5 cm thick lead, with collimator apertures 3 mm to 5 mm diameter. The selection of thickness and diameter of aperture is defined by the interplay between effective shielding (particularly for the high energy gamma rays), inverse square distance yield from the source (which affects signal to noise ratio) and angular definition of the source.

The basic collimator configuration is shown in Fig. 2.6.

Positional scans of the efficiency response of the detector were performed by translating the source and lead collimator on a precision X-Y translation table. The intensity was measured at each position, and the yield plotted as a function of scanning position.

The size of the detector was nominally 4,6 cm diameter by 5,0 cm long. The position of the active detector volume was established relative to the can as the front face of the detector was scanned from top to bottom and side to side, both scans crossing the centre. The side of the detector was similarly scanned horizontally on both sides from the end of the detector end cap, and vertically at three positions relative to the face of the detector.

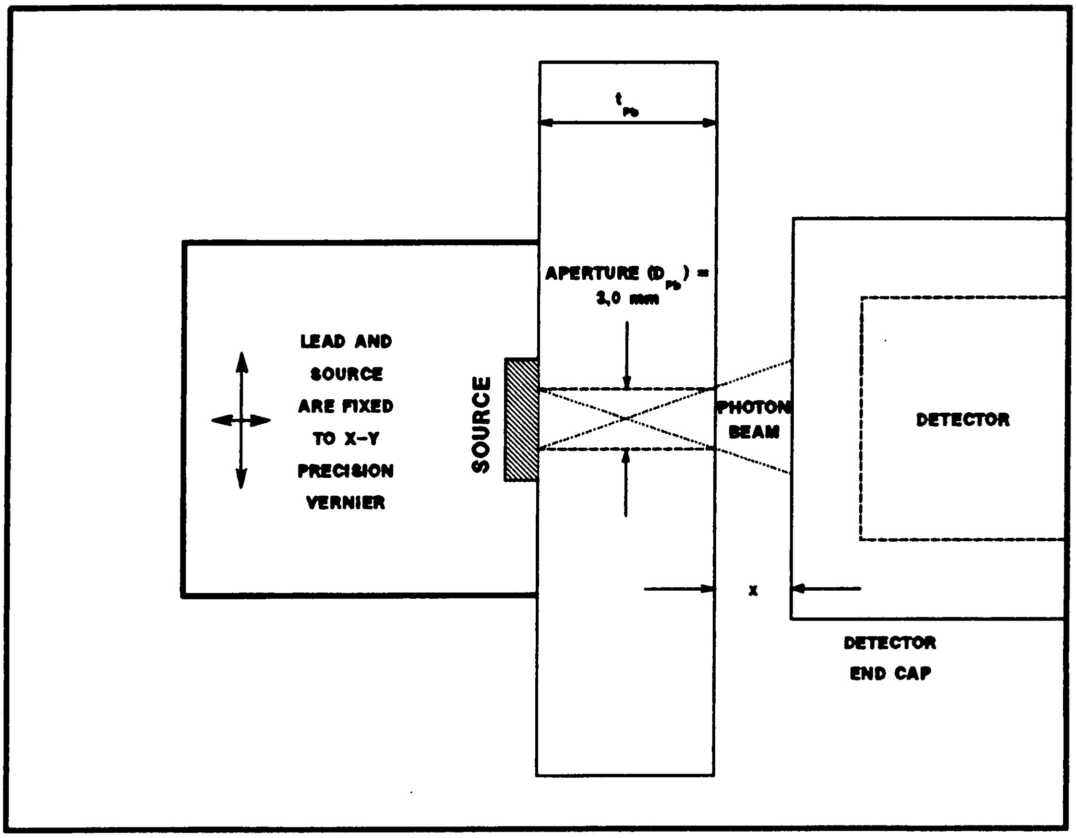

Fig. 2.6

Collimation geometry used for spatial response measurements

2.5.1 Choice of absorber and aperture

When transmission through the lead absorber is neglected the maximum diameter D_{max} of the collimated beam of photons with the source placed against the back side of the lead is geometrically determined at the front face of the detector by

$$D_{max} = 2D_{Pb}\left(1 + \frac{x}{t_{Pb}}\right) - D_{Pb} \qquad (2.3)$$

where D_{Pb} = diameter of aperture in the lead
t_{Pb} = thickness of lead
and x = distance from the lead to the detector cap

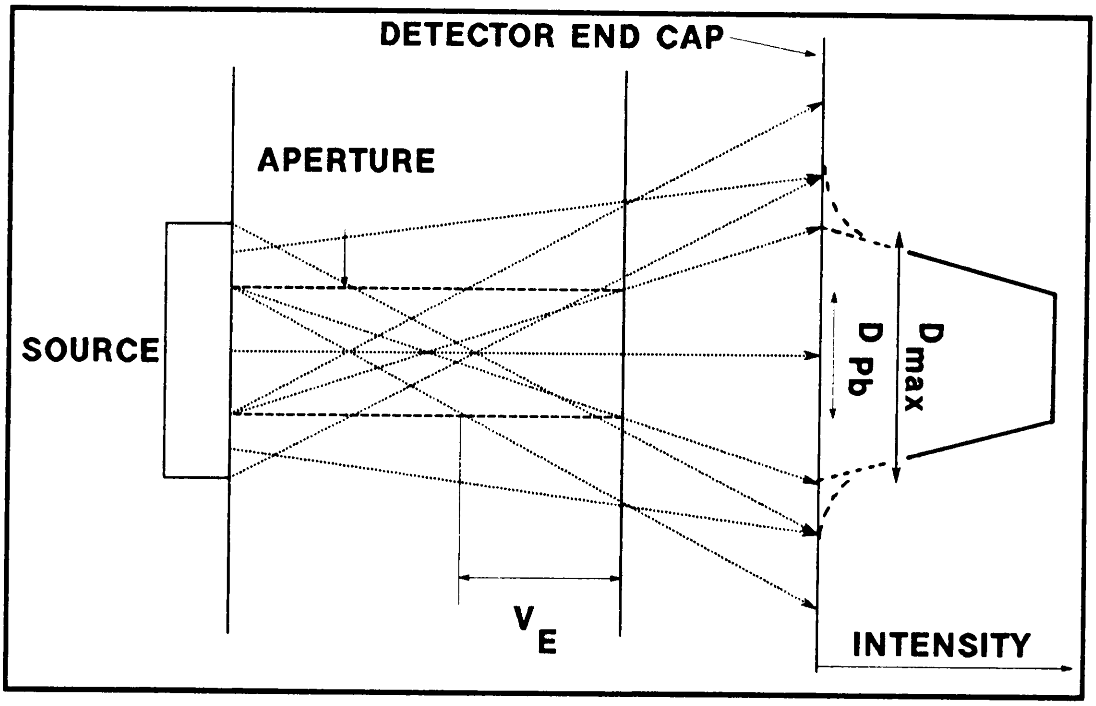

Fig. 2.7

Photon intensity criteria inside the beam spot as a function of position

This does not imply uniform illumination over this diameter. The intensity as a function of position inside the beam spot is very dependent on photon energies and geometrical parameters to account for absorber penetration.

It is fairly easy to obtain the functional form of this intensity function from pure geometrical considerations, assuming a uniform source.

The various contributions from the source to intensity as a function of position on the detector cap face are shown in Fig. 2.7. These contributions were calculated considering 11 different intensity components and added to one functional form which was analysed on a personal computer with the Mathcad routine. Three representative energies, 121 keV, 344 keV and 1 408 keV, of photons were considered.

The resulting intensity functions are shown schematically in Fig. 2.8 for these energies, with parameters as listed in the figure. The obvious feature of the function for 121 keV gamma rays is the fact that there is virtually no penetration through the lead, except for a very small component at diameter D_{max}. The intensity in the plateau region is constant up to D_{Pb}, and then decreases linearly to zero at D_{max}. For photons with energy of 344 keV there is significant penetration at the edges of the aperture, although the functional form is essentially conserved. The decrease in intensity is no longer linear but more exponential.

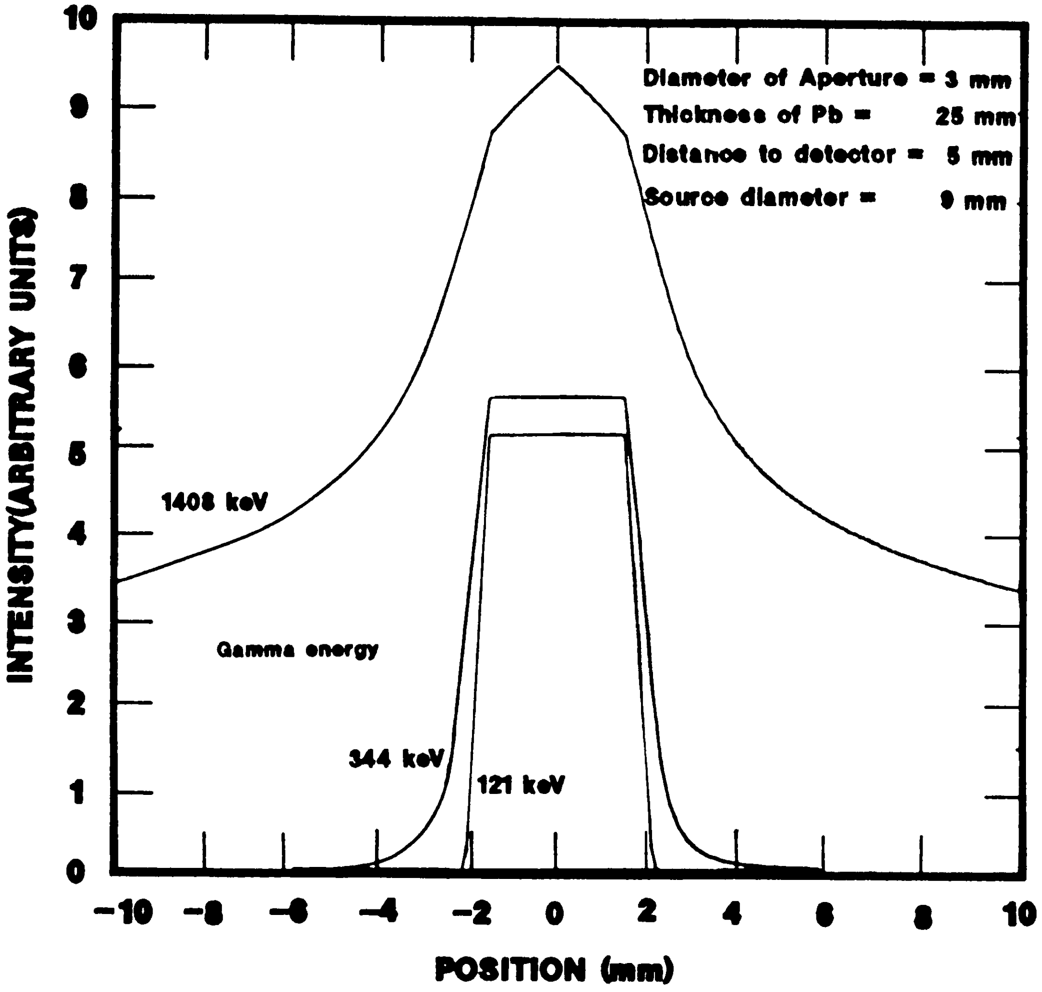

Fig. 2.8

Calculated intensity functions through lead as a function of position a) E = 1 408 keV, b) E = 344 keV and c) E = 121 keV

At 1 408 keV there is little comparison with the beam spots of the lower energies. The centre plateau of the beam spot is no longer constant, and there is a big background contribution from photons penetrating the lead. The higher yield at the centre of the beam spot is due to the fact that the source was taken to be larger than the aperture, with these parts of the source behind the lead adding to the intensity at the centre of the beam spot.

Other basic parameters of relevance are shown in Table 2.4 indicating penetrability and effective collimation as a function of source aperture diameter and lead thickness. The use of Hevimet (tungsten/nickel/iron alloy with density 18.0 g/cc) would have been preferable, but was limited by the ability to drill straight small apertures through thick material without curvature.

Table 2.4

Collimation penetrability and yield parameters for different lead absorber geometries

	x = 5 mm		E = 1 MeV				
Pb Thickness (t_{Pb})(cm)	Transmission through Pb	Collimation* of photon beam (aperture in mm)			Relative yield**		
		3,0	4,0	5,0	(3,0)	(4,0)	(5,0)
2,5	0,11	4,2	5,6	7,0	100	133,3	166,7
3,5	0,04	3,9	5,1	6,4	47,4	62,0	77,7
4,5	0,02	3,7	4,9	6,1	27,2	36,0	44,8
5,5	$8x10^{-3}$	3,5	4,7	5,9	17,2	23,1	29,0
6,5	$5x10^{-3}$	3,5	4,6	5,8	12,3	16,2	20,4
7,5	$1x10^{-3}$	3,4	4,5	5,7	9,0	11,9	15,1
8,5	$5x10^{-4}$	3,4	4,5	5,6	7,0	9,3	11,5
9,5	$2x10^{-4}$	3,3	4,4	5,5	5,4	7,3	9,1

* Maximum diameter calculated from (2.3)

** Normalized to 3,0 mm aperture and 2,5 cm lead thickness.

The results of this analysis led to the choice of 2,5 cm thick lead with a 3 mm diameter aperture. This choice was based on the compromise between good collimation and high relative yield and low penetrability obtained with this configuration. In the following discussion the effective beam spot size was defined as the full width of the effective beam spot at half the maximum intensity. The disadvantage due to significant penetrability of high energy gamma rays through 2,5 cm lead was corrected for, to first order, by using a blank absorber of exactly the same thickness and geometry, but

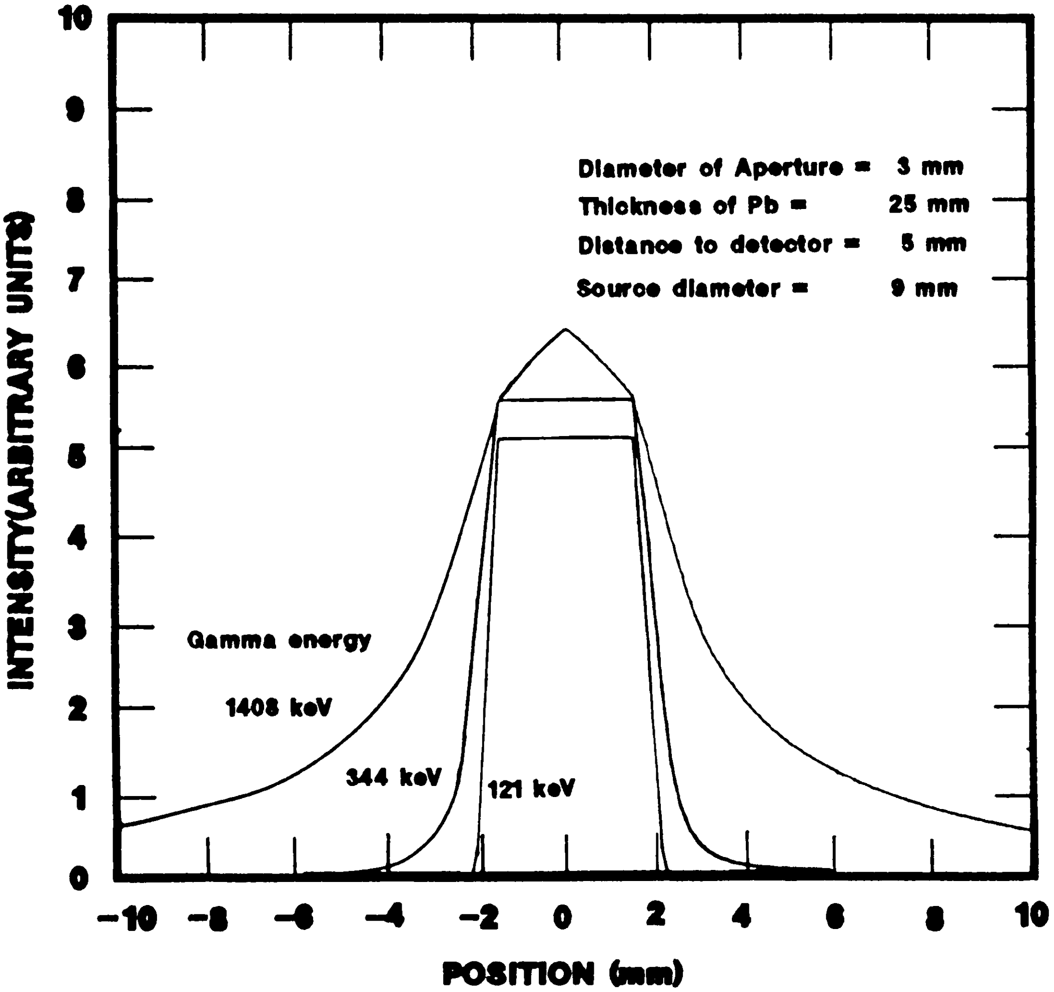

Fig. 2.9

Nett intensity functions for (a) 121 keV (b) 344 keV and (c) 1 408 keV without the aperture. With every measurement a penetration background had to be run and subtracted from the real measurement and all subsequent references to intensity functions were treated this way. This correction doubled the data accumulation times but count rates were sufficiently high (~300 Hz) to handle this for a maximum effective photon beam size of approximately 4,2 mm for 121 keV and 6 mm for 1 408 keV photons which was to be maintained at the front end cap of the detector. These calculated nett intensity functions for the three energies are shown in Figure 2.9 for the selected absorber.

When the yield is increased by using a bigger aperture (4 mm instead of 3 mm) the effect on collimation is significant. This is shown in

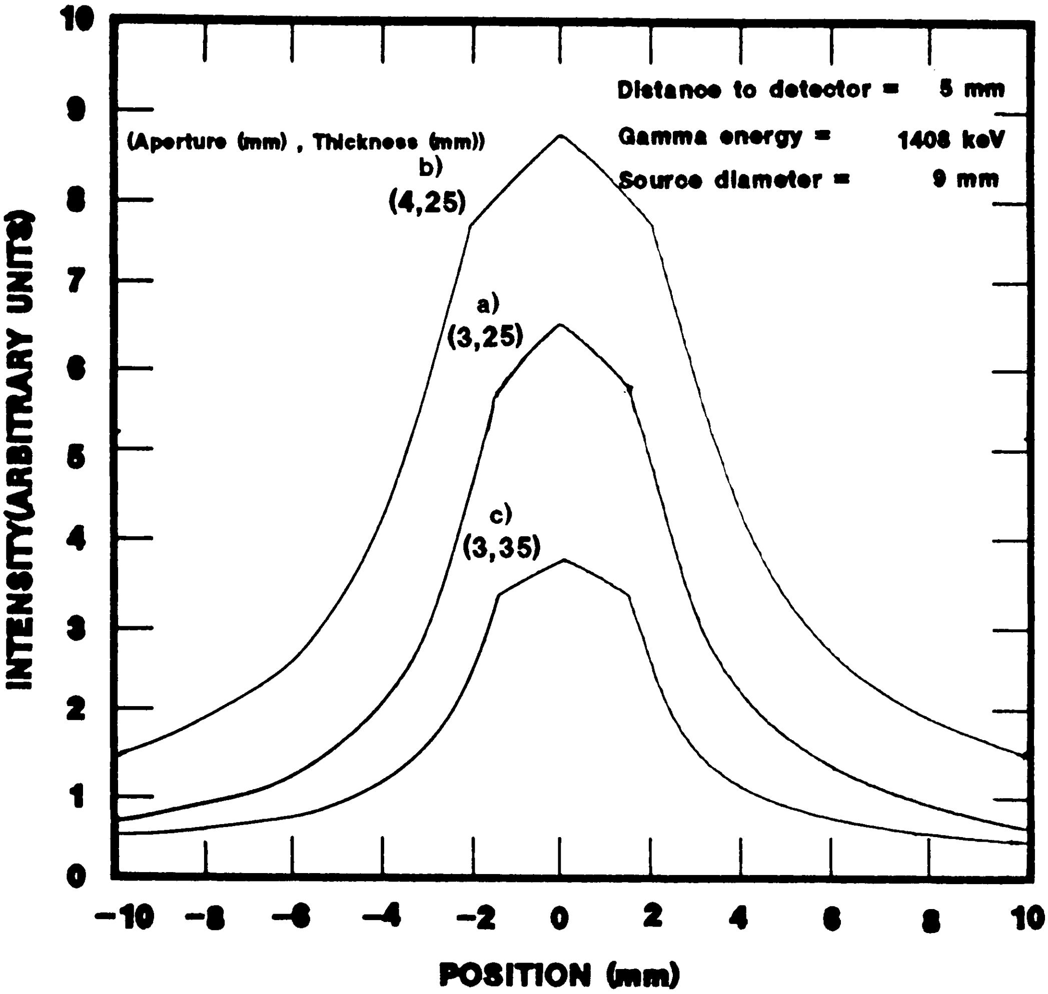

Fig. 2.10

Intensity functions for two different apertures: a) 3 mm and b) 4 mm and c) for thicker absorber (t_{Pb} = 3,5 cm)

Fig. 2.10 (b) which shows that the effective beam spot size for 1 408 keV increases by 35 % relative to Fig. 2.10 (a).

When attempting to improve collimation by using a thicker absorber, the maximum yield decreases by a factor of 2 on measuring from t_{Pb} = 2,5 cm to t_{Pb} = 3,5 cm, while little gain is made on collimation, the beam spot size decreasing by ~10%. This is shown schematically in Fig. 2.10(c).

The intensity distribution is more complicated when looking at the co-axial detector in the side looking geometry as a function of vertical position when the maximum diameter is defined by

$$D_{max} = 2D_{Pb}(1 + (\frac{x + k - (r^2 - y^2)^{\frac{1}{2}}}{t_{PB}}) - D_{Pb} \qquad (2.4)$$

where k = distance from lead to the geometrical centre of the detector
r = radius of the detector crystal
and y = vertical distance from the middle of the detector

This means that for the detector with a crystal diameter of 4,6 cm the maximum beam spot size on the end cap varied from 4,2 mm to 15,2 mm (E_γ = 121 keV) in a vertical side scan, taking the curvature of the detector crystal into account. This led to larger step lengths being made vertically along the side of the detector (6 mm) than step lengths horizontally along the middle of the side and front of the detector (3 mm).

The optimum condition is obviously when source effective diameter is equal to the aperture diameter. The significance of this is obvious when comparing the calculated beam spot for 1 408 keV photons with the expected beam spot with the source exactly the same size and geometry as the aperture. This is shown in Fig. 2.11. The intensity stays constant up to t_{Pb} when moving radially outward and falls off exponentially, but with a much smaller background contribution further from the centre.

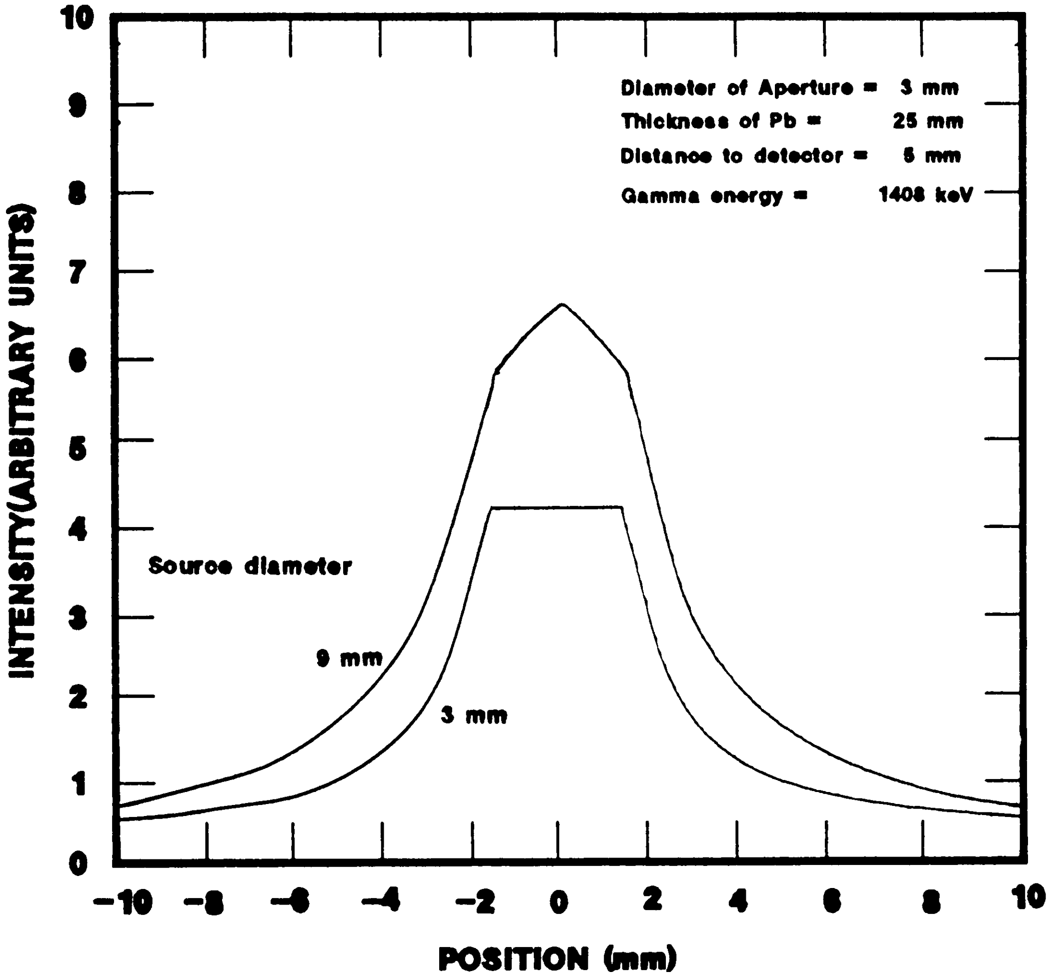

Fig. 2.11

Intensity distributions of the beam spot for photons with energy 1 408 keV and with source diameter (3 mm) equal to diameter of aperture compared with a source of 9 mm

The optimum source, whose active area equalled the hole diameter was not available but the best compromise was established. In order to optimise the source position, the source was scanned to establish if the source strength was uniform over the diameter (typically 1 cm), or had spots of higher activity, in which case these would be aligned with the detector hole. Although no statistically significant evidence of extreme "hot spots" were obtained with the scan, the spot with highest yield, which was sufficiently near the centre for the source to be centrally positioned, was used for measurements .

2.5.2 Results obtained

2.5.2.1 Front face

Results of the scans of the front face of the detector are shown in Figures 2.12 and 2.13. Both scans clearly show the lower efficiency in the central axial region of the co-axial detector where no clearing field exists for charged carriers.

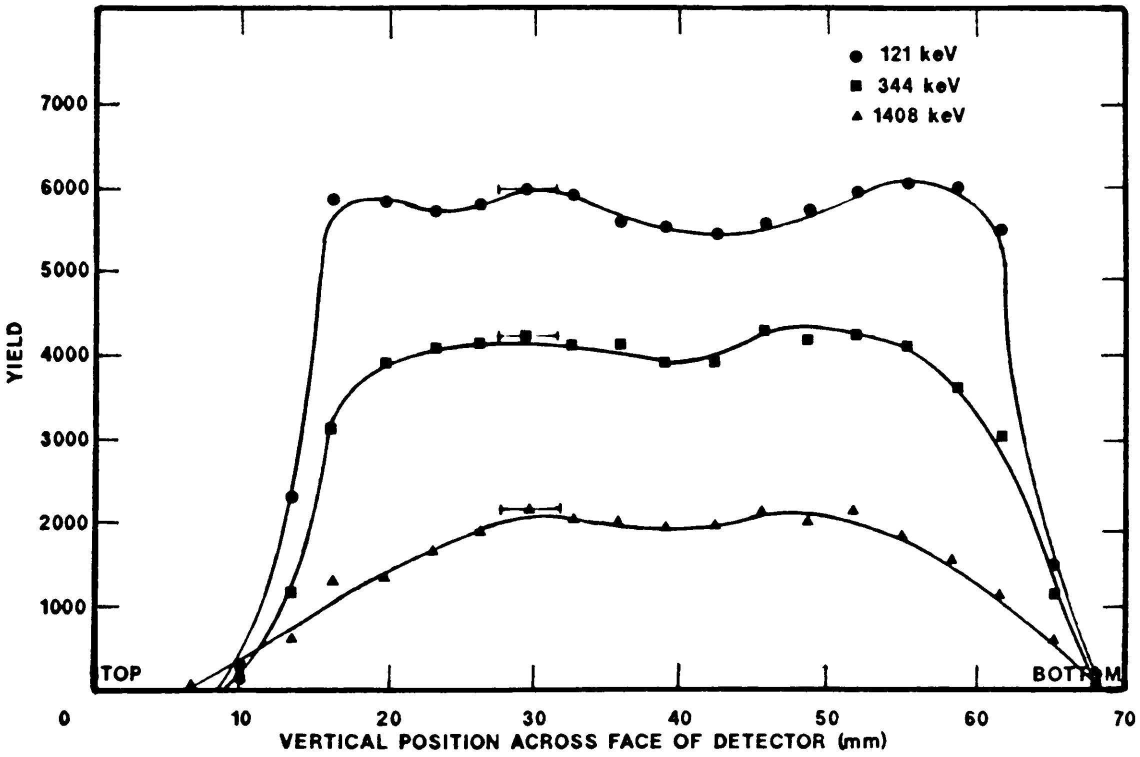

Fig. 2.12

Response of a vertical scan across the front face of the detector as a function of position and gamma energy

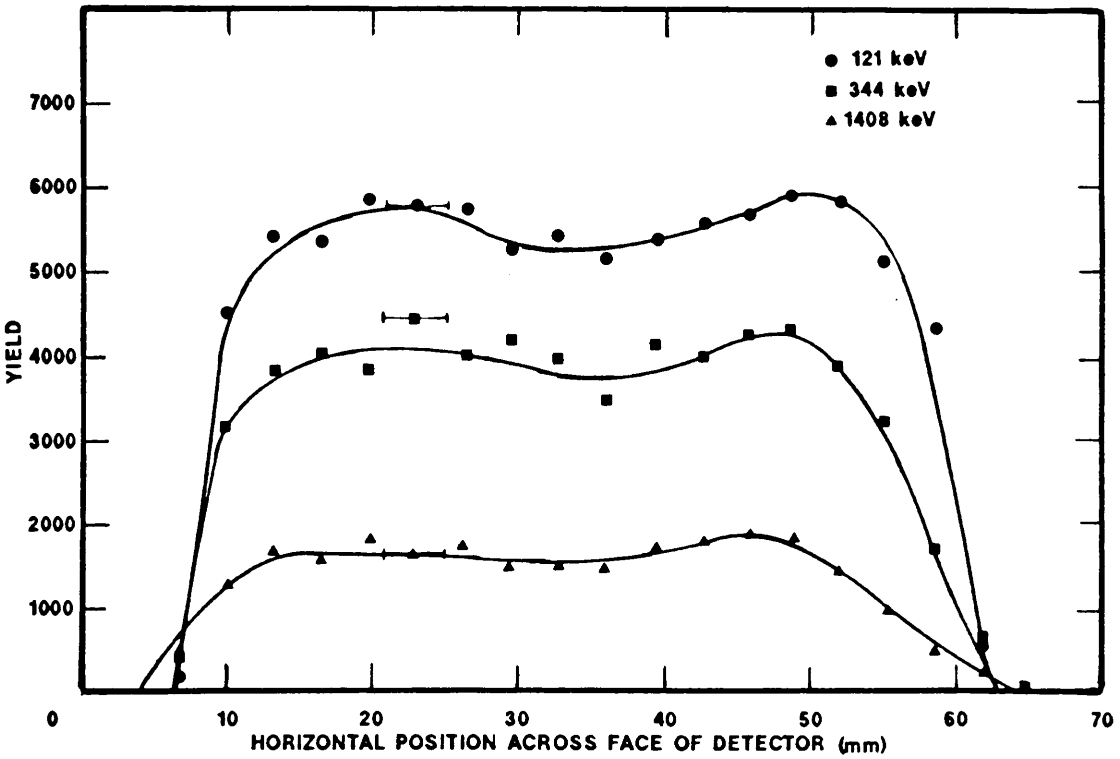

Fig. 2.13

Response of a horizontal scan across the front face of the detector as a function of position and gamma energy

The variation in sharpness of the drop in yield at the edges of the ingot is clearly seen as related to energy as expected. The results of the 121 keV photons were used to determine the physical position of the ingot accurately with respect to the detector housing material as the sensitivity of physical position with response increases with decreasing energy. Half of the average yield in the plateau region was taken to be representative of the edges of the detector crystal. The results of this analysis showed that the detector was not situated in the centre of the cap, as is shown schematically in Fig. 2.14, assuming a perfect circular shape. In addition, the vertical scan showed an active diameter of 4,9 cm while the horizontal scan showed 5,1 cm. It is known from earlier measurements that these detectors have frequently not pure cylindrical shapes.

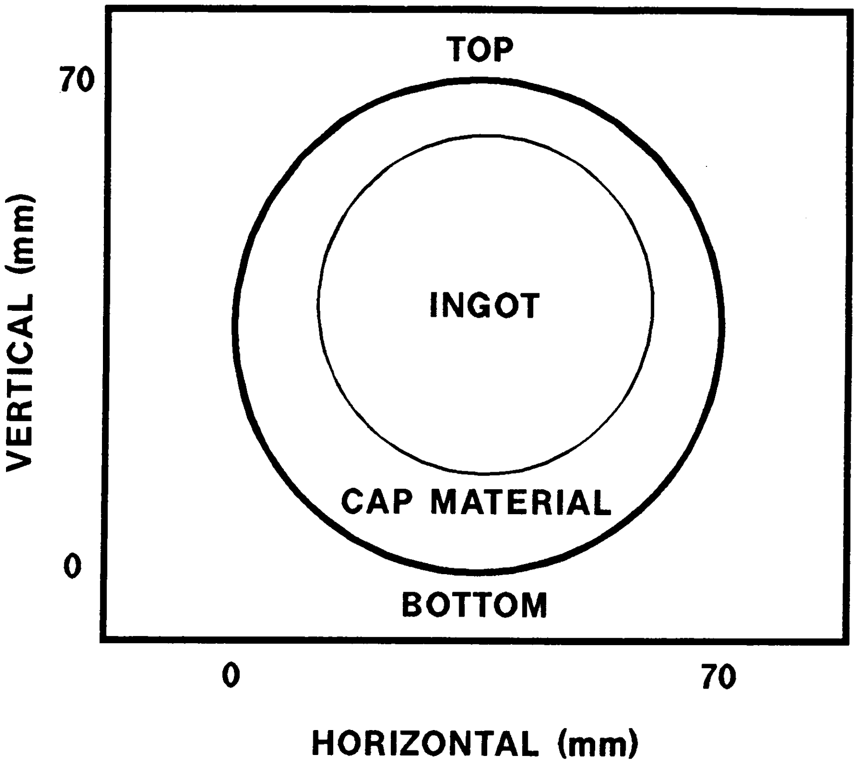

Fig. 2.14

Position determination of detector crystal with respect to the front face of cap material

2.5.2.2 Side

A horizontal scan in the centre of the can along the detector side which was to be used under operational conditions in the side looking configuration was made, and the results are shown in Fig. 2.15.

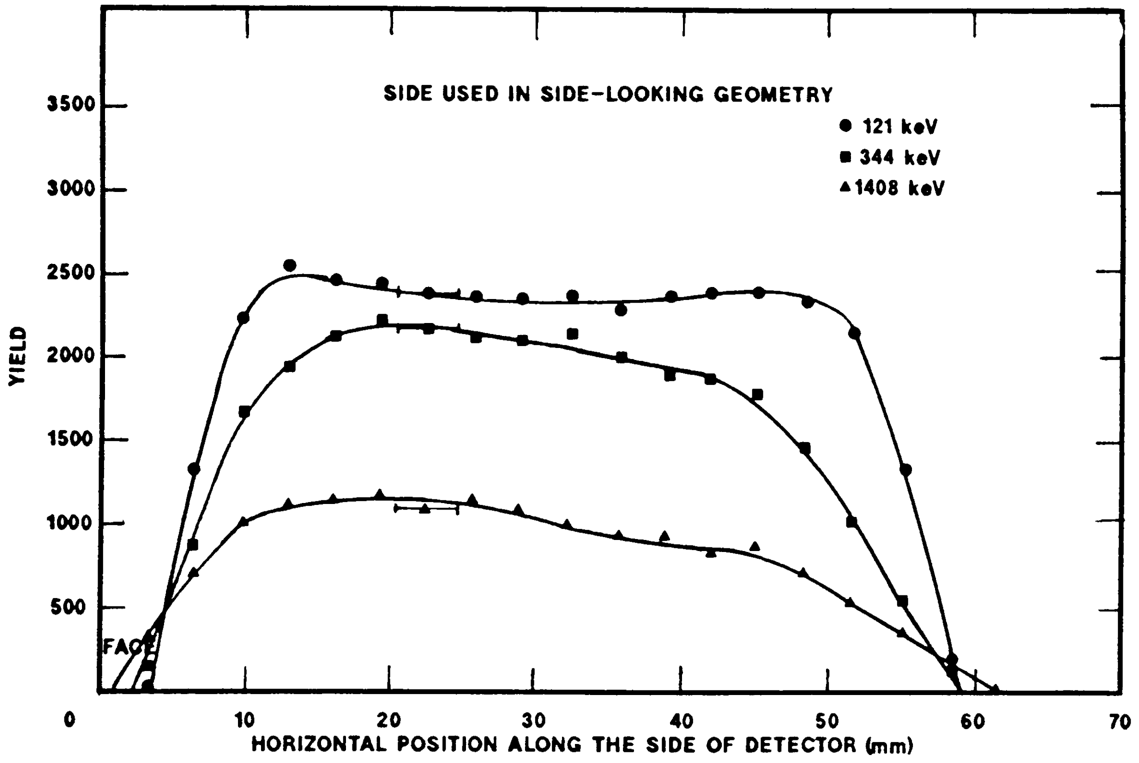

Fig. 2.15

Response along the side (used in the operational side looking configuration) of the detector as a function of position and gamma energy

A non-uniformity of response along the length of the detector (especially for the low energy gammas) is evident, and led to a similar measurement on the other side of the detector being made to verify these results. Fig. 2.16 indeed shows that this non-uniformity is observable on both sides of the detector. This shows that the side looking configuration should be used with care when making precision quantitative gamma ray spectral measurements.

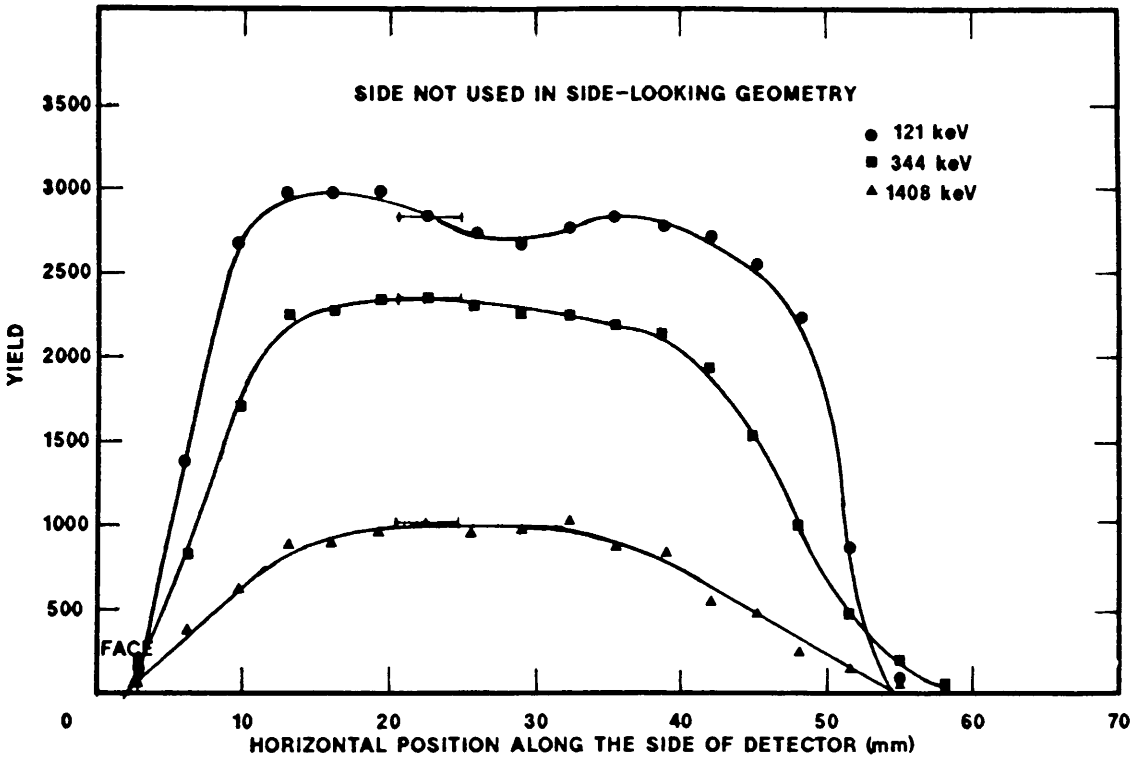

Fig. 2.16

Response along the side (not used in the operational side looking configuration) of the detector as a function of position and gamma energy

The difference in effective length of the detector is obvious as seen from the side for the two configurations. With the same technique used, it led to a length of 4,6 cm and 5,0 cm respectively.

The physical position of the ingot was obtained in the same way as for the front face and this position relative to the can material is shown in Fig. 2.17. The distance of 6,5 mm from detector can face to detector compares with the value of 5 mm quoted by the manufacturer. From this information it was calculated that an actual spot size of 5,8 mm was maintained on the front face of the detector crystal during scans.

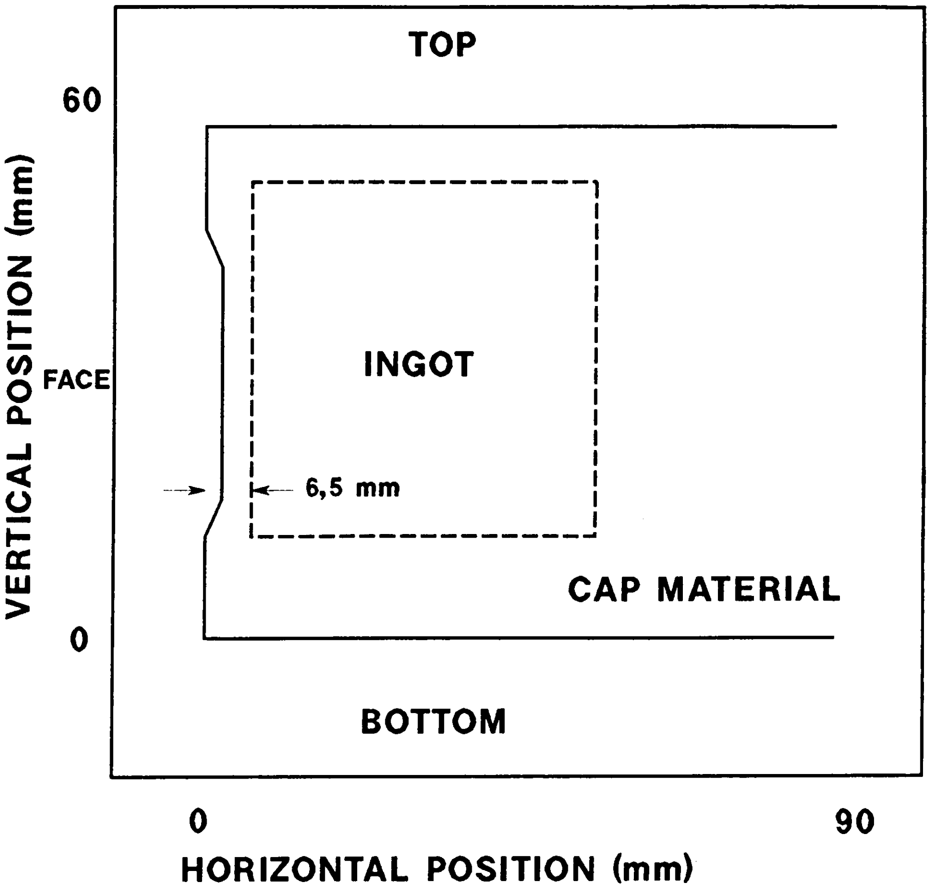

Fig. 2.17

Relative position of detector crystal along the side of the detector

Three vertical scans of the side from top to bottom were made at positions 17, 27 and 37 mm from the front face of the ingot, with the results shown in Figures 2.18, 2.19 and 2.20.

The absence of the sharp drop in yield at the edges of the detector is obviously due to the curvature of the crystal, leading to an increased effective beam spot size at the edges of the detector. This negative effect on position resolution is seen in the error bars in position accuracy at the edge of the detector.

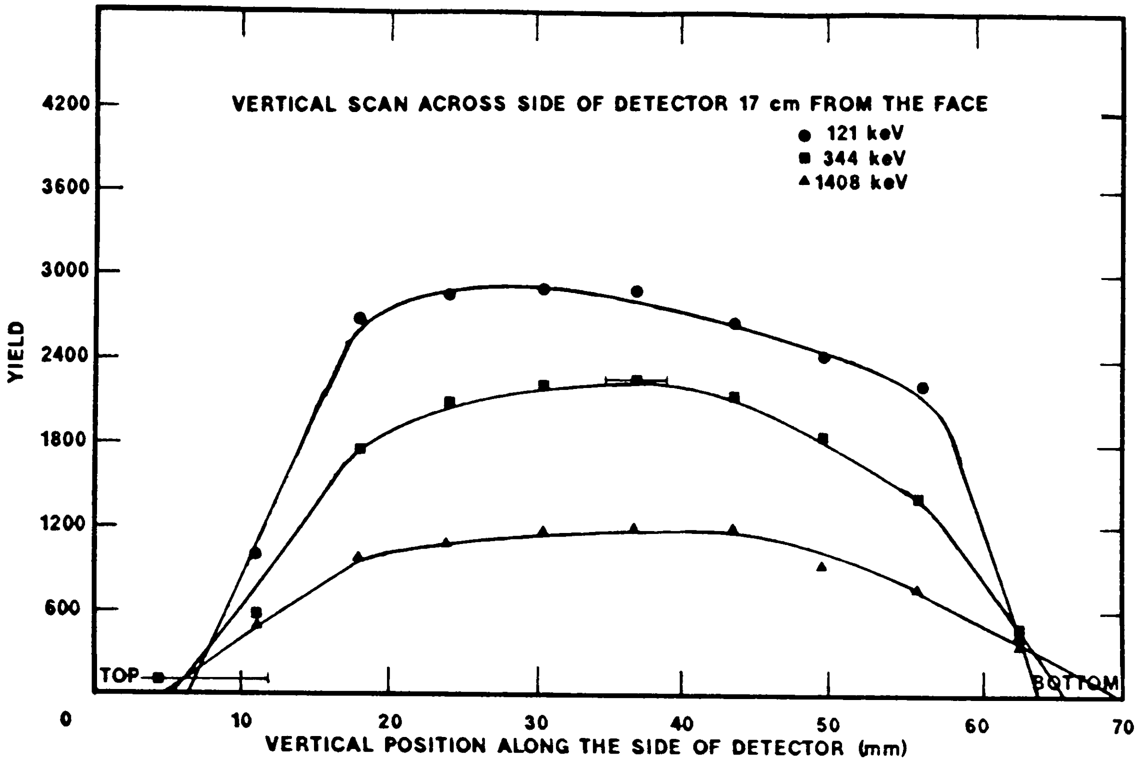

Fig. 2.18

Response of a vertical scan across the side of the detector 17 mm from the front face

A non-uniformity in response is clearly seen at a distance of 27 mm from the front face, corresponding to the centre of the detector crystal as shown in Fig. 2.19. This non-uniformity again probably indicates the complex geometry of the electric field in the crystal which, being sensitive only to the low energy photons, is representative of a surface anomaly. The results at 37 mm are similar to those at 17 mm and are shown in Fig.2.20.

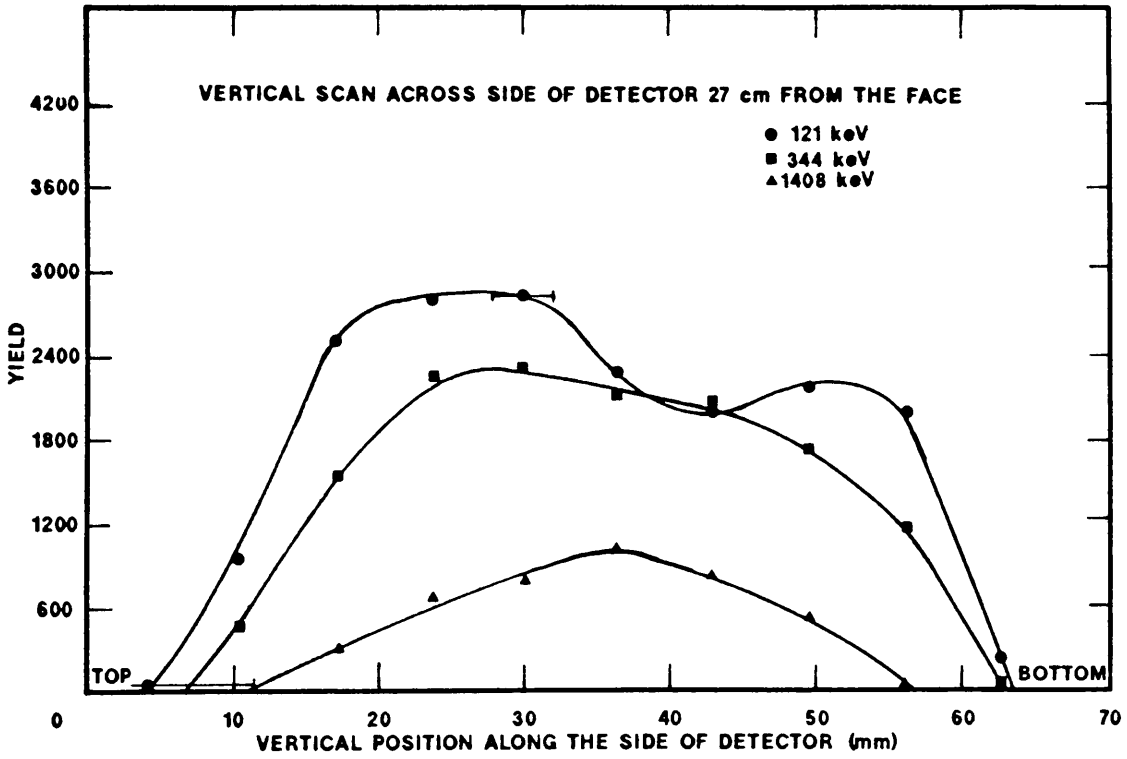

Fig. 2.19

Response of a vertical scan across the side of the detector 27 mm from the front face

Comment need to be made of the short response length of the 1408keV yield in Fig 2.19. This can in part be attributed to the large error bars in this measurement.

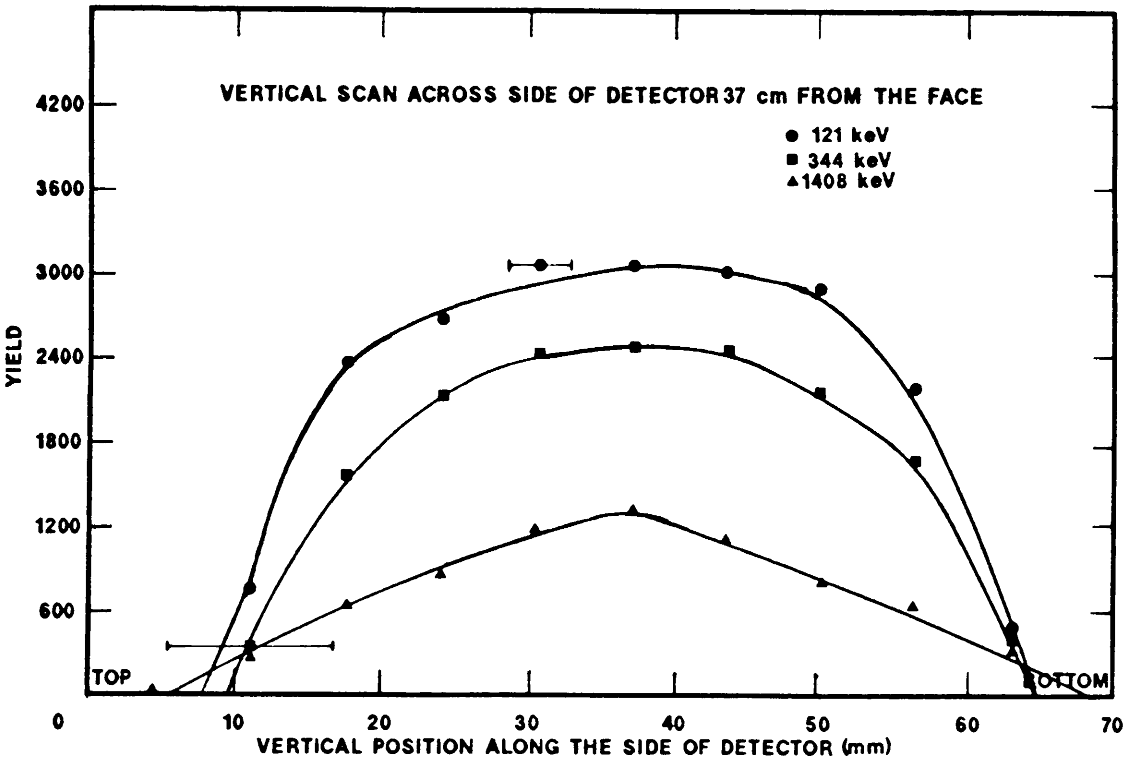

Fig. 2.20

Response of a vertical scan across the side of the detector 37 mm from the front face

2.6 Determination of background contributions

To determine the contribution of background radiation in a reactor environment, energy spectra in the side looking geometry were recorded and analysed. A typical spectrum is shown in Figure 2.21 where the usual main contributions[Ad69] to ambient background are indicated.

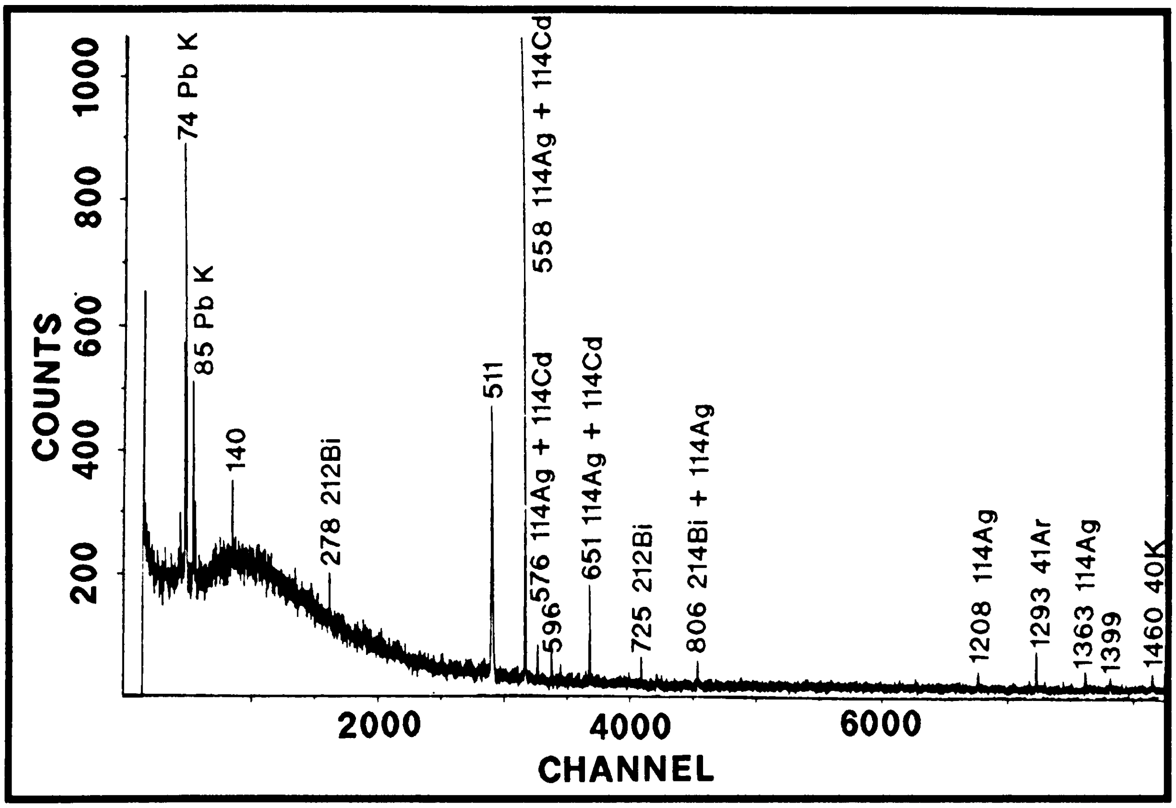

Fig. 2.21

Background spectrum accumulated in operating reactor environment

An extremely strong peak at 558 keV could not be attributed to a standard background nuclide. This peak was identified together with several others, as originating from the reaction of neutrons produced in the reactor with the cadmium spot welds inside the detector holder. The cross section for capture of thermal neutrons on cadmium is bigger than 2 000 barns, and the energies, intensities and life time[Wa72] of transitions in the residual nucleus in the reaction ^{114}Cd(n,p)^{114}Ag are shown in Table 2.5. The strong transitions are identifiable with the peaks designated in Fig. 2.21. The 747 keV peak is not distinguishable due to its low intensity, while the peak at 808 keV has another source of interference (^{214}Bi). The intensities of these transitions do not match well to the measured spectrum as there are contributions to some of these lines from the ^{114}Cd(n,n'γ) reaction. Peaks are expected from this reaction at energies 558 keV, 576 keV and 651 keV with relative intensities of 100; 7,3; 25,3 for E_n = 2,5 MeV[Gi74].

Table 2.5

Transition characteristics of ^{114}Ag ($t_{½}$ = 4.5 s)

Energy (keV)	Intensity (Rel)
558,1 ± 0,4	100
576,1 ± 0,5	8,1 ± 1,3
651,3 ± 0,6	3,3 ± 0,5
747 ± 3	0,7 ± 0,3
808,2 ± 0,7	3,0 ± 0,5
1208 ± 3	1,5 ± 0,5
1286,4 ± 2,7	0,7 ± 0,4
1302,9 ± 0,6	5,5 ± 1,0
1363,8 ± 1,2	1,8 ± 0,4

To verify these results, similar data was accumulated after a reactor week-end shutdown period of 66 hours, results of which are shown in Fig. 2.22.

Due to the short half life of ^{114}Ag (4,5 s) the contribution of this nuclide would be expected to vanish from the spectrum, but with stored fuel elements and other sources of neutrons present inside the reactor, the 558 keV peak is still distinguishable, although with much less intensity.

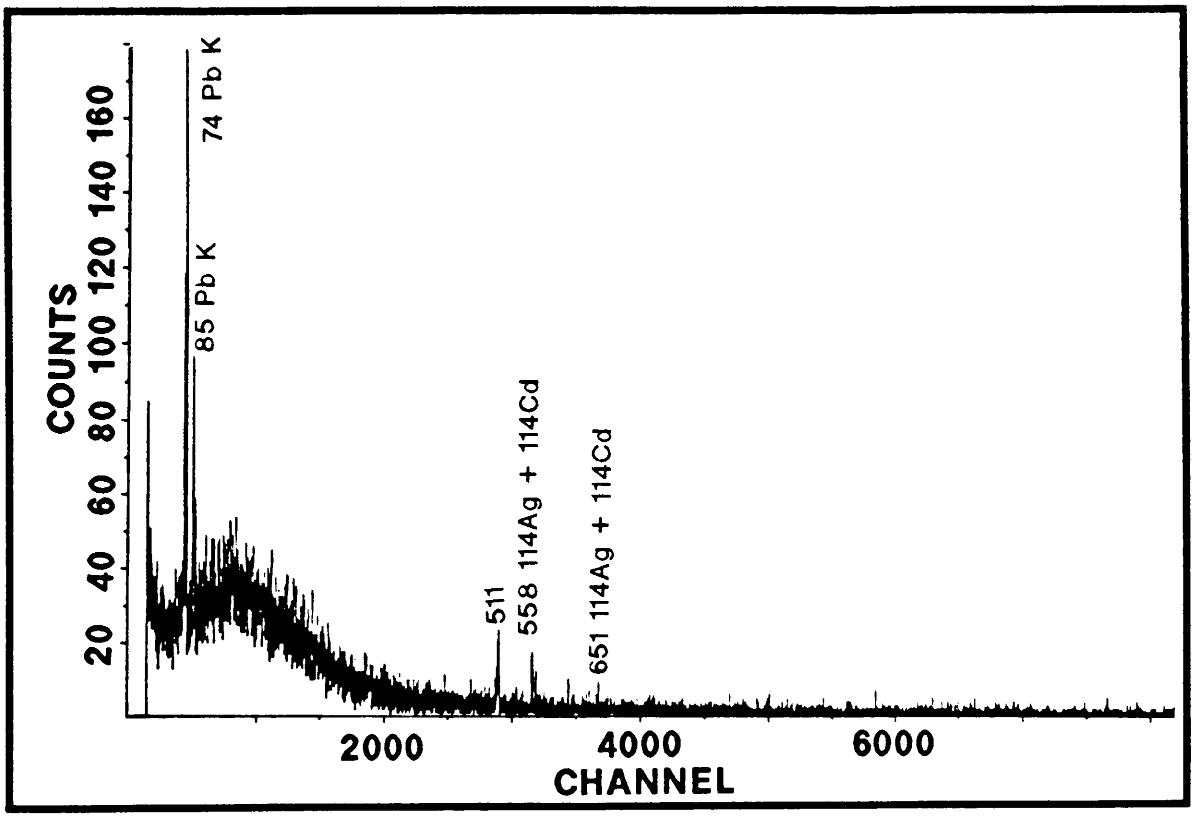

Fig. 2.22

Background spectrum accumulated in reactor environment after a shutdown period of 66 hours

Due to the high cross section for this reaction (>2 000 barns) cadmium is never used (except for control rods) in reactor materials, and in the analysis of fuel element assemblies this contribution of cadmium from the detector assembly could well have been mistaken for cadmium impurities in fuel elements.

2.7 Conclusion

The relative and absolute efficiencies of a gamma ray detector were determined using a ^{152}Eu source. The study included a compilation of previous measurements on energies and intensities of transitions attributed to this source.

Collimated beams of photons have been used to determine the physical position of the detector crystal inside the end cap as well as position dependent efficiency of the detector. It was shown that the detector crystal used was not situated in the centre of the detector assembly. The position of the active volume of the detector was determined and the response along the length (side looking) and face was shown to be non-uniform. This endorses the need that manufacturer specifications should not be merely accepted but experimentally determined.

In the reactor environment, the ambient gamma-ray background was analysed and it was established that neutron inelastic scattering and excitation of ^{114}Ag from ^{114}Cd present in the detector mounting materials contributed several background peaks which would need to be taken into account at a later stage when fuel pins are analysed.

3 THE LIFETIME OF THE 0_2^+ STATE OF ^{72}Ge

3.1 Introduction

The inelastic scattering of neutrons from germanium is extremely well known to protagonists of (n,n'γ) reaction studies. The Ge(Li) or intrinsic germanium (IG) detector used conventionally as a gamma ray detector displays well developed asymmetric peaks at energies corresponding to excitation by neutrons of specific levels in the germanium of the detector itself. These asymmetric peaks result from the summation of the two energy signals corresponding to the recoil Ge compound nucleus which has an energy defined by the reaction kinematics, summed with the signal derived from the de-excitation of the excited state produced.

Natural germanium consists of five isotopes and of these ^{72}Ge and ^{74}Ge are of prime importance during neutron bombardment of natural germanium. The isotopes, together with their relative abundances, Q values and cross sections of reactions leading to the first excited state of each isotope are tabulated in Table 3.1.

Table 3.1

The natural isotopic constitution of germanium together with reaction parameters at E_n = 1 MeV[Li69]

Isotope	Abundance %	σ(n,n'γ) (b)	Q values*(MeV)
^{70}Ge	20,5	0	-1,0396
^{72}Ge	27,4	1,1	-0,6913
^{73}Ge	7,8	-	-0,01326
^{74}Ge	36,5	1,6	-0,5958
^{76}Ge	7,8	1,5	-0,5628

* These values are appropriate to the first excited state of each nucleus.

Three well known levels so excited are the 596 keV 2+ level in ^{74}Ge, the 691 keV 0_2^+ level in ^{72}Ge and the 834 keV 2+ level in ^{72}Ge. The first and third levels mentioned decay by gamma emission with the characteristic associated distribution of the energy signal as defined by the detector response to gamma rays of energies 596 keV and 834 keV respectively. The attenuation of 596 keV and 834 keV photons in 1 cm germanium is 0,33 and 0,28 respectively. The 0_2^+ (second 0^+ level) level of ^{72}Ge (ground state $J^\pi = 0^+$) is totally internally converted and therefore provides a well defined full energy peak corresponding to detection of 691 keV conversion electrons with essentially 100 % efficiency. This level therefore lends itself ideally to special study via inelastic scattering and was the subject of this project.

The lifetime of a level can be measured when it is sufficiently long lived by electronically measuring the time difference between two energy signals. This is the case with the level under study where the lifetime of the 0_2^+ state of ^{72}Ge has been determined nine times before[Bo48, Mc49, Ke55, Kr56, Ei68, Ma68, An71, Dr74, Br84] by widely varying methods and with very different results. The values obtained in the different attempts are listed in Table 3.2 and illustrated in Fig. 3.1. From these results it is obvious that a large spread in values occurs, with the most recent determination[Br84] being orders of magnitude more accurate than previous measurements. It was therefore necessary to perform a measurement to attempt to confirm this latest value.

Table 3.2

Previous measurements of the half life of the 0_2^+ level in ^{72}Ge

Reference	Year	$T_{1/2}$ (ns)	% Err.
Bo48	1948	500 ± 50	10,0
Mc49	1949	290 ± 60	20,7
Ke55	1955	416	No error quoted
Kr56	1956	300	No error quoted
Ei68	1968	422 ± 13	3,1
Ma68	1968	440 ± 20	4,5
An71	1971	410 ± 60	14,6
Dr74	1974	404 ± 45	11,1
Br84	1984	444,2± 0,8	0,18

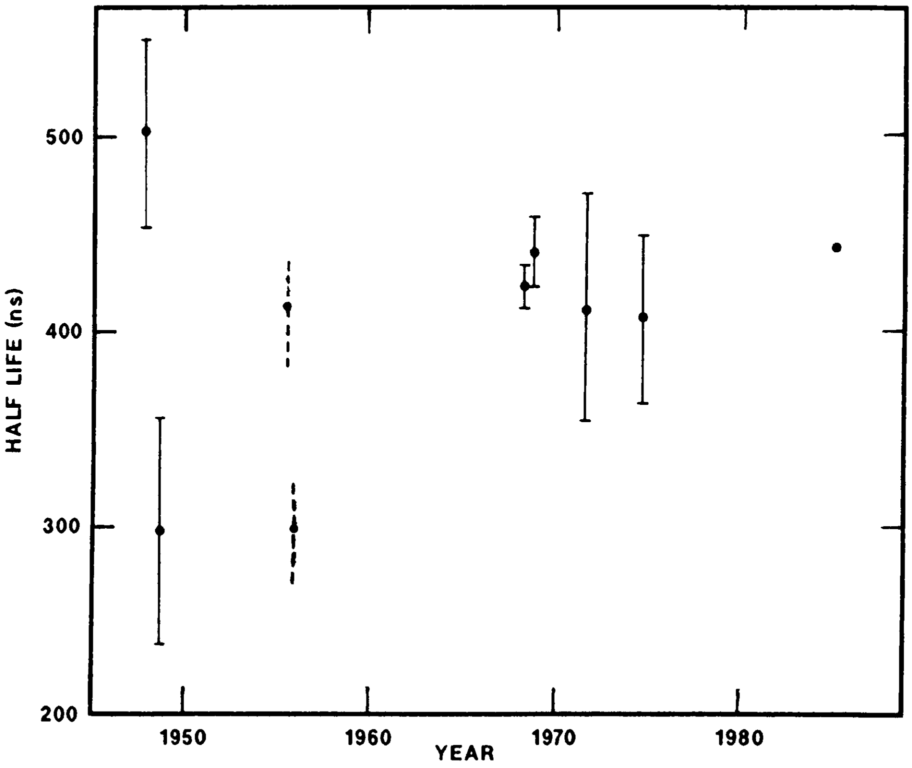

Fig. 3.1

Results of previous measurements of the half life of the 0_2^+ level in ^{72}Ge

3.2 Isomerism and internal conversion

When a nucleus is excited to a level other than the ground state it rids itself of the excess energy through emission of radiation. This radiation can be one of several possibilities, namely gamma decay, internal conversion, or if the energy is sufficiently high, particle decay or internal pair production. For gamma decay the energy of transition is defined by the energies of the states and the transition probability is characterised by the multipolarity. This is defined by the spin and parity of the initial and final states of the nucleus. This led to the different designations for electric transitions (E1, E2, ...) and magnetic transitions (M1, M2, ...), where e.g. E2 electric radiation corresponds with a change of 2 in the angular momentum.

If the excitation level is below threshold for particle emission then gamma emission is normally the preferred method of decay, but when such transitions are prohibited by selection rules (such as $0^+ \longrightarrow 0^+$) or other constraints (e.g. high spin change), the lifetime of such a state may become long compared with normal de-excitation times. This led to the somewhat arbitrary term of isomeric state for these levels, which is derived from the fact that these states are in metastable equilibrium.

Since monopole electromagnetic radiation is not possible a 0^+ level in a nucleus cannot de-excite through gamma emission to a 0^+ ground state. These transitions take place through internal conversion, or if the de-excitation energy is large enough (> 1,022 MeV), through internal pair formation.

Internal conversion involves the direct interaction of the nucleus with an electron moving close to the nuclear region. This interaction consists of the nucleus transmitting its excess energy to such an electron in an inner shell, and ejecting the electron from the atom. The kinetic energy of the emitted electron is equal to the transition energy minus the binding energy of the electron. The vacancy produced in an inner shell leads to the usual atomic processes under these circumstances, namely X-ray emission or Auger electron emission.

This is exactly the mechanism by which ^{72}Ge decays from the 0_2^+ state to the ground state. By precisely measuring the kinetic energy of the emitted electron it is possible to determine the origin (K,L, etc) of the electron, and with careful electron spectroscopy it is possible[Dr74] to measure differences in energies of electrons emitted from different shells.

There have been attempts to describe the lifetimes of isomeric states with zero total angular momentum change by approximate analytical expressions. A classical approach by Marmier and Sheldon[Ma69] described the mean lifetime τ_a by

$$\tau_a^{0\rightarrow 0} = \frac{0.37}{Z^3 A^{4/3}} \left(\frac{m_e c^2}{E_0 - B_a} \right)^{1/2} \qquad (3.1)$$

where

Z - atomic number
A - mass number
m_e - rest mass of electron
E_o - energy of the level
B_a - binding energy of the electron in the "a"-shell

Applying the equation to the level under study for a transition involving an electron from the K-shell of ^{72}Ge with Z = 32, A = 72, E_o = 0,691 MeV and B_k = 11,1 keV one obtains a classically predicted lifetime of 33 ns. These predictions are usually accurate to within an order of magnitude and in this case are far removed from the experimental measurements of the lifetime of about 600 ns. This can be attributed partly to the assumption of $E_o << m_ec^2$ in the derivation of this formula which is not valid in this case.

3.3 Previous measurements

In 1948[Bo48] and 1949[Mc49] the measurement of lifetimes by the delayed coincidence method using anthracene scintillation counters was improved and thereby extended to measure time intervals of down to 10^{-7} seconds. Via this method the time differences between signals from the beta decay of ^{72}Ga to ^{72}Ge ($t\frac{1}{2}$ = 14 hours) and the internally converted 0_2^+ state could be measured, and the mean lifetime therefore obtained.

A report in 1955[Ke55] on a measurement by a delayed coincidence technique recorded the half life of this level to be 0,416 µs, with no error quoted by the authors. Another measurement in 1956[Kr56] found the half life to be consistent with 0,3 µs, also with no error being quoted.

The next measurement chronologically[Ei68] had a significantly smaller associated error (~13 ns) using neutron inelastic scattering to excite the 0_2^+ level in ^{72}Ge inside a Ge(Li) detector, thereby also using the detector as target and detector for the first time. Neutrons with energies of 4,75 MeV were produced via the D(d,n) reaction on a 5,5 MeV Van de Graaff accelerator. The essence of the analysis was dependent on the pulsed deuteron beam which produced a pulsed neutron source having a repetition rate of 500 kHz. The pulse duration had a negligible effect on timing resolution. The internal conversion signal from the detector was fed through a time pickoff device to start a time-to-amplitude converter (TAC). The stop signal was obtained from the delayed signal of the beam pickoff. The TAC pulse height output was gated by the signals from a single channel analyser fed from the energy output of the Ge(Li) detector set to accept only signals corresponding to the 691 keV transitions. The time spectrum was then analysed with a least squares routine to obtain the lifetime quoted of 422 ns. Similar measurements were made to determine the effect of background but were found to be of no importance.

Also in 1968, Main et al[Ma68] measured the lifetime of the 1,64 MeV level in ^{40}K by a similar method, and simultaneously determined the lifetime of the 0_2^+ state in ^{72}Ge by setting gating windows on the 691 keV peak, and another window on the background just above it. The time spectra obtained were analysed in a similar way to the previous measurement.

In 1971[An71] ^{72}Ge in a natural germanium target was excited to the 0_2^+ state by inelastic proton (E_p = 6,1 MeV) scattering and two Si(Li) counters were used to detect both conversion electrons from the de-excitation signals and the scattered protons. Their outputs were used to start and stop a TAC. Suitable energy windows were set around the output pulses to select signals originating from inelastic scattered protons and conversion electrons. It was therefore possible to obtain two independent decay curves for the same reaction simultaneously. A similar measurement was made by Draper et al[Dr74] by bombarding enriched ^{72}Ge targets with a 28 MeV pulsed alpha beam from an AVF cyclotron. The two time signals were obtained from the beam pulse, and an in-beam Si(Li) detector which acted as electron spectrometer. A window was set around the 691 keV peak observed in the energy spectrum of this detector.

The most recent measurement[Br84] used the delayed auto coincidence method by making use of a germanium detector both as target and detector. Due to the progress of timing techniques and equipment it became possible to differentiate between the signals from the same detector which differed in time by more than about 100 ns. The time difference of signals corresponding to the inelastic scattering of the neutron, and the de-excitation pulse is of this order and it therefore became possible to measure this time difference with a single electronic circuit processing a single source of pulses. This was the obvious reason for the much improved precision for the quoted value of the lifetime of 640,9 ± 1,1 s.

3.4 Experimental

The experiment was performed using the autocoincidence method as measured by two different detectors to determine the lifetime of this level. A standard 15% efficiency Ge(Li) detector having an energy resolution of 2,1 keV at 1,33 MeV was used in the first measurement. It is well known (see also Section 4.4.3) that these detectors deteriorate under neutron bombardment, and therefore the first detector used for testing the method was old, and had poor energy resolution. The second detector used was an IG planar detector having good timing resolution. A typical spectrum resulting from neutron irradiation of the Ge(Li) detector using a ^{241}Am/Be source is shown in Fig. 3.2. The previously mentioned asymmetric peaks at 596, 691 and 834 keV are clearly visible, representing the inelastic neutron scattering in the active volume of the detector.

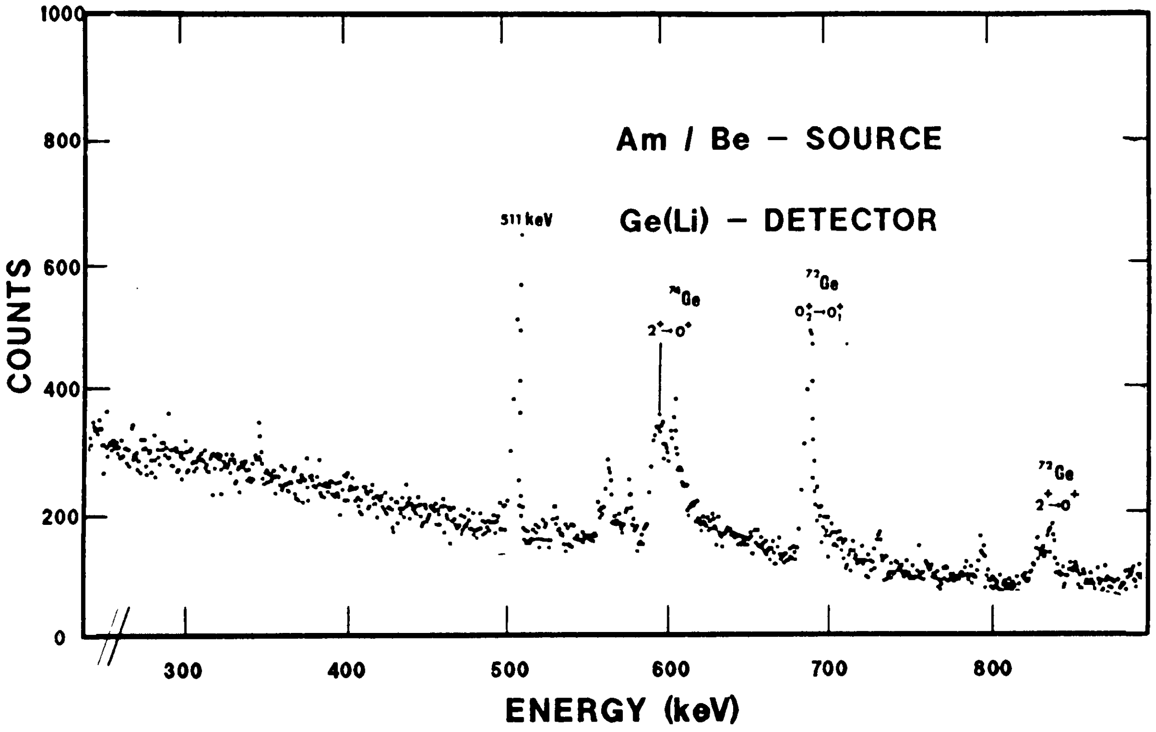

Fig. 3.2

Typical energy spectrum of germanium detector irradiated by neutrons

In terms of the characteristic response time of the detector, the electronic stopping of the ^{72}Ge reaction product provides a prompt pulse (typically less than 10^{-14} s) which is summed with the signal derived from the decay of the excited state at a subsequent time, dependent on the lifetime of the state, leading to the characteristic asymmetric peak with high energy tail. The separation of the two pulsed components therefore provides a direct method for the measurement of the lifetime of the excited state.

In determining the lifetime of the first excited state in ^{72}Ge the internal conversion process provides definite advantages as practically 100% efficiency of detection is obtained. These signals can be separated electronically for time differentials of the order of 1 s or more relating to the full charge collection time of the Ge(Li) detector. This is the result of a first order calculation using the mobility of electrons (0,38 $\frac{m^2}{Vs}$) and holes (0,18 $\frac{m^2}{Vs}$) for a cylindrical symmetric volume, as found in the co-axial Ge(Li) detector used. These mobility values are for room temperature, but should give an indication of full charge collection time of the detector. The largest path length for the slower charge (holes) is of the order of 2 cm, and with an applied voltage of 5 kV this leads to a collection time of about 200 ns. Differentiation should be made between logic timing pulses and analog energy pulses. Timing pulses are gained using the leading edge of the signal, essentially corresponding to measuring the first charge arriving at the electrode, with resolution typically 5 ns. Signals where the total energy deposited in the detector is measured however, depend on the integrated charge measured. Obviously there is a large difference in time resolution characteristics between these signals.

The simple electronic diagram used is illustrated in Fig. 3.3. The detector was bombarded with neutrons (thermal energy up to 11 MeV) from a ^{241}Am/Be source. Signals from the detectors were preamplified and amplified with short amplifier time constants, typically 0,5 s. This provided a sufficient degree of energy resolution of spectra (10 keV at 1,33 MeV) so that energy windows could be established on single channel analysers (SCA) which provided the timing signals. One SCA was set to cover the energy range from 20 keV to 300 keV, appropriate to the response of the recoiling germanium nucleus, recognising that the signal response of the detector to the heavy recoil nucleus is not equal to unity but closer to 0,4[Br84] as a result of the pulse height defect (see discussion in Section 4.8). The signal due to the stopping of the 0-600 keV recoil nucleus should therefore occur in the energy interval 0 keV to 250 keV.

The second single channel analyser window was set to cover the energy range of 670 keV to 710 keV, corresponding to the full energy response of the internally converted electron decay of the 691 keV level, i.e. the delayed signal.

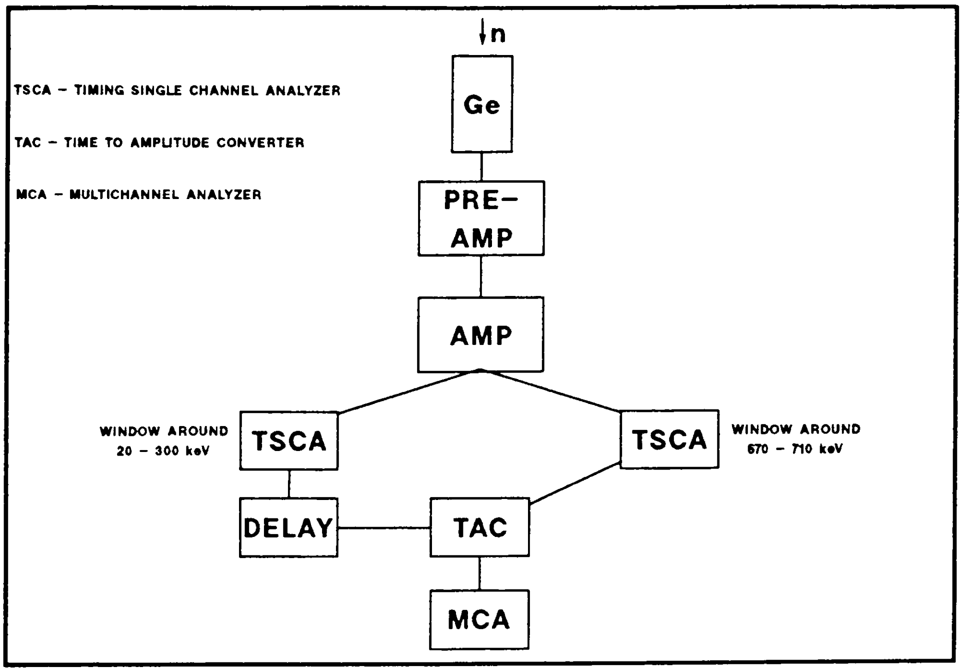

Fig. 3.3

Electronic circuit used in the delayed autocoincidence measurement

For electronic convenience this signal was used as the start signal for a time-to-amplitude converter, while the recoil nucleus signal, suitably delayed, was used as the stop signal. Optimisation of count rate and signal to noise ratio was established experimentally using a suitable amount of heavy metal to shield the detector from the overwhelming number of direct gamma ray events generated from the source in the detector. The TAC signal was fed into a multichannel analyser, where the spectra were accumulated and stored in a computer for subsequent analyses.

3.5 Results

The result of a typical TAC spectrum so generated with the Ge(Li) detector is shown in Fig. 3.4 covering 5 half lives. The analysis of the data was obtained by fitting an exponential plus constant background curve with a least squares routine using the Marquardt iteration scheme. A typical fit to the data with r = 0,998 is shown in Fig. 3.5. To establish the "cut-off" position at short time differences where the electronic signals become inseparable, points close to this region were added one at a time to the data points being analysed up to where the result was affected. The calibration of the time axis was achieved using standard delay units which were accurate to << 1%.

A double exponential plus constant background curve was fitted to the data, but did not provide better fits to the data.

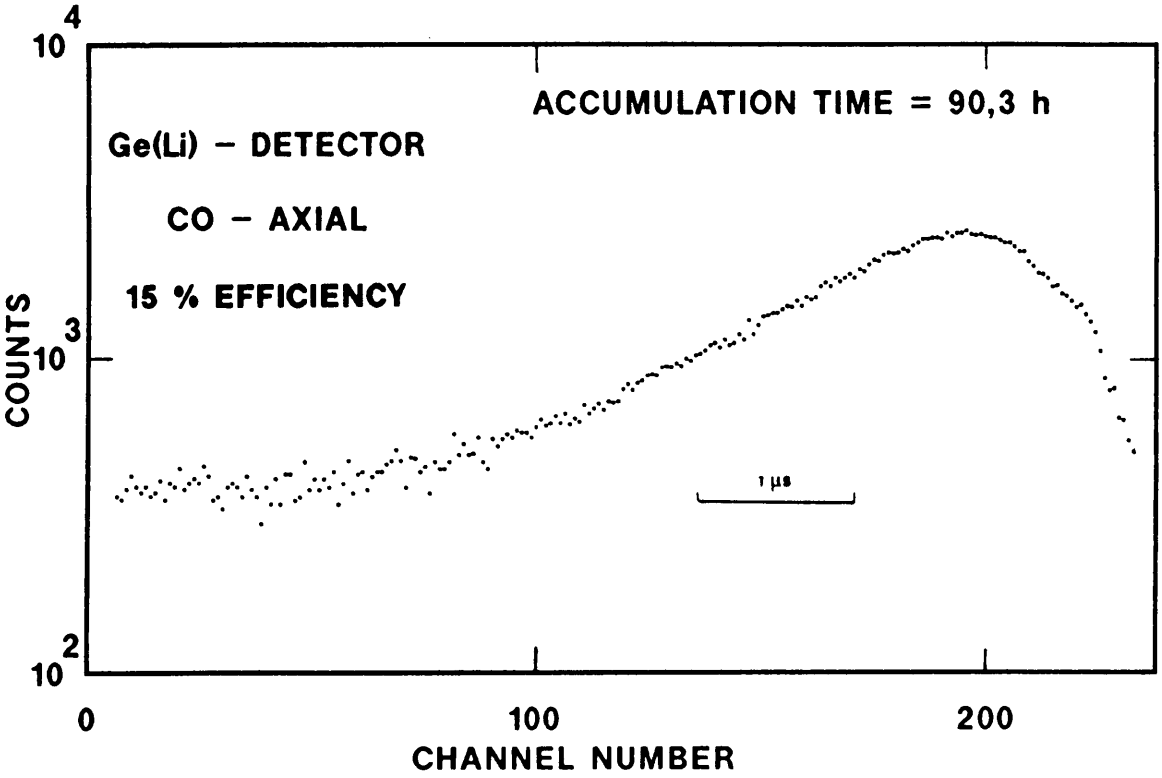

Fig. 3.4

Time spectrum obtained in the delayed autocoincidence method with a Ge(Li) detector

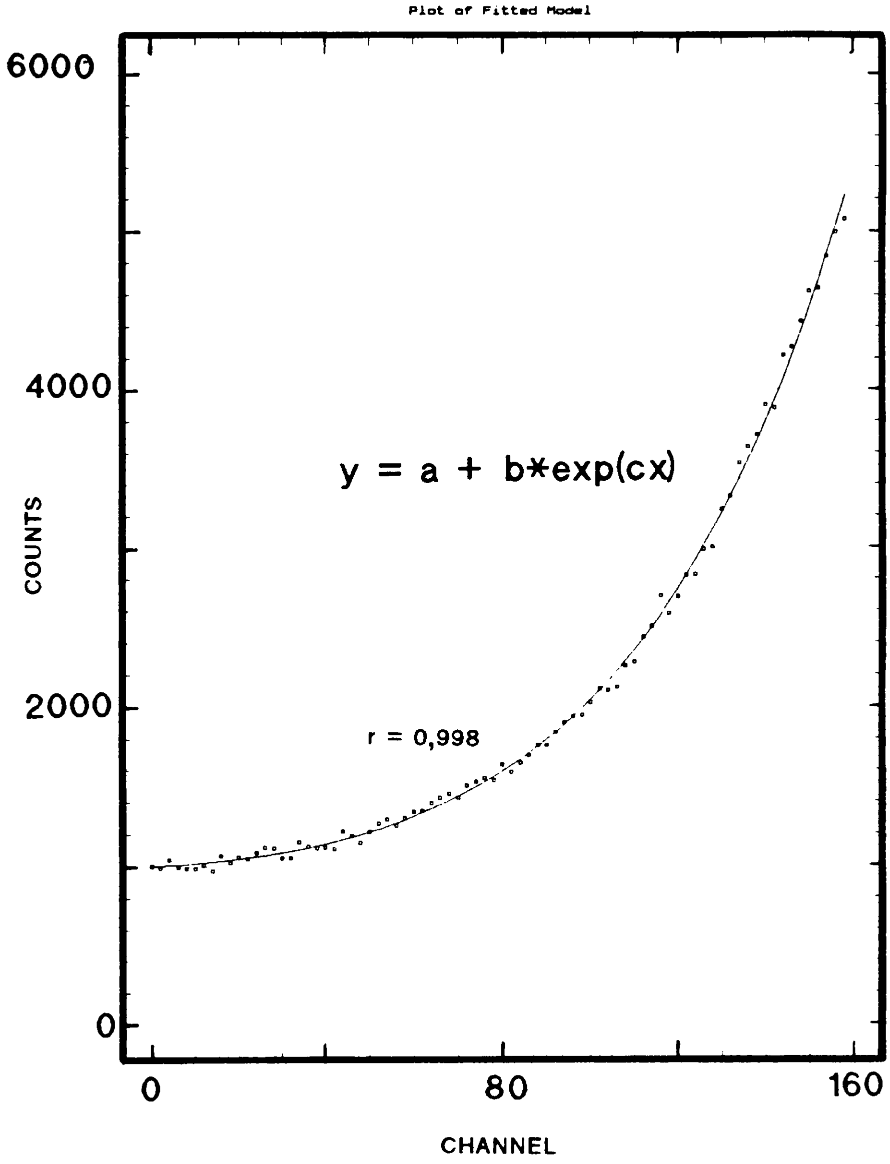

Fig. 3.5

Non-linear least squares fit to data obtained with data points close to the cut-off region neglected

The Ge(Li) detector was used for 10 individual runs using slightly different energy windows in each case which led ultimately to an average value extracted for the half life of 434 ± 5 ns. The same process was repeated with measurements using the planar IG detector. A typical spectrum is shown in Fig. 3.6. This detector was also used for 10 individual runs with the subsequent averaged result of 440 ± 4 ns.

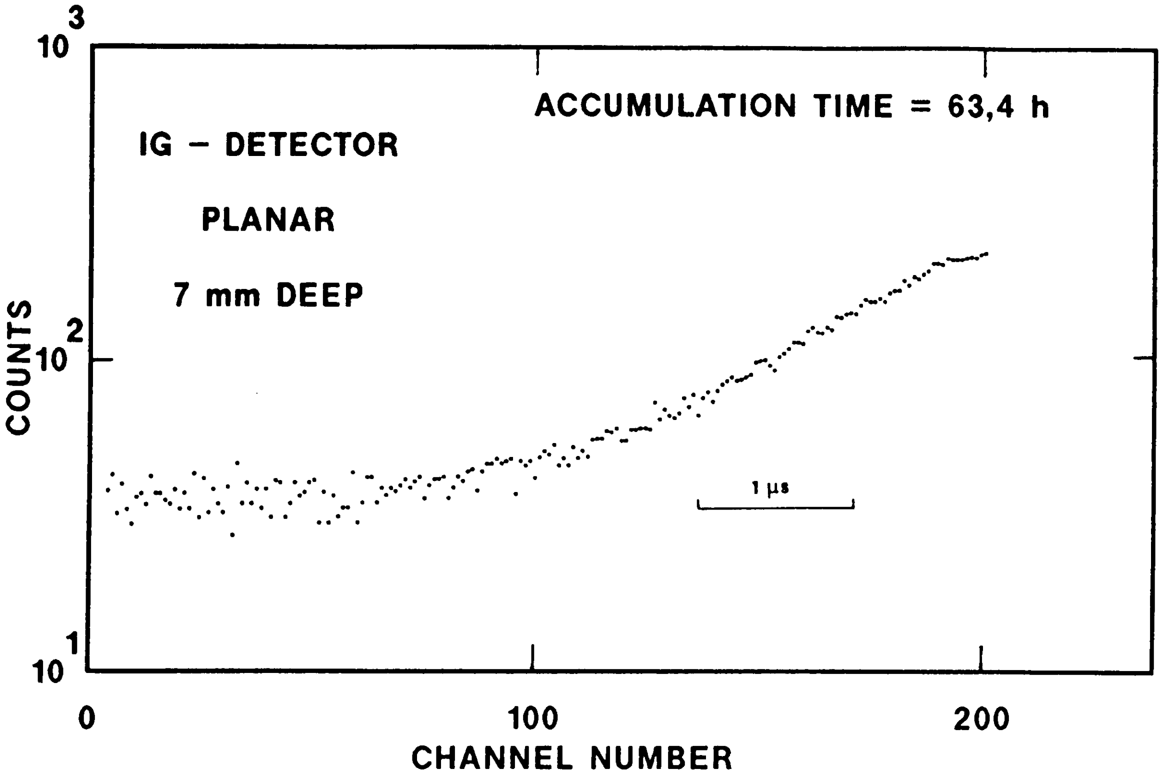

Fig. 3.6

Time spectrum obtained in the delayed autocoincidence method with a planar IG detector

This second set of measurements was made to establish any effect of two different detector geometries on the result. A small planar detector has better timing characteristics, which would enable the use of more events occurring closer to each other in time which the large detector would not be able to distinguish. The smaller volume, however, leads to smaller efficiency with resulting poorer statistics, which represented an important consideration in these low count rate measurements. The different charge collection times are clearly seen in the results (Fig. 3.4 and Fig. 3.6) from the two detectors in the cut off region where the signals become inseparable. The lower efficiency of the IG detector required longer (order of magnitude) accumulation times.

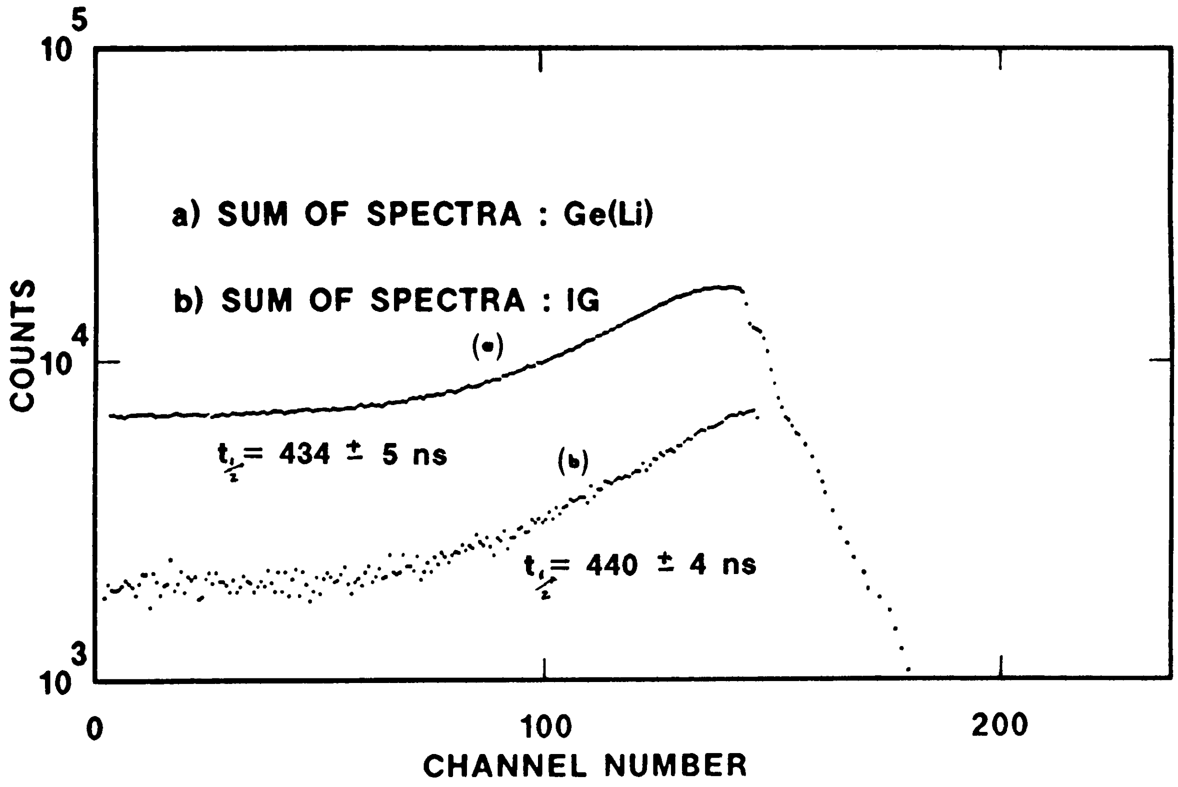

Fig. 3.7

Sum of all individual runs on a) Ge(Li) detector, and b) planar IG detector

The summed results of all runs for both detectors are shown in Fig. 3.7 and the final result of 437 ± 5 ns is added in Fig. 3.8 in a resumé of the previous measurements.

This result is within two standard deviations with respect to the most recent determination of the lifetime of this state of 444.2 ± 0,8 ns, and although not as precise, demonstrates the auto coincidence method of lifetime determination.

A small improvement electronically would have been to use a standard fast slow coincidence system. Better statistical results would obviously also be obtained with longer counting times, but the threat of radiation damage prevented this action. Total fluence of neutrons incident during measurements on these detectors was of the

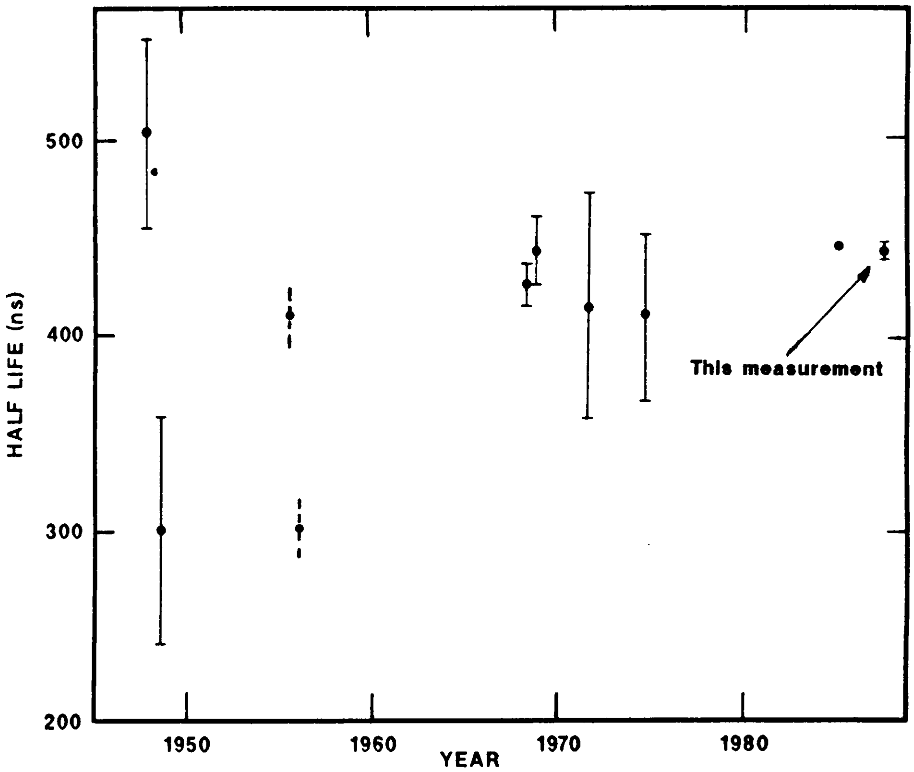

Fig. 3.8

Resumé of measurements including this result order of $10^9/cm^2$ compared with 10^{11} neutrons/cm^2 necessary to see damage effects. With the detectors used no degradation of energy resolution due to radiation damage was detected (although the Ge(Li) detector had been previously used in neutron environments).

3.6 Conclusion

The delayed autocoincidence method has led to a vast improvement in the precision of lifetime determination of the 691 keV isomeric level of ^{72}Ge having a relatively long lifetime (>400 ns).

The aim of this measurement was to measure the lifetime of the level and establish the accuracy obtainable using the auto coincidence technique. The result ultimately attained did not match the quoted accuracy of the previous measurement [Br84] and the absolute value deviated by slightly more than the error determined.

Seen in perspective the error of ±0,8 ns quoted in the previous measurement might well be optimistic as the fit to this data was extremely dependent on the choice of fitting parameters. This is realised by the fact that the addition of a second exponential to the fitting parameters of a constant plus exponential function results in very little alternation in the degree of fit, but with a difference of 1 to 2 ns in the resulting lifetime. When this uncertainty is incorporated in our data it results in a limit of precision of at least 1 ns, excluding other errors. The uncertainty in the result is also determined by the choice of the result of the statistical average and deviation of the 20 individual measurements. This resulted in a bigger error bar being allocated to the derived lifetime when compared with an analysis of the summed spectrum of all these measurements.

This technique has proved to be a very precise way of determining the lifetime under study.

4 NUCLEAR REACTIONS WITHIN SILICON SURFACE BARRIER DETECTORS INDUCED BY NEUTRONS

4.1 Introduction

Silicon solid state semiconductor detectors have been in use as particle detectors for nearly three decades now, and have proved themselves for general application in this field. These detectors can, in addition, be used to observe nuclear reactions occurring within the active volume of the detector. This method is of course only useful when the impinging particle can penetrate the detector, and for this purpose neutrons are well suited. Neutron reactions result in the production of charged particles, specifically two channels being of importance here, i.e. (n,p) and (n,α) reactions. Since in this case the energies of both emergent particle and residual nucleus are added and measured, unique identification of the various states and energies of the residual nuclei is possible, knowing the total energy of the neutrons and the respective Q-values.

The need to monitor fast neutron fluxes led to a study of the nuclear reactions within silicon surface barrier detectors induced by neutron bombardment. Different (n, particle) reactions are observable in a set up where the detector is used both as target and detector simultaneously. This method has previously been applied[Co62, Ai62, Co62A, Mo66, Mi67, Gr69, Mi71] and interesting results and features have been observed.

When reactions take place within a detector the efficiency of detection is essentially equal to unity if edge effects are ignored, since a detection solid angle of 4π is subtended. This supposition is only valid in the case of large volume detectors having deep (typically >1 000 µm) depletion layers, and both large volume and small volume detectors were used in these measurements to study depletion depth dependent effects.

This vast simplification when measuring with large volume detectors enabled the measurement of absolute neutron cross sections and excitation functions in the original measurements[Co62, Ai62, Co62A, Mo66, Mi67, Gr69, Mi71] or in subsequent use as accurate neutron flux monitors. In the case of a silicon detector the most relevant reactions are: $^{28}Si(n,p)^{28}Al$, $^{28}Si(n,\alpha)^{25}Mg$, $^{29}Si(n,p)^{29}Al$ and $^{29}Si(n,\alpha)^{26}Mg$.

This method has also proved itself as a useful way of measuring not only the neutron flux, but also the energy of energetic neutrons (typically >10 MeV) produced in nuclear reactions. The energy of less energetic neutrons can also be measured, although with less precision. An example[Mi67] of a neutron energy measurement obtained via this method is the determination of the ground state Q-value for the $^{10}B(^3He,n)^{12}N$ reaction (E_n = 11,24 MeV) of 1561 ± 9 keV. The excitation energies of the excited states of ^{12}N were found to be 994 ± 20 keV and 1220 ± 30 keV. Such measurements, while in no way comparable with accuracies obtained by gamma ray spectroscopy, are possible with careful and accurate calibration measurements.

These measurements were not directed towards the re-measurement of cross sections or excitation functions, but aimed specifically at the need for the calibration of silicon surface barrier detectors for ultimate use in fast neutron flux measurements.

4.2 Neutron Reactions in Si

There are three naturally abundant isotopes of Si in silicon and all three contribute reaction products. The most important reactions are tabulated in Table 4.1 together with Q-values and cross sections at a neutron energy of 14,5 MeV.

Table 4.1

Isotopic abundance and reaction parameters of silicon

Isotope	Natural abundance (%)	Reaction	Q-value (keV)	Cross section (mb) (E_n = 14,5 Mev)	
^{28}Si	92,21	^{28}Si(n,α)^{25}Mg	-2652,6±3,2	35	[Mi71]
		^{28}Si(n,p)^{28}Al	-3852,1±4,2	14,1	[Mi71]
^{29}Si	4,70	^{29}Si(n,α)^{26}Mg	- 32,7±3,9	-	
		^{29}Si(n,p)^{29}Al	-2893 ±7	112	[Ne76]
^{30}Si	3,09	^{30}Si(n,α)^{27}Mg	-4210 ±5	0,06	[Ne76]
		^{30}Si(n,p)^{30}Al	-6510 ±250	5	[Ne76]

The relatively high negative Q-values and small cross sections of ^{30}Si are due to pairing that gives ^{30}Si higher binding energy. These larger negative Q-values result in peaks originating from the excited states of residual nuclei in the reactions ^{30}Si(n,p)^{30}Al and ^{30}Si(n,α)^{27}Mg that are lower in energy, and thus interfere with excited states of ^{25}Mg, ^{28}Al, ^{26}Mg and ^{29}Al. The small cross sections limit the contributions of these states to being minor peaks in energy spectra.

For the purpose of description of peaks in spectra obtained in these measurements it is defined, for example, that the reaction

$^{28}Si(n,\alpha)^{25}Mg$ leading to the ground state of ^{25}Mg is written $^{28}Si(n,\alpha_o)^{25}Mg$ and the peak in the spectrum would then be denoted by α_o. Similarly the reaction leading to the first excited state of ^{25}Mg is represented by $^{28}Si(n,\alpha_1)^{25}Mg$ and the peak denoted by α_1. The same applies for the different reactions $^{28}Si(n,p)^{28}Al$ where, for example, $^{28}Si(n,p_o)^{28}Al$ is the reaction leading to the ground state of ^{28}Al, and the peak is denoted by p_o.

The peaks resulting from the reactions $^{29}Si(n,\alpha_i)^{26}Mg$ and $^{29}Si(n,p_i)^{29}Al$ are primed $(\alpha'_i;p'_i)$ for distinction, and the peaks from $^{30}Si(n,\alpha_i)^{27}Mg$ and $^{30}Si(n,p_i)^{30}Al$ are double-primed $(\alpha''_i;p''_i)$, but will only be indicated in exceptional cases due to their small spectral contributions.

4.2.1 Fluctuation analysis

Previous work[Co62, Co62A, Co63, Mo66A] on the measurement of excitation functions and cross sections for the levels of ^{25}Mg and ^{28}Al has endorsed the fact that these reactions proceed via compound nucleus formation. This followed from the result of Ericson fluctuation analyses[Co62, Co62A, Co63, Gr69, Mi83] on the highly structured excitation functions for the different levels. Fluctuation theory was published originally in 1960 by Ericson[Er60] and has proved to be very useful in describing reactions proceeding via compound nuclear formation in energy regions having overlapping levels. Ericson proposed that if the mean widths of excited levels in the compound nucleus are large compared with the spacing of the levels, i.e. $\Gamma/D \gg 1$, these fluctuations might be interpreted as interference effects among the different states of the compound nucleus. From these fluctuations it is then possible to deduce the mean lifetime of the compound nucleus according to the Heisenberg uncertainty principle $\Gamma\tau \sim \hbar$.

In these measurements it was shown that the level widths were indeed bigger than the spacing of levels, covering essentially the whole energy range from En = 4 - 16 MeV and corresponding to excitations in the compound nucleus between 12 MeV and 25 MeV in ^{29}Si. The value of τ has also been determined[Co62, Co63] in this interval and found to be $\sim 10^{-20}$ s.

The compound nucleus concept is illustrated simply in Fig. 4.1 where a neutron is captured by a ^{28}Si nucleus, the compound nucleus ^{29}Si exists for a short time ($\sim 10^{-20}$ s) and then disintegrates to the reaction products.

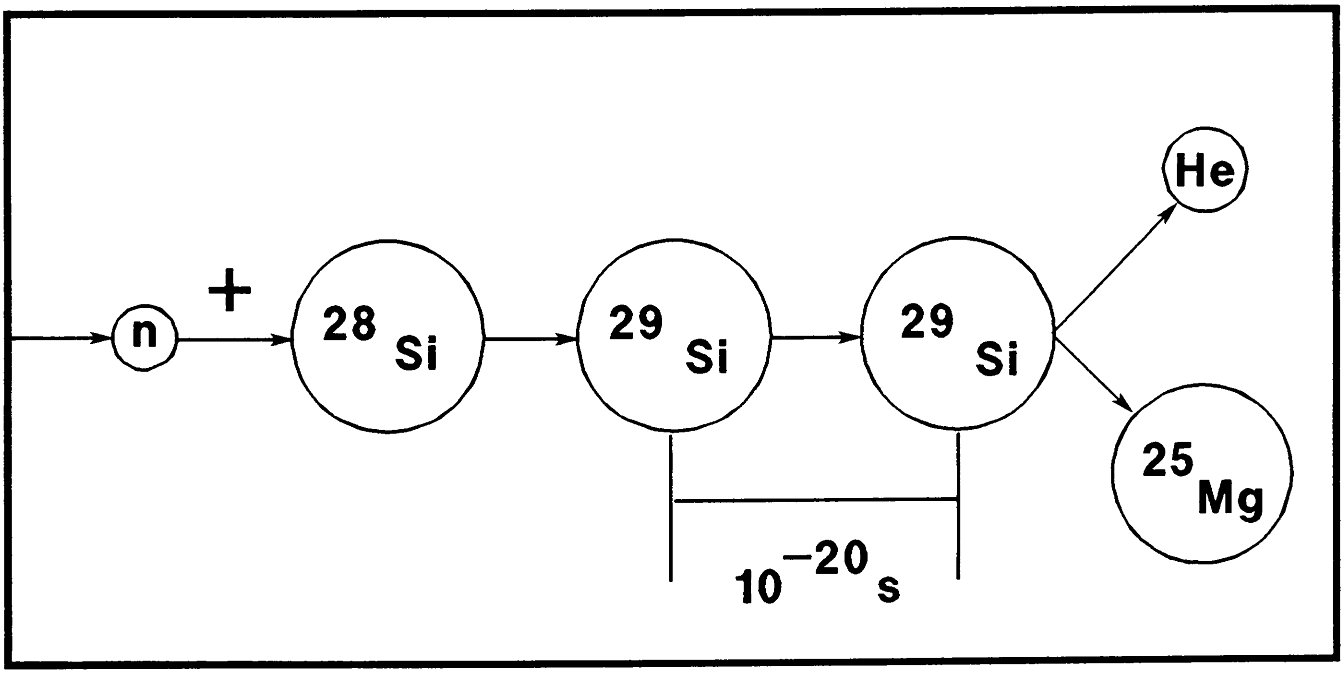

Fig. 4.1

Typical compound nucleus reaction

4.3 Source of neutrons

From the vast variety of neutron producing reactions, three positive Q-value reactions are probably best known for producing energetic neutrons with charged particle accelerators:-the $T(d,n)^4He$, $^9Be(d,n)^{10}B$ and $D(d,n)^3He$ reactions with Q-values of 17,592 MeV, 4,361 MeV and 3,267 MeV respectively.

The large positive Q-value which leads to production of high E_n (plus the large range of energies available kinematically) led to the choice of the $T(d,n)^4He$ reaction. This is specifically the energy region of interest for future fusion studies.

The kinematics for the reaction are shown in Fig. 4.2 and illustrate the angle dependent neutron energy variation for deuteron bombarding energies of 1.3, 1.5 and 1.7 MeV. Note the convergence of the different neutron energies at θ_{lab}~120°. The range of neutron energies as a function of angle available for E_d = 3,0 MeV is E_n = 11,89 (180°) to 19,61 MeV (0°). The neutron energy can thus be selected by using different machine energies or by selection of reaction angle.

At the energies obtained with this reaction, relativistic effects do play a significant role in the determination of neutron energies. As an example the neutron energy at θ_{lab} = 110° and E_d = 1,5 MeV is 13,792 MeV in the classical calculation, while in a relativistic treatment E_n = 13,738 MeV, which indicates an error of 54 keV in the classical approximation. This error is comparable to other sources of error in these measurements and should not be neglected. All calculations of kinematic parameters were subsequently made in a relativistic scenario which is often neglected by researchers on low energy accelerators.

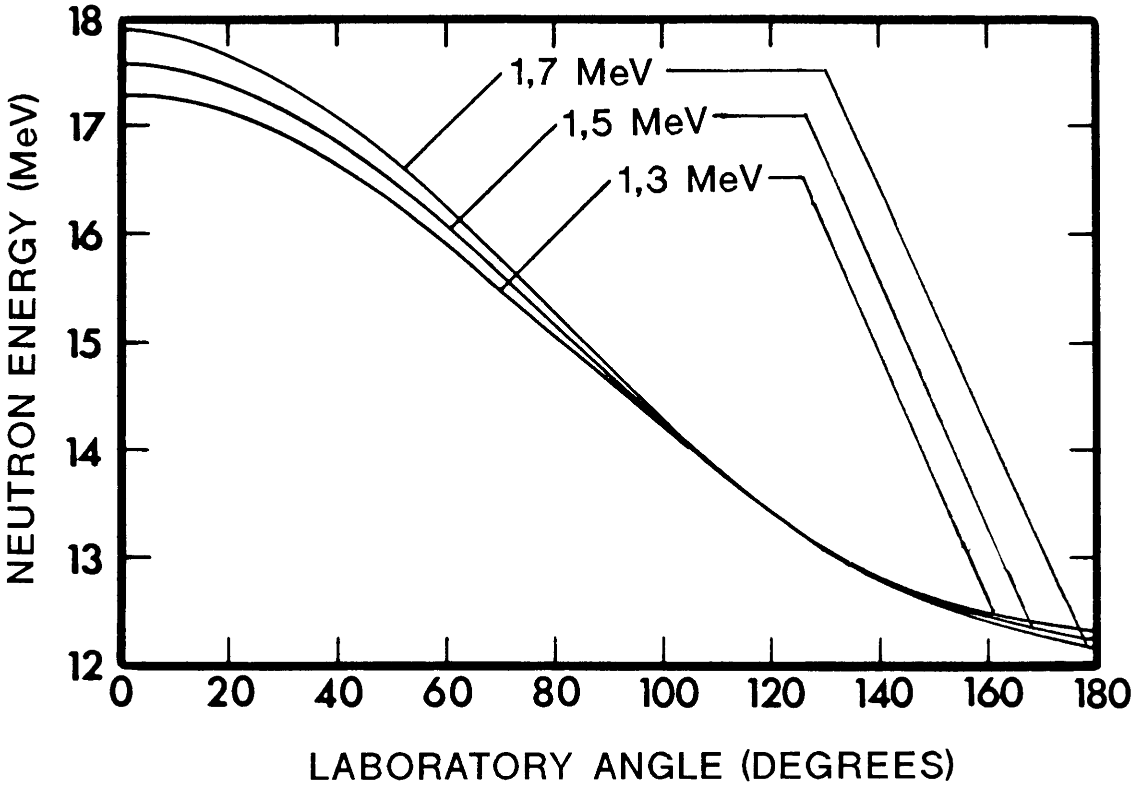

Fig. 4.2

Kinematics of the $^3H(d,n)^4He$ reaction (Q = 17,592 MeV) for 3 incident deuteron energies

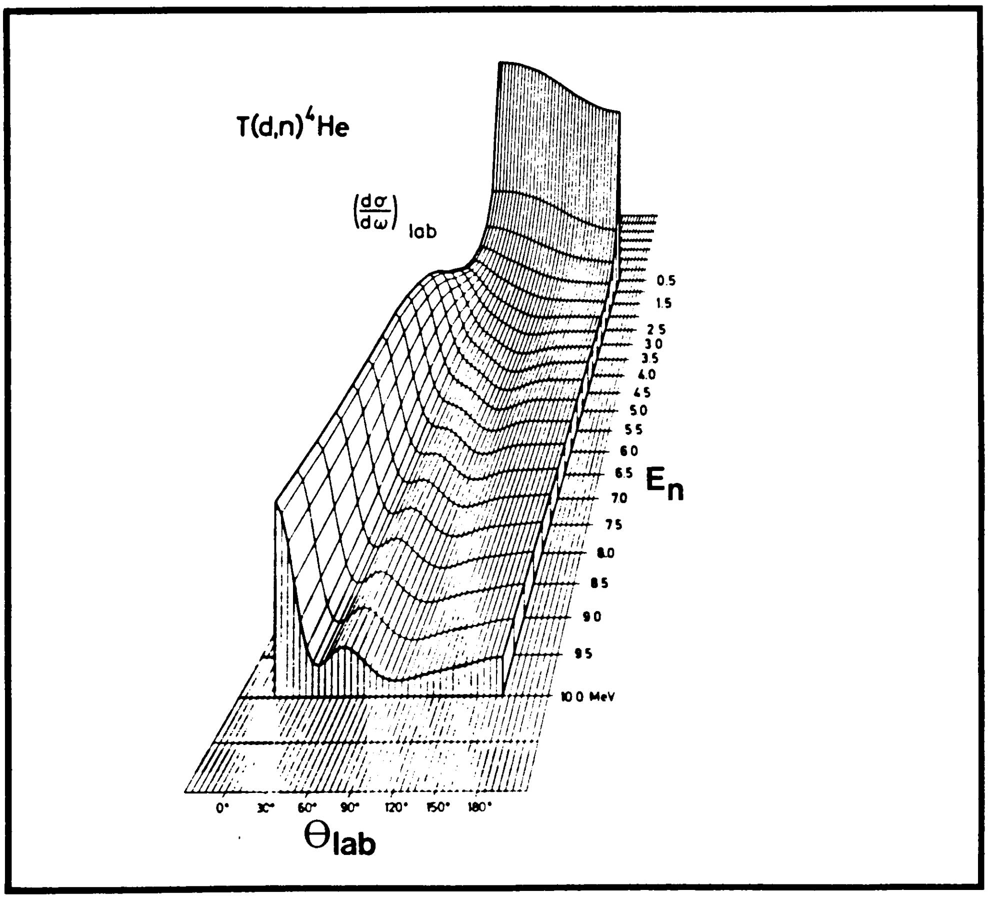

Fig. 4.3

Experimental cross section of the $T(d,n)^4He$ reaction [Li73]

The differential cross section for the $T(d,n)^4He$ reaction[Li73] is shown in Fig. 4.3. The relatively high cross sections at lower deuteron energies lead to a large yield of neutrons which are ideally suited for fast neutron activation analysis and in a limited way to study reactions in materials for use in fusion reactors.

4.3.1 Choice of target

A titanium tritide (TiT) target was selected for use. This selection was based on the fact that the target was thin (1 μm effective) and the titanium represented a strong matrix, which is excellent for hydrogen storage, which was necessary for long target lifetime.

Tritium is radioactive and decays by β-emission to ^3He (τ = 12.6 years) which causes the tritium content in the target to decrease with age. The target used in these measurements was about 20 years old which resulted in about 30% of the original tritium content being present in the target. In addition, a considerable amount of daughter product ^3He probably resided in the target.

Although a gaseous tritium target is in many cases preferable (better yield per thickness, no metal) practical health monitoring problems limited our use to a TiT target.

Problems are encountered in the use of such targets since high beam currents can lead to high temperatures in the target resulting in diffusion through and ultimate loss of tritium from the matrix. Adequate cooling was achieved by spraying water and air onto the back of the target. Regular measurements of the neutron flux with a BF_3 long counter positioned at $\theta_{lab} = 0°$ were made to ensure that the neutron yield remained constant and that no tritium was lost.

The spread in neutron energy resulting from the $T(d,n)^4He$ reaction is dependent on several parameters including the depth distribution and possible existence of inhomogeneities in the tritium content in the target as was pointed out by Gunnerson and James[Gu60]. They measured the distribution of tritium inside their solid TiT target, results of which are shown in Fig. 4.4.

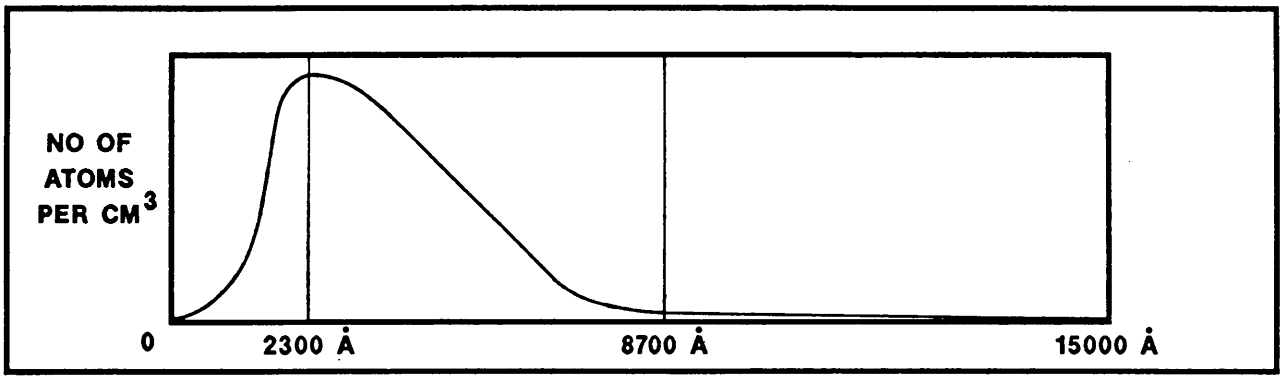

Fig. 4.4
Distribution of tritium inside target[Gu60]

It is also well known that the tritium depth distribution alters with time and especially so during beam bombardment. The spread in neutron energy due to effective target thickness is therefore complex, although most of the tritium is usually situated near the surface within the top μm of the target. In this measurement the effective thickness was assumed to correspond to less than 50 keV degradation of 1,5 MeV deuterons, corresponding to an effective target thickness of 1,5 μm. Stopping values for mixed elemental samples [An77] were obtained from the formula[Gu60].

$$\frac{dE}{dx} = \frac{48}{48 + 3N} \frac{dE}{dx_{Ti}} + \frac{3N}{48 + 3N} \frac{dE}{dx_{T}} \qquad (4.1)$$

$$\sim \frac{dE}{dx_{Ti}} \qquad \text{for } N = 0.3 \qquad (4.2)$$

where N is the tritium atomic ratio per titanium atom.

4.3.2 Associated particle counting and competing reactions

When using the T(d,n) reaction as a neutron source, the counting of associated alpha particles is done when absolute cross sections are required and excitation functions measured. A particle counter is placed in an evacuated arm viewing the tritium target beam spot. The energy of the associated alpha particle at the specific detection angle is defined by the kinematics of the reaction. From this value the peak in the energy spectrum produced by the particle counter can be identified, and the neutron flux can be calculated knowing the number of counts in this peak. Another novel use of associated particle counting is to collimate high energy neutron beams with coincidence measurements between neutrons and associated particles [Sc69].

A problem that is encountered when using the T(d,n)^{4}He reaction is a build-up of implanted deuterium in the target and the competing reaction D(d,p)T coming into effect. The Q-value of this reaction is 4,032 MeV and for E_d = 1,5 MeV and a particle counter at 80° with respect to the incident deuterons, the energy of the proton released is 3,688 MeV while the energy of the associated He nucleus resulting from the T(d,n)^{4}He reaction is 3,680 MeV. The difference of 8 keV causes the peaks corresponding to these particles to interfere totally as a result of target thickness even when good detector energy resolution is obtained and must be taken into account when associated counting techniques are used. Another competing reaction exists from the presence of the ^{3}He from T-decay, of which special care should be taken when old targets are used. The Q-value for the reaction ^{3}He(d,p)^{4}He is 18,341 MeV, which leads to an alpha energy of 3,630 MeV in the same geometry as discussed before. The peak corresponding to these particles is therefore situated at 50 keV lower on the energy scale. Good energy resolution (~15 keV) can eliminate interference problems, in this case only for extremely thin tritium targets for which the yield is correspondingly small. These interferences occur to different degrees at different angles of detection.

4.3.3 Selection of acceptance angle θ_{lab}

The two major contributions to the neutron energy spread as a function of angle of emission (lab) of the neutrons are the spread in deuteron beam energy (caused mainly by target thickness, uneven occurrence of tritium in titanium titride and to a negligible extent the fluctuation in machine energy) and the angular acceptance geometry. These two contributions were calculated for E_d = 1,5 MeV, and the relative and total contributions are shown in Fig. 4.5.

The spread in detection angle $\Delta\theta$ was taken as 0,3° and the uncertainty in effective beam energy in a 1 μm thick target, E_d, was taken as 32 keV. These restrictions are typical for a very thin TiT target. Care should be taken when calculating the total spread in neutron energy, as the total spread is not simply the sum of the two contributions, but is also a function of the difference in the slopes of the plot of E_n versus laboratory angle for firstly machine energy E_d, and secondly for the decreased deuteron energy after moving through the target. For a target thickness of 1 μm the effect is negligible, but for thicker targets (>5 μm) or lower bombarding energies (<1 MeV) the effect becomes significant.

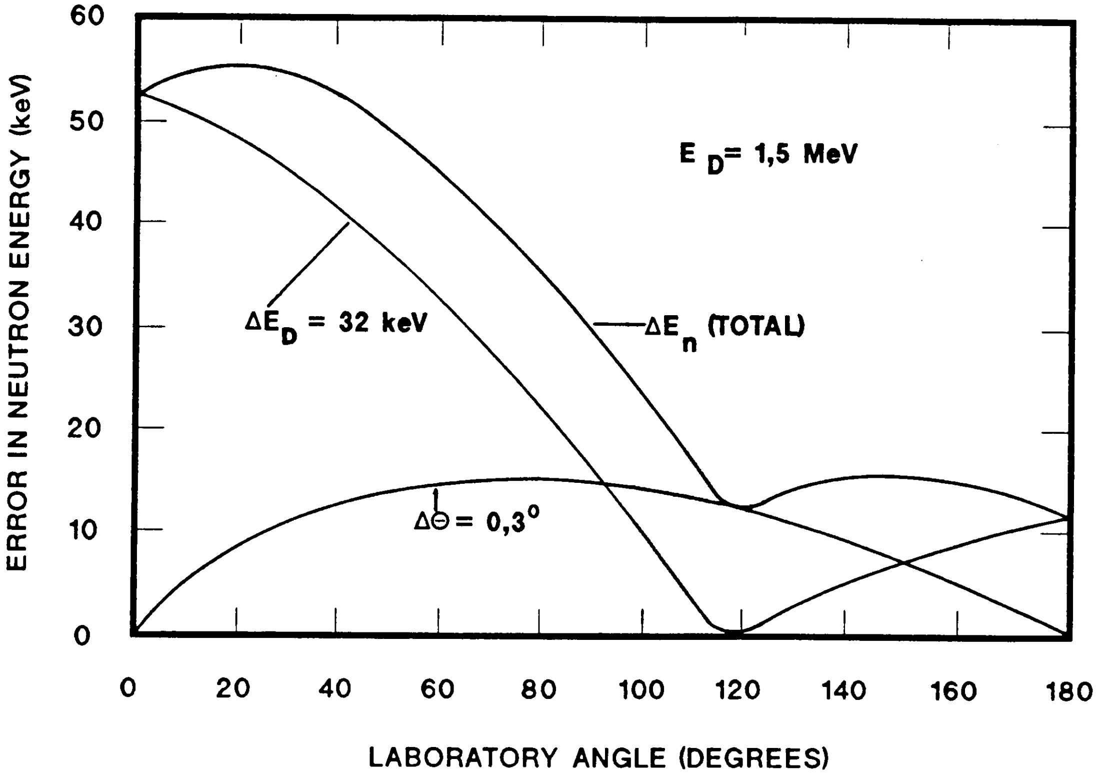

Fig. 4.5

Neutron energy resolution as a function of angle (laboratory frame) based on effective target thickness (1 μm) and angular considerations ($\Delta\theta = 0{,}3°$)

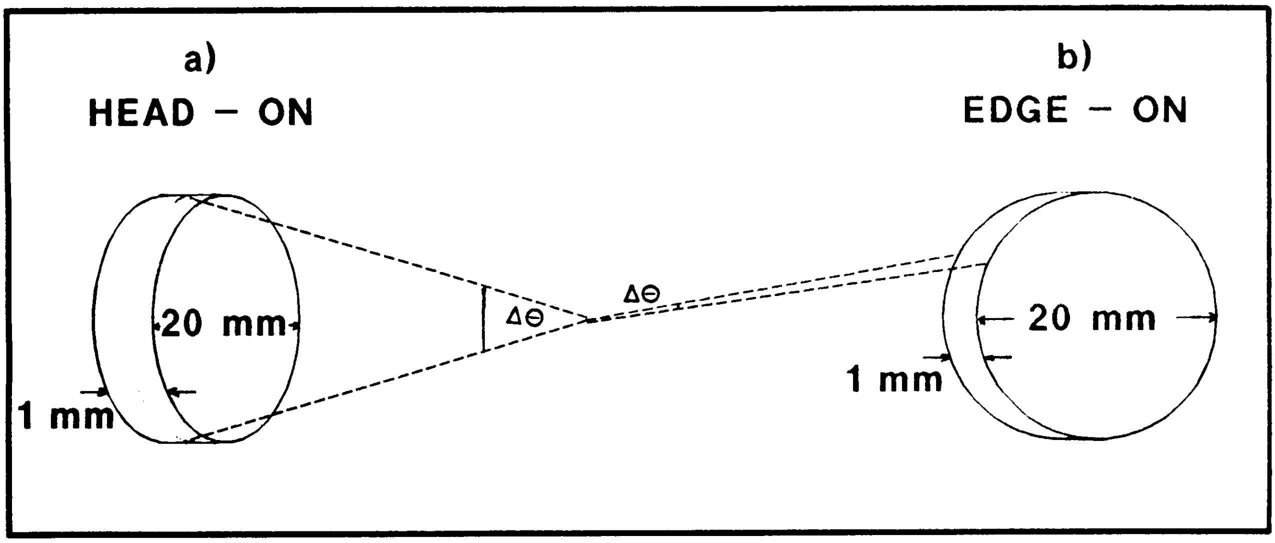

Fig. 4.6

Finite detection angle as seen in (a) Head-on geometry (b) Edge-on geometry

Silicon detectors used were typically between 100 µm and 1 mm depth and of 20 mm diameter. The finite acceptance angle geometry can only be as small as 0,3° when the detectors used for the reaction studies, are in the edge-on position as opposed to the traditional particle detection head-on position as shown in Fig. 4.6(a) and (b). The fact that neutrons are the impinging particles offers minor volume limitations for this position, and the acceptance angles for 1 000 µm, 300 µm and 100 µm deep detectors 12 cm away from the tritium target assuming no azimuthal dependence, are 0,5°; 0,14° and 0,05° respectively. The inherent spread in neutron energy, due to a kinematically induced spread over the spread in angle is, to a first approximation, linearly related to $\Delta\theta$.

The choice of 110° as detection angle used in these measurements was based on the kinematics of the $T(d,n)^4He$ reaction as qualitatively discussed in Section 4.3. The energy of the neutron is classically determined by[Mo60]:

$$E_n = \frac{m_d m_n E_d[(\eta + \cos^2\theta)^{\frac{1}{2}} + \cos\theta]^2}{m_n + m_{He})^2} \qquad (4.3)$$

where

$$\eta = \frac{(m_n + m_{He})(m_{He} - m_d + m_{He} Q)}{m_d\, m_n}, \qquad (4.4)$$

To obtain the angle where the change in neutron energy as a function of beam energy is a minimum, eq. 4.3 must be differentiated with respect to E_d, and set to zero.

The result is schematically shown in Fig. 4.7, and the angle where equals zero was calculated from [Ts84]

$$\cos^2\theta = \frac{(m_n + m_{He})(m_{He} - m_d)^2}{m_d\, m_n\left(\frac{m_{He} Q}{E_d} - m_{He} + m_d\right)} \qquad (4.5)$$

to be 118,15°. This result was checked using the full relativistic calculations, which differed only in the third digit after the decimal point.

The best overall neutron energy resolution (as indicated in Fig. 4.5) including finite target thickness effects is therefore to be obtained at θ_{lab} slightly greater than 118,15°. The choice of θ_{lab} = 110° for the experiment was based purely on practical reasons for accurate placing and mounting of other larger detector systems which were to be calibrated.

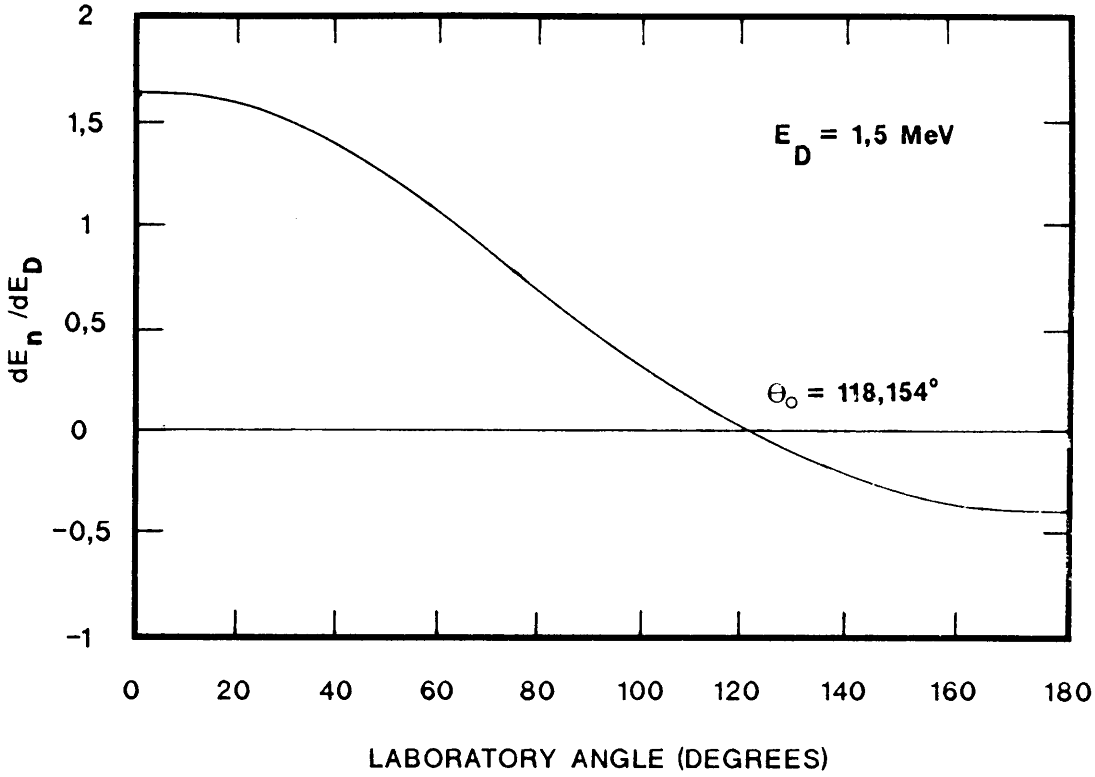

Fig. 4.7

$\frac{dE_n}{dE_d}$ as a function of laboratory angle

4.3.4 Selection of beam energy

The choice of beam energy (E_d = 1,5 MeV) was also made with the two main contributors to neutron energy spread as a function of beam energy in mind, namely the constant finite acceptance angle which leads to neutron energy spread from kinematic considerations as a function of beam energy, and secondly the effective thickness of the tritium target. These two contributions plus the total error in neutron energy are shown in Fig. 4.8 for θ_{lab} = 110°, $\Delta\theta$ = 0,3° and a target thickness of 1 μm.

The selection of E_d = 1,5 MeV was made from a viewpoint of keeping the degradation of neutron energy in the same order as obtained via the selection of the acceptance angle, but at the highest possible beam energy to ensure that a large range of neutron energies was available kinematically.

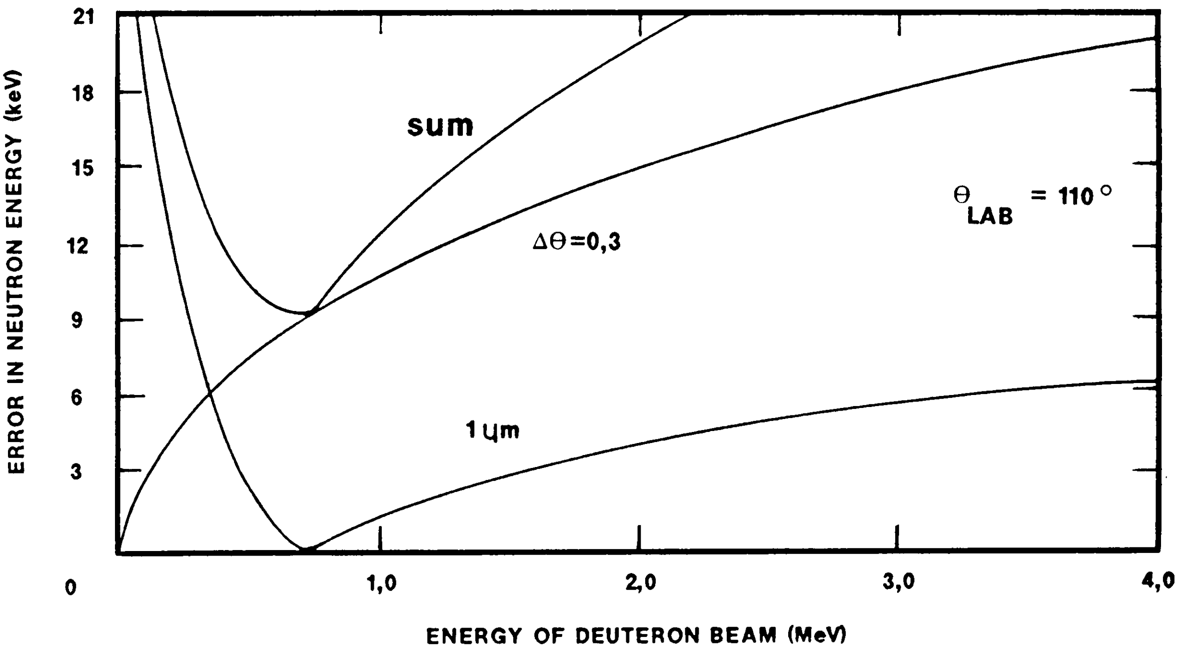

Fig. 4.8

Neutron energy resolution as a function of beam energy based on tritium target thickness (1 μm) and angular considerations $\Delta\theta$ = 0,3°

4.3.5 Competing neutron producing reactions

Another competing neutron producing reaction exists through the build-up of deuterium in the target. The reaction, $D(d,n)^3He$, has a Q-value of 3,267 MeV. However, with this comparatively low Q-value the neutron energy is ~ 4 MeV at most and the peak corresponding to the ground state of ^{25}Mg [$^{28}Si(n,\alpha_o)^{25}Mg$ reaction] occurs 11,4 MeV below the corresponding peak produced by the neutrons from the $T(d,n)^4He$ reaction, with E_d = 1,5 MeV at θ_{lab} = 110°. Therefore it is only the lower energy region of the spectrum that is affected by this reaction, and not the region of interest corresponding to much higher ($>>\alpha_{15}$) levels of the residual nuclei.

4.4 Another way of measuring neutron flux and normalisation of the neutron source

Recently a method was reported[Of88] whereby the total flux of collimated neutrons produced via the $T(d,n)^4He$ was measured by a completely different technique involving activation of a copper foil. The activity was used to calculate the neutron fluence, and thereby calibrate an NE-213 scintillator which was simultaneously irradiated by the neutrons. In this way the NE-213 scintillator could be used in determining neutron flux in subsequent experiments.

4.5 Detectors and electronics

4.5.1 Considerations involving choice and position of detectors

Whenever energy dispersive detectors are used, the aim is generally to obtain the best energy resolution to extract the most information from measurements. In these measurements there were other important factors to consider simultaneously with energy resolution, namely the effective volume (area x depletion depth) of the detector used, counting efficiency and the distance of the detector from the tritium target.

Generally, the energy resolution of surface barrier detectors improves with decreasing area and increasing depletion depth since the detection capacitance is thereby reduced. In this case of volume neutron detection there is a loss of resolution due to surface effects which depend mainly on active depletion depth and not area. An increase in volume has the effect of increasing counting efficiency. This is an important statistical consideration as only one in ten thousand 15 MeV neutrons passing through 1 mm of ^{28}Si will react[Mi67] via the reaction ^{28}Si(n,α_o)^{25}Mg. Another way to improve the counting efficiency is to increase the solid angle for detection by decreasing the distance from the tritium target to the detector. This in turn influences the acceptance angle, and therefore the spread in neutron energy, negatively. The contribution of acceptance angle to the degradation of neutron energy for a 1,5 MeV beam of deuterons was shown in Fig. 4.5 to be practically the only contributor at θ_{lab} = 120°.

With the detector in the edge-on position it is therefore clear that deep detectors offer the most advantages with these considerations in mind. A deep detector results in better energy resolution and higher counting efficiency, while influencing the acceptance angle minimally. To use this advantage to good effect, some early measurements[Mi71] involved 3 mm and 5 mm deep lithium drifted silicon detectors, but low energy tailing due to incomplete charge collection presented interference problems. The incomplete charge collection occurs from the smaller electric field strength present and subsequent charge carrier trapping in these detectors. Typical bias used for a 5 mm Si(Li) detector is 500 V, with a resulting field strength of 100 V/mm. The 300 μm surface barrier silicon barrier is biased with 120 V, which represents a field strength of 400 V/mm. The dewar mountings required to cool Si(Li) detectors to liquid nitrogen temperatures are, in addition, rather large and restrict the placing and mounting of these detectors to a certain extent.

4.5.2 Detectors used in these measurements

For comparison, three surface barrier detectors were used with specifications as stated in Table 4.2.

Table 4.2

Specifications of detectors used as neutron spectrometers

	#	Depth (μm)	Area (mm^2)	Bias
A	21 - 406F	100	450	120 V
B	22 - 399F	300	300	120 V
C	27 - 012B (Ruggedized)	1 000	450	-175 V

The three depths of these detectors were selected to investigate edge loss effects in high energy reactions such as these. These effects originate from the incomplete stopping of particles in the depletion depth and is dependent on the geometry of the detector. These effects therefore lead to the loss of especially protons that are not stopped completely in shallow detectors. For example, the reaction $^{28}Si(n,\alpha_o)^{25}Mg$ at 14 MeV neutron energy leads to a maximum energy of the alpha particle of 11 MeV. The range of such an alpha particle is 80 μm in silicon. The percentage of reactions suffering from edge effects in a detector with a depth of 100 μm is about 45 %, assuming isotropic emission (see also Section 4.9). In a detector with depth 1 000 μm these edge effects are decreased by a factor of 10. For protons from the $^{28}Si(n,p)^{28}Al$ reaction the effect is obviously much larger.

4.5.3 Energy resolution of silicon detectors used in neutron induced reactions

The energy resolution of silicon solid state detectors used in neutron induced reactions is always much worse (typically a factor of 4) than for mono-energetic charged particles alone. In these measurements the energy resolution for α-particles from a ^{241}Am source (E_α = 5,488 MeV) was 26 keV for the 300 μm deep detector, while the energy resolution at 10 MeV degraded to 175 keV when the same detector was used to study neutron induced reactions.

This degradation is mainly due to angular distribution which leads to a range of shared energies of residual nucleus and emergent particle, and in particular, to the way in which the heavy residual nucleus is stopped. Such a nucleus does not spend all its kinetic energy producing electron-hole pairs for charge collection but a large component is spent on nuclear interactions which does not lead to electron-hole pair production. In addition there is a possibility that the dense ionization column or plasma around the ionizing track prevents the clearing field from collecting charge with full efficiency. As the energies of the residual nucleus and the emergent particle are added in the detector as one output pulse, this defect in charge production is inherent in these reactions. To this defect the loss of charged particles from the active volume of the detector also contributes. There is always, in addition, a contribution of energy resolution loss resulting from the spread in neutron energy which results from finite detector geometry as well as the fact that the source of neutrons is not a point source, but a function of the finite beam spot size on the tritium target.

It is paramount to keep in mind that radiation damage occurs and considerably worsens the energy resolution of solid state detectors in experiments with fast neutrons. The damage becomes visible after 10^{10} fast neutrons/cm^2 and terminally effective after a fluence of about 10^{11} fast neutrons/cm^2 [Da88]. Care must therefore be taken when using these detectors in neutron energy measurements as these detectors are relatively expensive. With the detectors used the flux of fast neutrons through the detectors was 10^5 neutrons/(cm^2.s) and run times totalling less than 1 000 minutes meant radiation damage should not have occurred and indeed no loss of resolution was recorded.

4.5.4 Contributions of other radiation sources to energy spectra

Compton scattering of gamma rays both in the detector and from surrounding materials is also detected by the detector and leads to the continuous background in the energy spectrum. There are different sources of background to be considered when studying a specific reaction, namely natural background (^{214}Bi, ^{214}Pb, ^{40}K etc), and gamma rays from the reaction being studied. Local shielding can be used to reduce the natural background from reaching the detector, but this was shown not to be important in this study as these gamma rays are of comparatively low energy and did not contribute to the spectrum.

The most important contributor in a different way results from detection of gamma rays from the reaction under study. It could happen for example that in the reaction $^{28}Si(n,\alpha_1)^{25}Mg$, the gamma ray (590 keV) by which the ^{25}Mg nucleus decays is also detected and summed to the α+Mg signal, since the mean lifetime for this level is 3,4 ns. This will produce an energy signal corresponding to the signal from the reaction $^{28}Si(n,\alpha_o)^{25}Mg$, or in the energy region between these reactions if the gamma ray Compton-scatters and then escapes from the detector. In the classic case of $^{28}Si(n,p_1)^{28}Al$ the low energy de-exciting γ-ray (E = 31 keV) is sufficiently low for the gamma ray to be stopped with high probability in the detector, causing peak p_1 to overlie p_o. For randomly positioned reactions in the case of the 1 000 μm deep detector, the mean path length to exit from the detector is ~ 6 mm. The attenuation for a 31 keV gamma ray in 6 mm silicon is 0,79 , which implies that 80% of these gammas would be absorbed in the detector, thereby enhancing the p_o peak at the expense of p_1.

Many of the particle producing neutron induced reactions occurring in a silicon detector result in unstable residual nuclei that β-decay to stable nuclei. The different nuclei are shown in Table 4.3 with their half lives, the energy of the transition and the decay mechanism. It has been shown[Mi67] that the maximum energy which an electron can deposit in a detector with maximum path length of 1 cm is about 6 MeV. This leads to a limitation in lower energy neutron measurements, but has no real effect on the resolution of high energy neutron detection (>10 MeV) except superficially through pile-up. However, pile-up effects did not pose problems since the count rate was low (0,1 kHz). This problem becomes worse when using deeper detectors.

Table 4.3
Residual nuclei contributing to background by β-decay

Reaction	$t_{\frac{1}{2}}$ (s)	Decay mechanism	Energy of decay (keV)
$^{30}Si(n,p)^{30}Al$	3,69	$^{30}Al(\beta)^{30}Si$	8540
$^{29}Si(n,p)^{29}Al$	393,6	$^{29}Al(\beta)^{29}Si$	3681
$^{28}Si(n,p)^{28}Al$	134,6	$^{28}Al(\beta)^{28}Si$	4643
$^{30}Si(n,\alpha)^{27}Mg$	567,5	$^{27}Mg(\beta)^{27}Al$	2609

The energies of decay are such, however that the decays do not contribute to background in the higher end of the spectrum, where the region of interest really is. For the prominent reaction $^{28}Si(n,p)^{28}Al$ with a large negative Q-value of -3852,1 keV, the energy of the resulting peaks corresponding to the different states of the ^{28}Al nucleus will be such that the β-decay of ^{30}Al will contribute to the background only from the peak corresponding to the 5th excited state of ^{28}Al . The intensity of these transitions are also small due to the small contribution of ^{30}Si based reactions to energy spectra.

4.5.5 Electronics

The electronic circuit used to process energy signals and generate spectra was elementary. The different units used are detailed in Fig. 4.9.

Two such circuits were run simultaneously into Canberra 8080 ADC's and stored on-line on the Nova 3/4 computer.

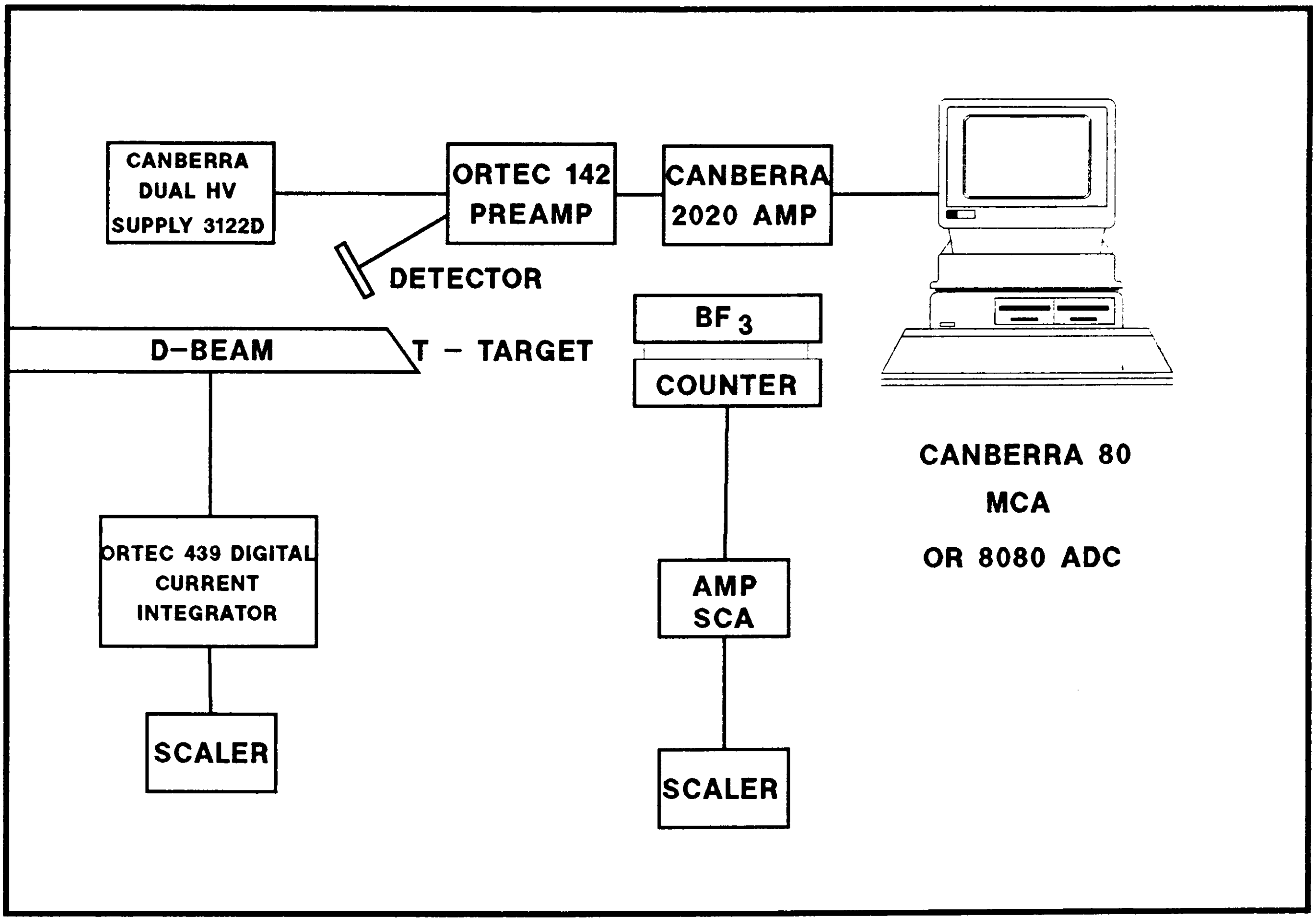

Fig. 4.9

Electronic signal processing

4.6 Experimental configuration

A deuteron beam was accelerated by the AEC Van de Graaff accelerator at Pelindaba to 1,5 MeV, deflected through 90° by an analysing magnet used for machine stabilisation and directed and focussed by alternating gradient magnetic quadrupoles onto a titanium tritide target. Typical beam current at the target was 1 to 2 μA. The three silicon detectors were located 12,5 cm from the target and situated at an angle of 110° with respect to the deuteron beam in the edge-on configuration. The experimental configuration is schematically detailed in Fig. 4.10.

4.7 Spectra obtained

The spectra produced by the silicon solid state detectors, of 1000 μm, 300 μm and 100 μm depth respectively, are shown in Figures 4.11, 4.12 and 4.13. These spectra are characterised by several clearly defined peaks resulting from the reactions with the naturally abundant isotopes of silicon. The energy level diagrams for the residual nuclei are included in the spectra for easy correlation and identification. The spectra clearly indicate the many states in each residual nucleus.

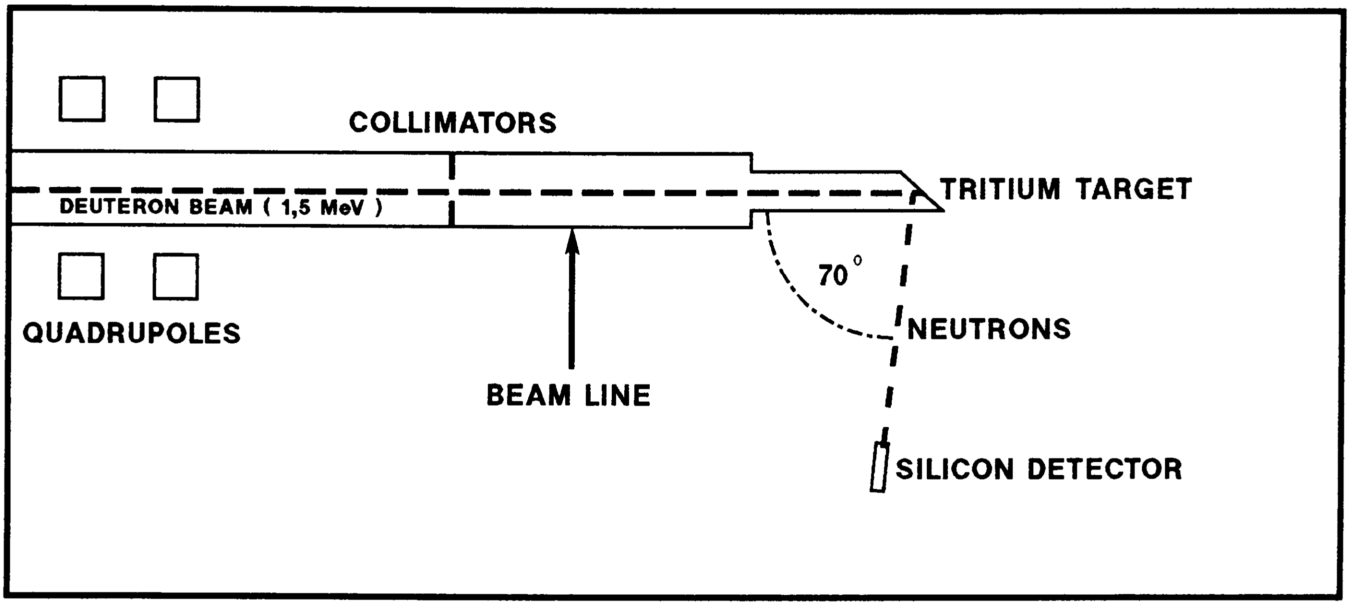

Fig. 4.10

Experimental configuration

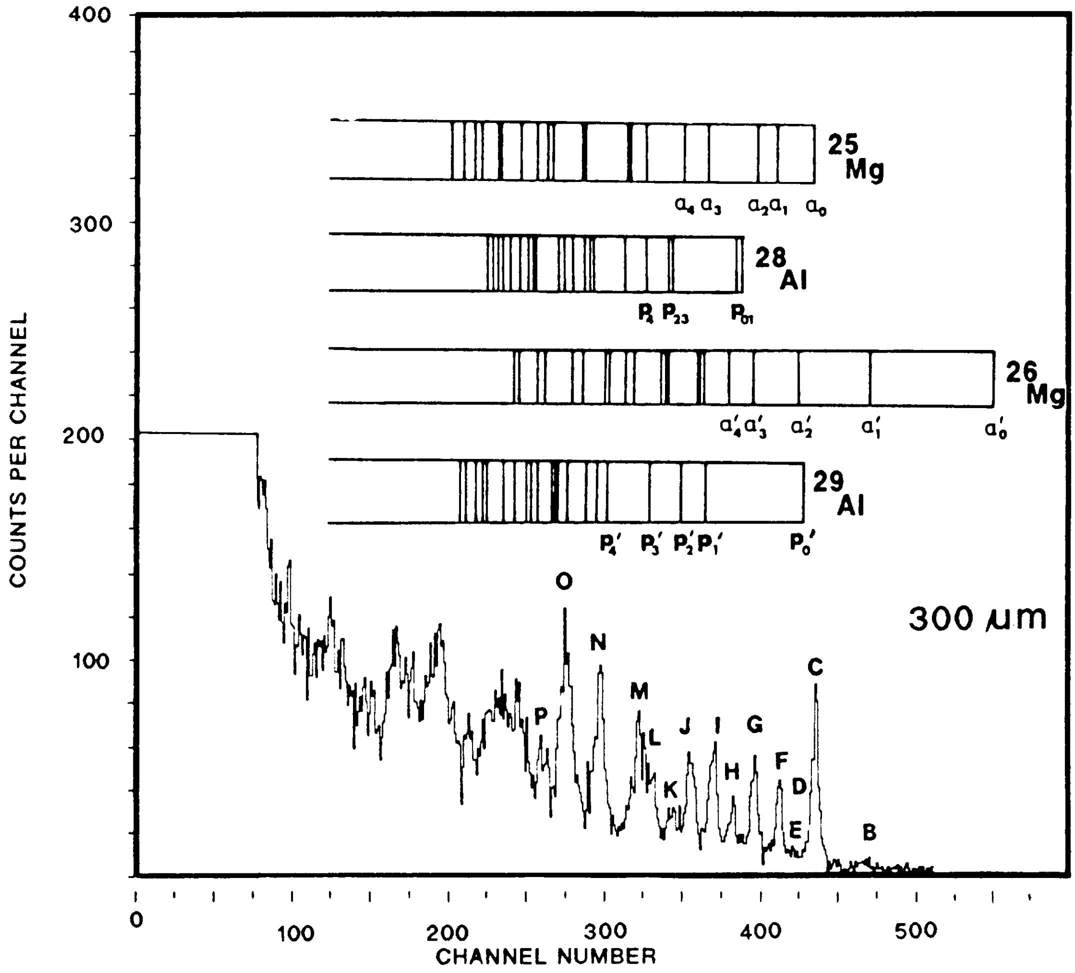

Fig. 4.12

Energy spectrum obtained with 300 µm deep detector

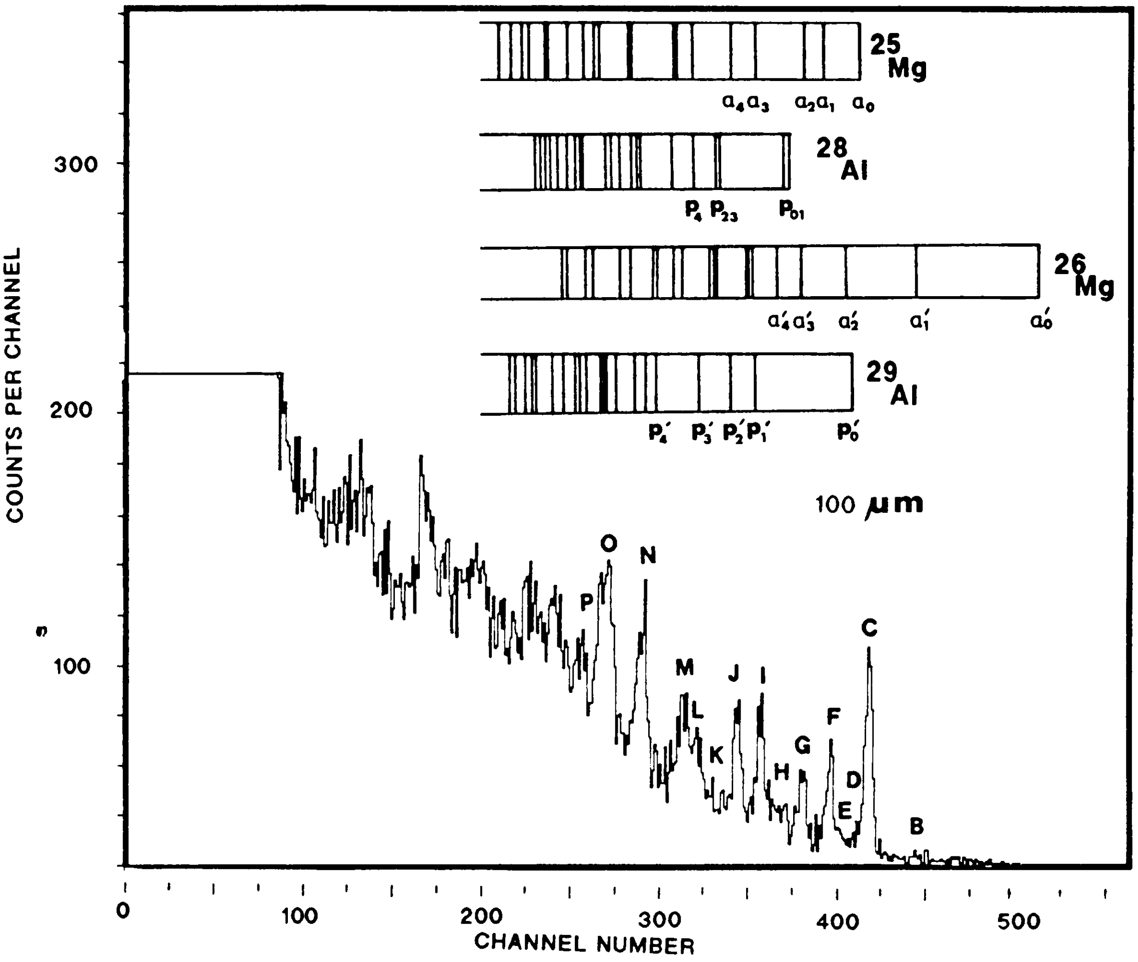

Fig. 4.13

Energy spectrum obtained with 100 μm deep detector

The peaks in all these spectra having the same origin have the same alphabetical letters associated with them, and these states are identified with peaks as indicated in Table 4.4.

Table 4.4

Reaction contribution of different states of nuclei to peaks identified in spectra

Peak	Primary contribution	Secondary contribution
A	α_0'	-
B	α_1'	-
C	α_0	-
D	α_2'	-
E	p_0'	-
F	α_1	-
G	α_2	α_3'
H	p_0^+, p_1	α_4'
I	α_3	p_1' , α_5' , α_6'
J	α_4	-
K	p_2	p_3, α_7' , α_8' , α_9' , p_2'
L	α_5	-
M	α_6, α_7, p_4	α_{10}' , α_{11}' , p_3'
N	α_8, α_9, p_6, p_7, p_8	α_{14}' , α_{15}' , p_4' , p_5' , p_6'
O	α_{10}, α_{11}, α_{12}	α_{16}' , α_{17}' , p_8' , p_9' , p_{10}'
P	α_{12}, α_{14}	p_{11}' , p_{12}' , p_{13}'

Peaks C and F indicate the ground state and first excited states of ^{25}Mg. The main contribution to peak G is the second excited state of ^{25}Mg, as is the third excited state in peak I. Peak H is attributed both to the ground state of ^{28}Al [^{28}Si(n,p$_o$)^{28}Al] and the first excited state [^{28}Si(n,p$_1$)^{28}Al], as discussed in Section 4.5.4. Due to the bigger volume of the 1 000 μm detector more of the de-excitation gamma rays (31 keV) are absorbed in the detector when compared with the 300 μm detector. As such, the p_{o1} peak (H) in the 300 μm spectrum should be broadened on the lower energy side by comparison with peak H in the 1 000 μm spectrum. This is indeed seen when comparing Figures 4.11 and 4.12. This characteristic would be even more enhanced for the 100 μm detector. However, since most protons escape from this detector undetected there is no clearly visible peak H in Fig 4.13. The lower lying peaks from the different states of ^{28}Al have several interferences among themselves. An important shift of about 100 keV between the expected and measured α_o-α_4 peak positions (C, F, G, I, J) relative to the neighbouring p_{o1} and p_{23} (H, K) peaks is seen as was measured earlier[Mi67,Mi71], the p_i peaks being relatively low with respect to the α_i peaks.

The peak K consists mainly of the second and third excited states of ^{28}Al, and has to be energy defined in terms of the mean energy. These states are separated by 40 keV and with the energy resolution of 200 keV, there is no way of distinguishing between p_2 and p_3. The position of this peak was calculated from the average expected position assuming equal population of these states which again indicated the shift to lower energies of the calculated peak by 100 keV with respect to the α-peaks.

Since the previous measurement[Mi71] the fifth excited state of ^{28}Al has been shown to be a doublet[En78] at 1,620 and 1,623 MeV.

The 4,7 % component of ^{29}Si makes it possible to identify peaks resulting from the ground state (α_o') and first excited state (α_1') of ^{26}Mg because of the low negative reaction Q-values. Although peaks A and B are small, they are identifiable. The (n,p_i') reactions overlie the peaks from reactions of ^{28}Si and the ground state is not seen, since it is overridden by the strong ^{28}Si$(n,\alpha_o)^{25}$Mg peak. Positions of peaks D and E are indicated although they are not identifiable in these spectra.

The higher order (lower energy) peaks are subject to greater interference and are impossible to resolve. The expected associations between levels and peaks are shown up to peak P. No such levels are shown for ^{30}Si based reactions since the Q-value leaves peaks heavily overridden by the major ^{28}Si component reactions.

Due to the relative shift of the p_i peaks relative to the α_i peaks because of the pulse height defect of heavy recoil ions, it was decided worthwhile to attempt to calibrate the energy absolutely with α-sources. This is difficult due to the high energy region that needed to be covered, and was done with exactly the same electronic configuration but with the 300 μm deep detector which displayed the best resolution in an evacuated chamber. The α-sources used were ^{241}Am (5,488 and 5,443 MeV) and ^{230}Th (4,688 and 4,621 MeV). This calibration showed the peaks resulting from (n,α_i) reactions to be shifted 120 ± 16 keV lower than expected in energy, with the peaks from (n,p_i) reactions shifted by a further 100 keV. The absolute calibration was made including corrections for alpha particle energy loss in the entrance window of ~20 keV. From the measurement of Bizetti et al[Bi65] it had been derived previously that signals from different recoiling heavy ions (^{27}Al, ^{24}Mg in his case) led to different pulse height defects in the measurement of energy. This complements the measurements[Mi67,Mi71] which have indicated the relative shift of the α_i-groups with respect to the p_i-groups as related to this phenomenon. It is therefore essential that this pulse height defect be taken into account whenever high energy reactions involving detection of heavy ions by solid state detectors are studied.

4.8 The pulse height defect (PHD)

Since the first measurements were made, the importance of the PHD has increased considerably with the advent and advance of high energy heavy ion accelerators and associated studies. The intense study of fission fragments in other studies necessitated precision energy measurements and calibration of heavy ion spectroscopy. Therefore a need for the accurate absolute calibration of the mass dependent energy non-linearity of solid state detectors developed. Application of the results of more recent measurements[Ka74, Fi84] of the PHD to these measurement is limited. These studies were almost exclusively done for particles of greater mass (A = 59 to 238[Fi85]) and higher energies (up to 100 MeV)[Mo78].

The pulse height defect is the difference between the true energy of an ion and the energy of a light charged particle (p or alpha), measured with the same pulse height as the ion, which is the apparent energy of the ion [Wi71]. The original theoretical treatment was done by Lindhart et al[Li63] relating to energy loss mechanisms of ions in matter where it was recognised that the kinetic energy of the heavy recoil nucleus was not fully spent in electron-hole pair signal producing processes, which led to the collection of free charge carriers generating the output pulse.

Other processes such as lattice vibrations, heat dissipation and nuclear interactions also contribute to the loss of energy of heavy nuclei. This leads to the fact that not all the kinetic energy is detected electronically, and the pulse height corresponding to the signal is measured at lower energies than expected.

The peak energy detected for a given reaction is defined by the Q-value, the incident energy, and the full collection of electron-hole pairs produced by both reaction products. For example, in the $^{28}Si(n,\alpha)^{25}Mg$ reaction both the alpha particle and heavy residual nucleus ^{25}Mg deposit their energy in the detector. If emission is isotropic then the energies for the alpha particles range from 10,808 MeV (θ_{lab} = 0°) to 7,703 MeV (θ_{lab} = 180°), corresponding to ^{25}Mg energies from 0,328 MeV (θ_{lab} = 180°) to 3,433 MeV (θ_{lab} = 0°). (Emission might not be isotropic though, but might have a small component of excess forward yield, corresponding to a direct reaction component in contrast to a full compound nucleus mechanism. These effects should, however, be small[Mi67].)

Although the pulse height detection of the alpha particle in this reaction is accurate, that is not the case for the heavy emergent nucleus. This is seen in the spectral results discussed, namely the shift in energy of full energy peaks, which not only adds to degradation of energy resolution but makes absolute calibrations difficult. This shift is dependent on the angular distributions and kinematics of the reaction under study.

There are two theories[Mi67] that attempt to explain the effect: (1) that recombination of electron-hole pairs in the first part of the track leads to charge loss and (2) that the PHD results from screened collisions closer to the end of the track when free charge carrier production losses occur - this being the theory of Lindhart.

Experiments have been done by several groups[Ai62, Ax65, Sa65, Bi65, Mo66] trying to discriminate between the contributions of both theories. Axtmann and Kedem[Ax65] measured the PHD for fission fragments and found it to be approximately constant for both heavy (PHD ~13 MeV) and light (PHD ~11 MeV) fragments over the energy range 25-100 MeV. They concluded therefore that the PHD is generated towards the end of the track of the fragment in the detector, as the PHD was independent of incoming energy and mass. This indicated that heavy ions being slowed down would lose energy initially by ionisation and partly by nuclear stopping near the track end knowing that the probability of nuclear collisions increased as the velocity of the ion decreased.

These results were complemented by Morgenstern et al[Mo66] where neutrons were produced via the reaction $T(d,n)^4He$ (E_d = 300 keV), and used to bombard two silicon detectors in vacuum facing each other. Coincident pulses from (n,α) and(n,p) reactions were registered resulting from particle production and losses in either detector. By varying the angle subtended by the detectors, an angular distribution was obtained while flight time measurements were used to discriminate against different particles. The results indicated that the PHD was entirely due to the heavy ions (^{25}Mg and ^{28}Al in this case) and not at all due to the light particles. The ionisation fraction as a function of ^{28}Al recoil energy as derived from the original theory[Li63] is shown in Fig. 4.14 together with values measured[Mo66]. From this relation the ionisation fraction for ^{28}Al recoil nuclei for the maximum recoil energy of 1,56 MeV is 0,87. This leads to the result that the absolute pulse height defect for ^{28}Al (E_n = 13,738 MeV) is 200 keV, which is in fair agreement when compared with the value obtained (220 ± 16 keV) from the absolute energy calibration in these measurements.

Results have also led to the suggestion[Bi65] that the PHD results from incomplete charge collection in the detector due to charge carrier trapping and recombination in the dense plasma created by the heavy ion. The carriers may be screened from the electric field by the surrounding plasma field and recombine before the plasma is diffused. These results led to other studies[He78] of the rise time of the signals from silicon detectors to measure plasma times.

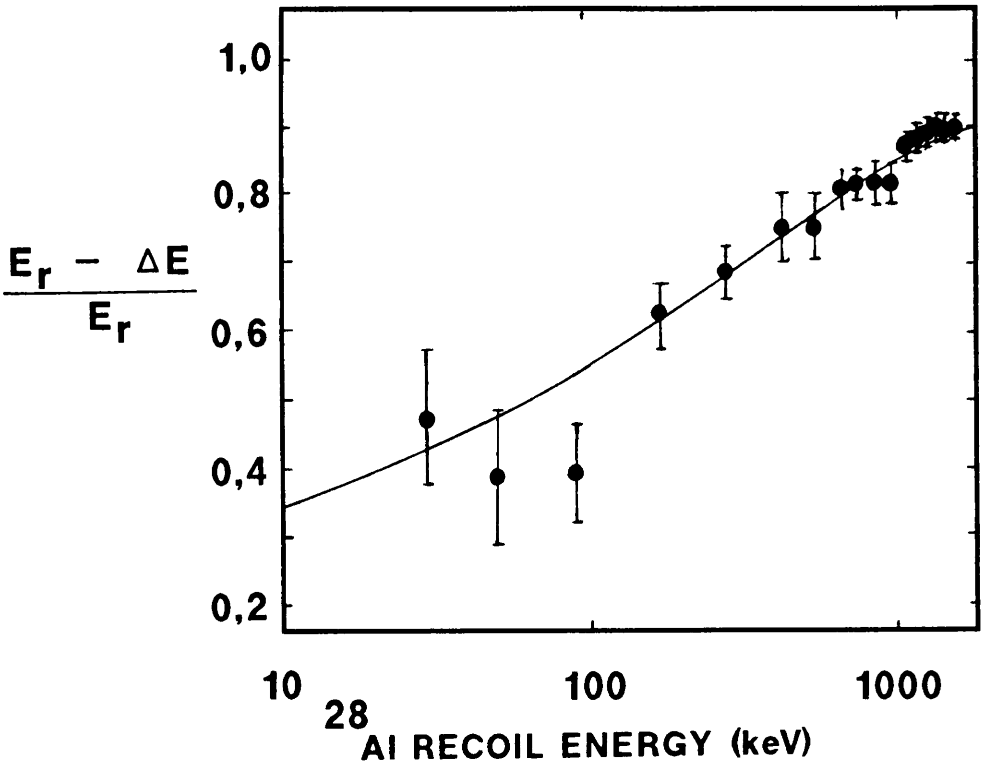

Fig. 4.14

Ionisation fraction as a function of ^{28}Al energy

4.9 Edge effects in detectors

When inspecting the spectra obtained (Figures 4.11 to 4.13) the obvious feature is the difference in peak height of peaks corresponding to alpha particle emission with respect to peaks corresponding to proton emission when using detectors of different active depths. As expected, the proton related peaks become relatively smaller for thinner detectors as the relative number of protons escaping from the active volume of a detector increases as the thickness decreases.

The study of edge related effects was undertaken to estimate the contribution of particles lost from the active volume of these detectors. The area under the peaks α_o and p_{o1}, were determined, and the ratios of counts in the α_o-peak relative to the counts in the p_{o1}-peak (N_{α_0}/P_{01}) were calculated with results of 2:8:40 for 1000 µm:300 µm:100 µm detectors respectively. These values were compared with theoretically expected values which were obtained by simple geometrical considerations.

When a point source of particles (alphas or protons) inside the active volume of a detector is considered, which radiate particles of equal energy (thus equal range assumed) isotropically, it is possible to obtain the expected efficiency of a detector of specific dimensions for containing particles. The average energies of both the alphas and protons associated with the reactions leading to the ground state of ^{25}Mg and the ground state of ^{28}Al were assumed to be 10 MeV, with ranges of 70 µm and 700 µm in silicon [An77] respectively.

By using simple integration routines it was possible to obtain the contributions of different parts of the edges, that is the face and side of the detector, to the loss of particles from the active volumes of the detectors. These results are summarised in Table 4.5.

Table 4.5

Expected percentages of particles lost from the active volumes of different detectors with separate contributions from the face and side indicated

Particle	Detector (depth (μm); and area (mm²))								
	1000;450			300;300			100;450		
	Side	Face	Total	Side	Face	Total	Side	Face	Total
α	0,9	4,5	5,4	1,0	14,9	15,9	0,8	44,6	45,4
p	7,7	44,6	52,3	6,4	86,3	92,7	4,9	95,0	99,9

These results are plotted both for alphas and protons in Figure 4.15.

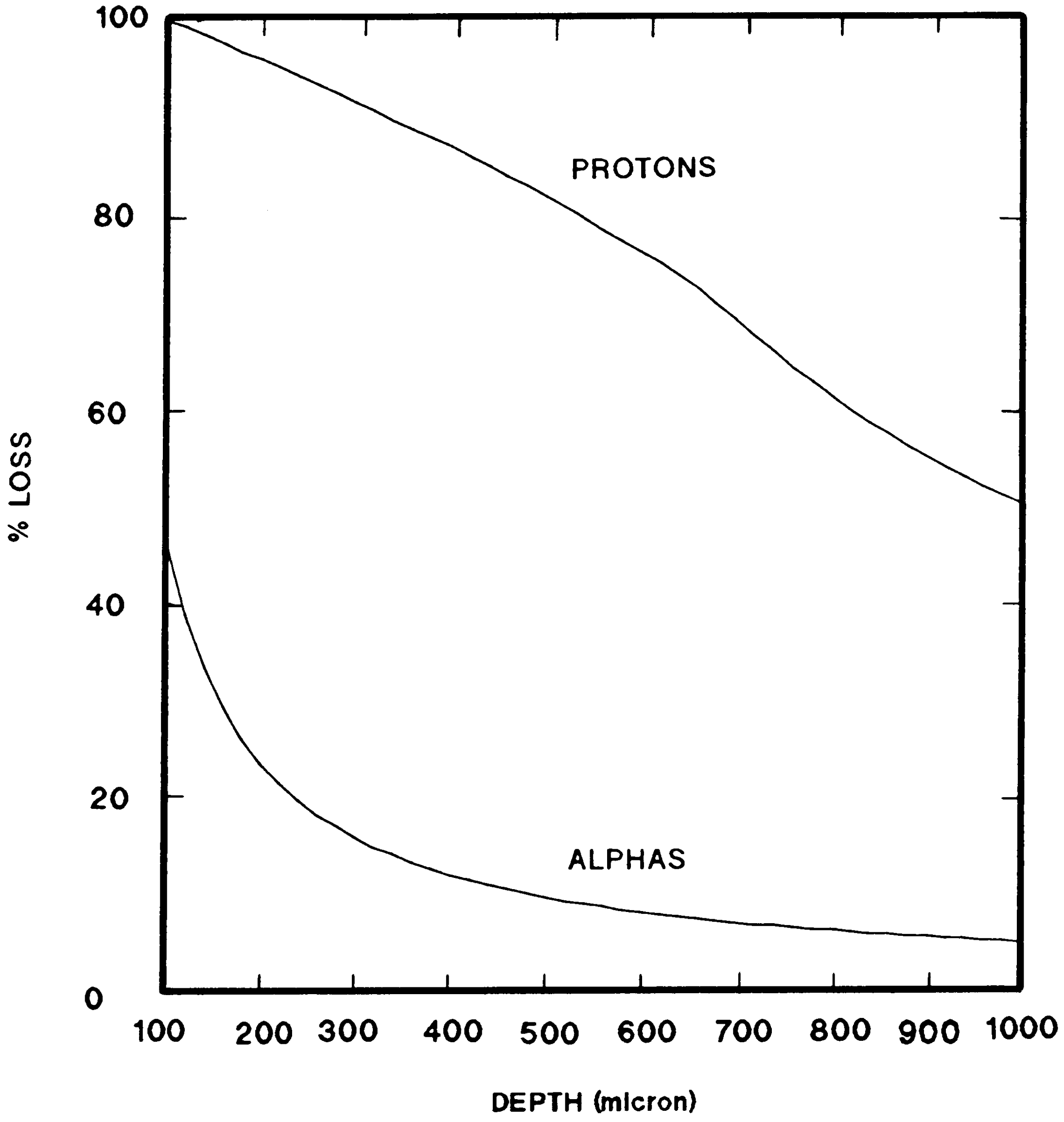

Fig 4.15

Expected percentage losses from detectors with different depths for 10 MeV protons and alpha particles

From these values it is possible to determine the expected $\frac{N_{\alpha 0}}{N_{p01}}$ as a function of detector depth and this result is plotted in Figure 4.16 together with the experimentally obtained values for the different detectors used.

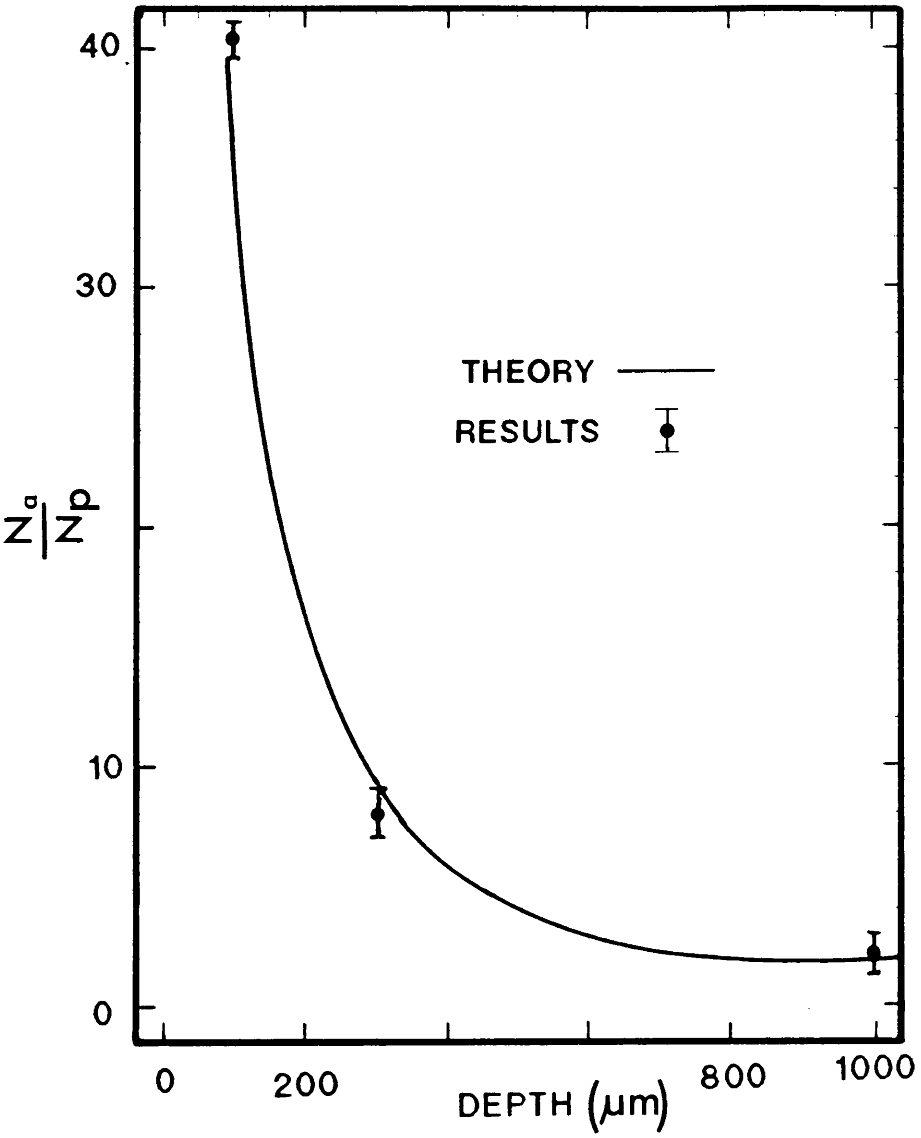

Fig. 4.16

$\frac{N_{\alpha_0}}{N_{p_{01}}}$ as a function of detector depth

The error bars include the choice of average particle energy, as well as statistical errors. The excellent correspondence of predicted values with the experimental results suggests that the assumptions made in the calculations are valid, and that it is realistic to accept the values in Table 4.5 for absolute losses from the detectors. These results allow easy, efficient calibration of detectors with different depths.

4.10 Feasibility of using a thinner detector for standard flux measurements

The cost of deep detectors (1 000 µm) being an order of magnitude more expensive than 100 µm detector suggested the study of the feasibility of using a 100 µm detector instead of the 1 000 µm detector normally used.

From geometrical considerations to achieve the same counting efficiency for 1 000 µm and 100 µm detectors with equal areas, the 100 µm detector must be placed closer to the neutron source by a factor of √10. In monitoring $T(d,n)^4He$ reactions, if the spread in angle is determined for both these detectors in such equal solid angle positions, it follows that the spread in angle, and resulting spread in neutron energy is smaller for the 100 µm detector. This result is shown in Figure 4.17 where the neutron energy spreads for the 100 µm and 1 000 µm detectors were calculated for equal solid angles of detection and a point neutron source.

In subsequent measurements it was clear that care should be taken when making measurements with the 100 µm detector. Figure 4.18 was obtained using the 100 µm detector in the side looking configuration, but placed very close to the neutron source.

This led to serious degradation of resolution due to both finite beam spot size and the importance in exact alignment of the detector. This is apparent when using the 1 000 µm, 300 µm and 100 µm detectors in the face on position, again for equal detection efficiency, recognising that the deeper detectors are positioned further away from the source. The resulting spectra showing kinematic effects in loss of neutron energy definition especially in the case of the closely positioned 100 µm detector are shown in Figures 4.19, 4.20 and 4.21.

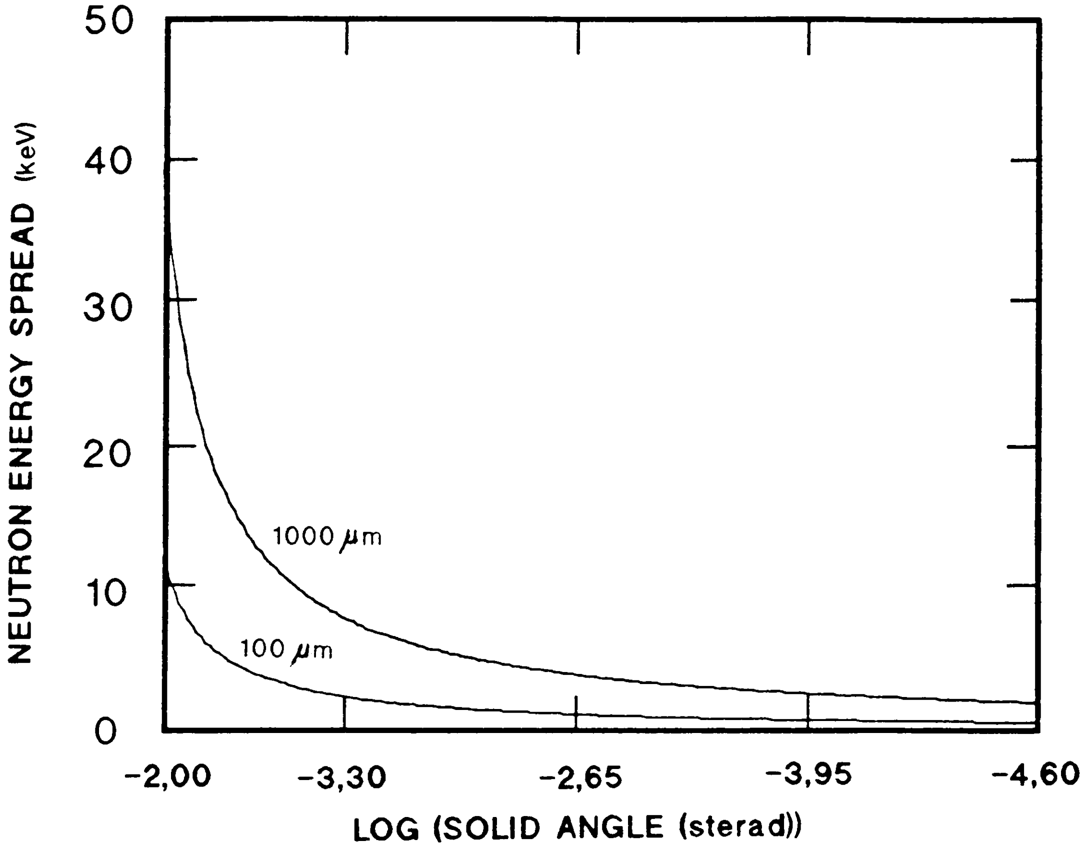

Fig. 4.17

Spread in neutron energy as a function of solid angle from the source for the 1 000 μm and 100 μm detectors

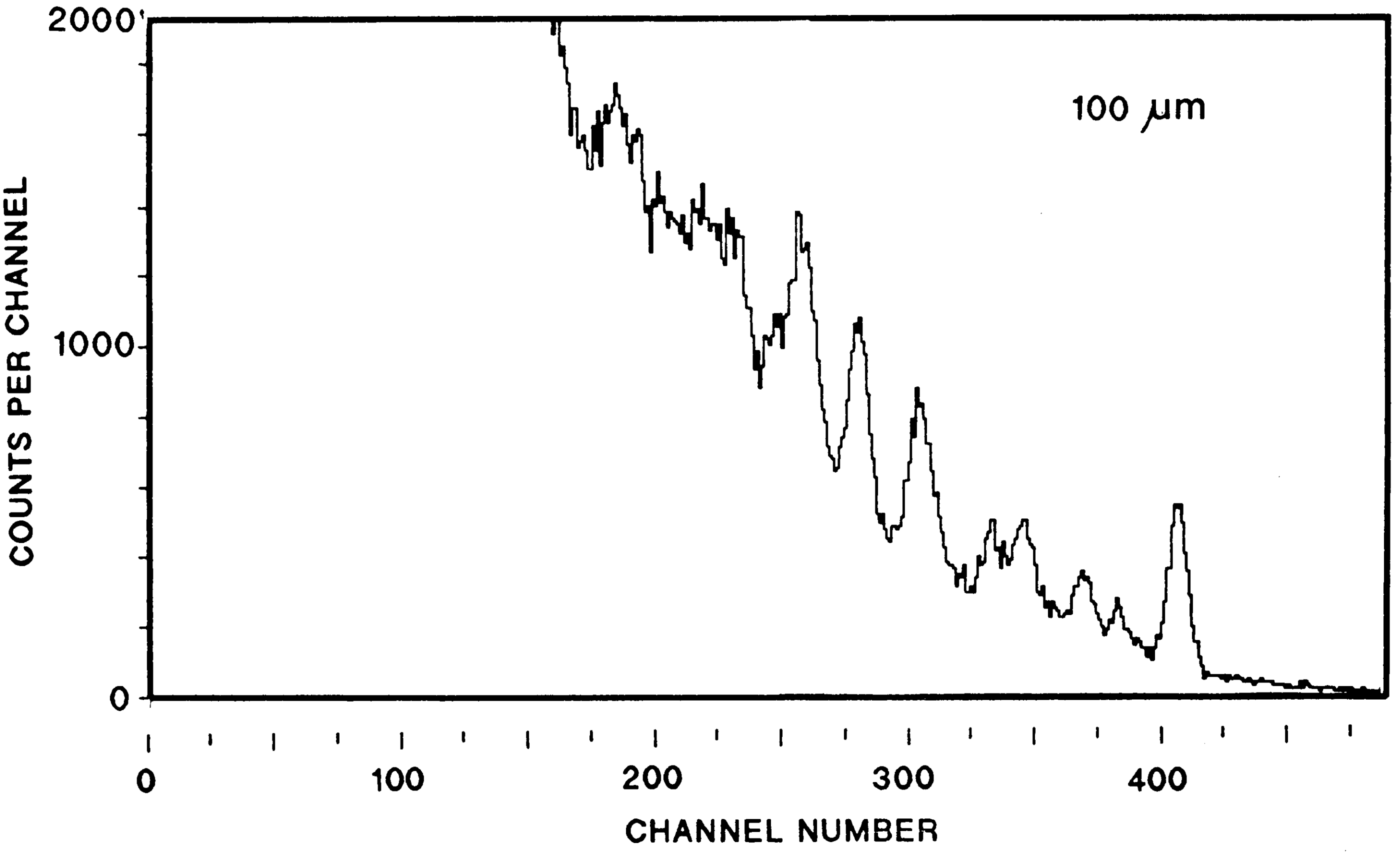

Fig. 4.18

Spectrum obtained with 100 μm detector very close to neutron source

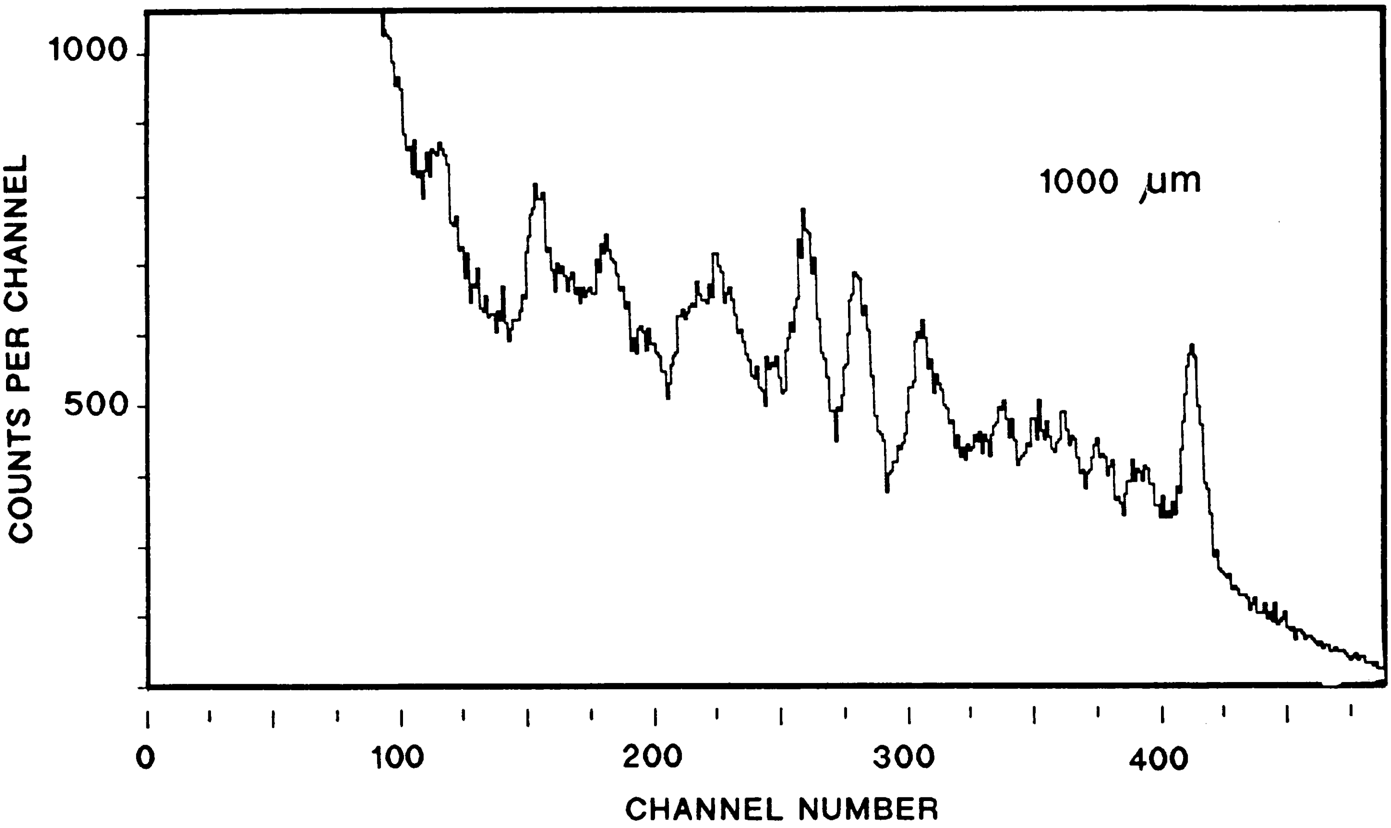

<u>Fig. 4.19</u>

<u>Energy spectrum of 1 000 µm detector in face on position</u>

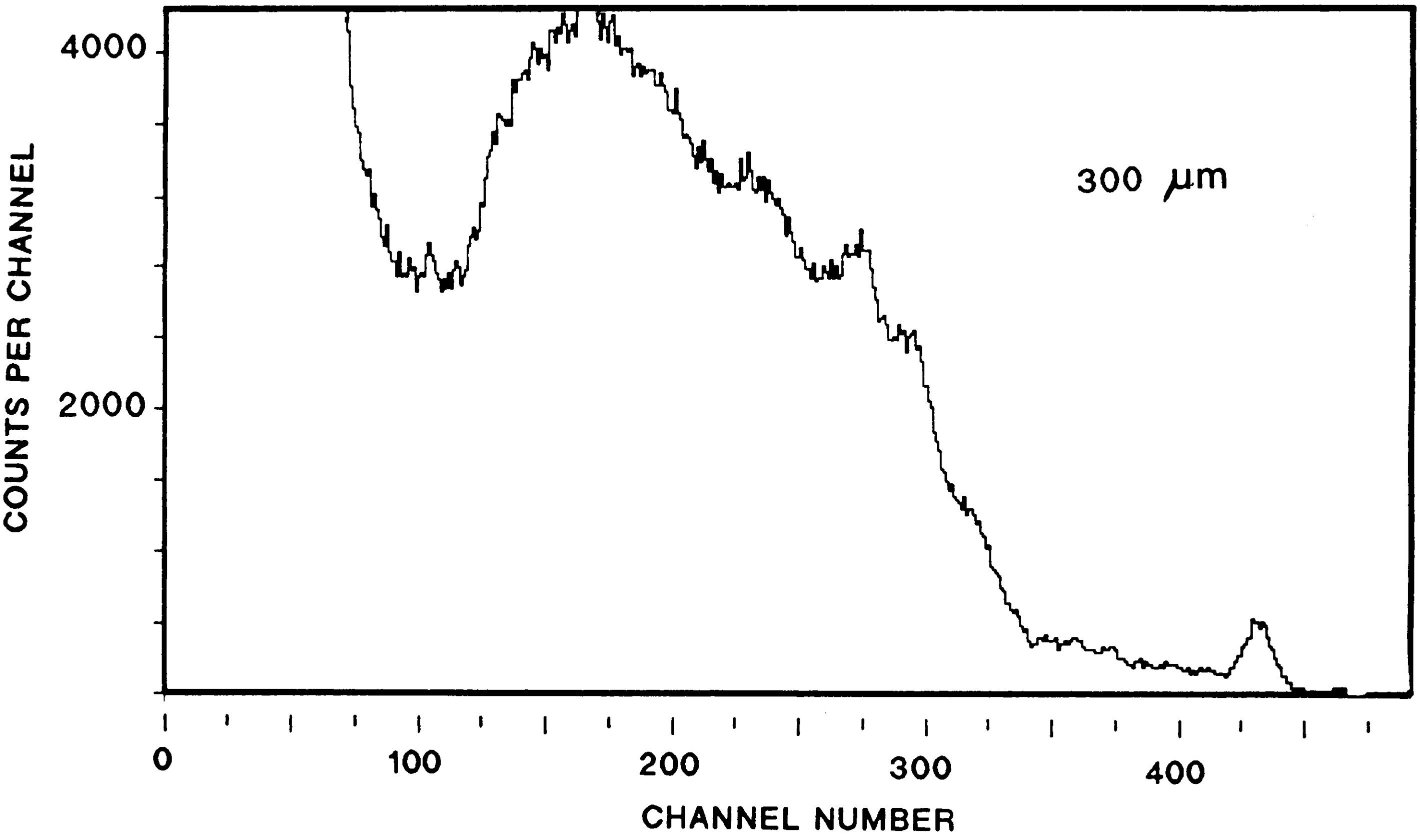

<u>Fig. 4.20</u>

<u>Energy spectrum of 300 µm detector in face on position</u>

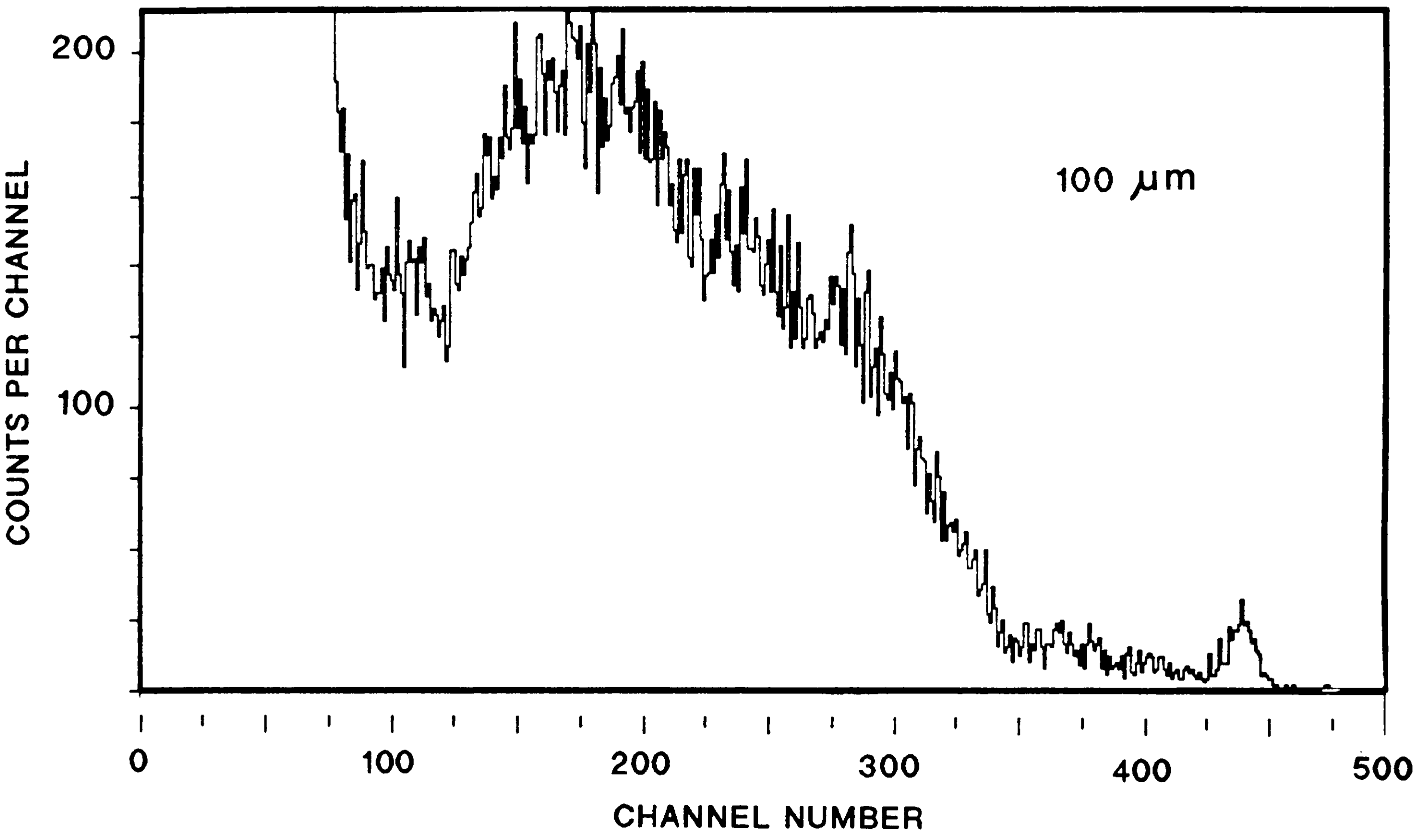

Fig. 4.21

Energy spectrum of 100 µm detector in face on position

It is obvious that the geometry and kinematics of the source of neutrons become very important for such a detector. The use of such a detector for example as a neutron spectrometer in a fusion device would be impractical due to the large range of neutron energies encountered at all angles. However, it would be possible to derive some values for neutron fluxes at high energies (>10 MeV).

4.11 Conclusion

The use of silicon solid state detectors for neutron energy measurements has been firmly established since the 1960's. It has proved useful at the Van de Graaff accelerator at Pelindaba, AEC, where various detectors have been used to obtain neutron flux measurements for application to specific projects.

There are a number of complicating phenomena, of which the pulse height defect and finite volume loss effects are the most important, which have to be considered during measurements, but these do not affect the technique severely. A thinner detector can also be used as a cheap alternative to the deeper detectors normally used.

This technique has now been established as a standard method of 14 MeV neutron energy flux measurements at the accelerator at Pelindaba.

5 STUDY OF PHYSICAL PROPERTIES OF X-RAY DETECTORS

5.1 Introduction

The efficiency and physical properties of X-ray detectors have been extensively studied in the past (eg [Sh79], [Ba84], [Ca84]) and have reached a state of maturity portrayed by a state of the art review recently published by Campbell et al [Ca86]. The fundamental complexity of complete definition of detector efficiency is obvious from this compilation of techniques and standards.

X-ray detectors are used at Pelindaba in various atomic physics endeavours and maximum knowledge of these detector characteristics is vital in order to obtain reliable results from experimental measurements. It was impossible to fully investigate and describe our X-ray detectors since e.g. in situ direct determination of beryllium window thickness has not proved possible as yet. However, it was vitally important to study the geometry and efficiency of these detectors since parameters such as distance from detector window to crystal face, geometrical size and shape, intrinsic efficiency and charge collection factors of the detector crystal are important factors of the detection characteristics. The efficiency response of an X-ray detector is determined by absorption effects, as defined by a number of entrance windows, the intrinsic ingot efficiency and geometry related functions. It has been previously shown [Ca84], [Il84] that should geometrical parameters of X-ray detectors require to be applied in measurements they should be confirmed experimentally, since one cannot rely on manufacturer specifications.

5.2 Experimental

5.2.1 Efficiency of X-ray detectors

The efficiency of an X-ray detector is defined by

$$\varepsilon(E) = \varepsilon_I f_g f_{Be} f_{Au} f_d f_R \left(E \right) \qquad (5.1)$$

where $\epsilon_I(E)$ = intrinsic efficiency

$f_g(E)$ = photon energy dependent geometric function

$f_{Be}(E)$, $f_{Au}(E)$, $f_d(E)$ = transmission factors through beryllium window, gold and frontal dead layers

$f_R(E)$ = radial dependent efficiency

To obtain the efficiency of an X-ray detector all these contributions should be determined.

The intrinsic efficiency is related to the stopping power of detectors as well as the role of escape peaks. For germanium detectors the stopping power is sufficiently high to be considered capable of fully stopping 50 keV photons while silicon detectors have a roll off of efficiency from typically 10 to 20 keV.

The function $f_g(E)$ is important only for a high energy source, typically >50 keV, very close to the detector. As this was not the case in any of these measurements, it was not taken into account.

In general the product absorption correction $f_{Be}.f_{Au}.f_d$ is measured by calibration without singling out the respective components. While this was the case in our calibration routine it is worth mentioning the techniques that can be applied for individual determinations.

Although a lot of thought [Ca86] has been devoted to measuring the thickness of the beryllium window in situ it has not yet proved to be possible without damaging the detector. During these measurements different methods were considered to directly obtain this thickness, but no technique could be found where the detector would not be damaged during such a measurement. This correction however poses a problem with low energy photons (<3keV) only, and consequently the nominal thickness provided by the manufacturer was used. The transmission of photons through beryllium is given by

$$f_{Be}(E) = \exp(-\mu_{Be}(E) d_{Be}) \quad (d_{Be} = \text{window thickness}) \tag{5.3}$$

where $\mu_{Be}(E)$ is the energy dependent linear attenuation coefficient of photons in beryllium.

For E_X = 6 keV this means that a 10 μm beryllium window has less than a 1 % effect on the X-ray transmission compared with a 1 % absorption for a 30 μm beryllium window. When looking at the efficiency at lower energies however, this becomes important. At 3 keV the contributions from these windows are 3 % and 9 % respectively.

The absorption of the frontal gold contact can be determined by fluorescence of gold X-rays with photons of energy larger than 11,92 keV (i.e. above the Au L_3 edge). From the number of Au X-rays measured and knowing the source strength, the thickness of the gold contact can be derived and the transmission of photons calculated. The thickness d_{Au} is typically <0,03 μm, which value results in <2 % absorption of 6 keV photons with increasing effect at lower energies.

The dead layer transmission factor f_d can be obtained concurrently with that of the gold contact determination by fluorescence of K

X-rays of the detector in the dead layer region. The number of characteristic germanium (or silicon) X-rays measured is therefore an indication of the dead layer thickness d_d, which is given by the relation [Ha73].

$$d_d = \frac{2C_K \varepsilon_\gamma}{C_\gamma \varepsilon_K \mu_K w_K} \qquad (5.3)$$

where:

$\frac{C_K}{C_\gamma}$ is the observed ratio of Ge (or Si) K X-ray yield to the number of counts in the exciting photon peak.

μ_K is the mean K-shell attenuation coefficient in the detector for the exciting photons.

$\frac{\varepsilon_K}{\varepsilon_\gamma}$ is the ratio of intrinsic detection efficiencies for Ge (or Si) K X-rays and exciting photons.

W_K is the Ge (or Si) K-shell fluorescence yield.

The dead layer thickness for silicon detectors is typically ≤0,2 µm and for germanium detectors ≤0,5 µm. For 6 keV photons these values result in absorption correction of less than 1 % and 3 % respectively.

The radial dependent function $f_R(E)$ is included to correct for any radial dependence of efficiency. This effect is usually very small, and in these measurements the maximum difference in collimated efficiencies at different radial positions was always <<5 % for 6 keV photons with the exception of one IG detector (detector #3). This effect contributes at most a 1 % error to the efficiency of the good detectors.

At higher X-ray energies (>10 keV) the intrinsic efficiency of silicon detectors is defined by the sensitive depletion depth D of the detector since, at these energies, photons can penetrate the sensitive depth. The energy dependence of the efficiency of such a detector is given by

$$\varepsilon_I(E) = 1 - \exp(-\mu_{Si}(E)D) \qquad (5.4)$$

where $\mu_{Si}(E)$ is the absorption coefficient of photons in silicon.

The effect of typical maximum values used for physical properties of dead layers of a silicon detector on the low energy efficiency response is illustrated in Fig. 5.1(a) which illustrates the complexity of efficiency calibration required when entrance windows are relatively thick. The effect of L shell absorption by Au is particularly marked. In most detectors the Au layer is considerably thinner than shown here.

Fig.5.1(b) compares the efficiencies of IG and Si(Li) detectors through the energy regions 0,1 to 1 000 keV. The low energy region response is defined for different Be entrance window thicknesses. The high energy response is defined by the sensitive depth of the detectors, the higher stopping power of germanium showing up clearly in terms of greater efficiency of detection at high energies. The efficiency of a Ge detector drops abruptly to ~ 85% immediately above the K-edge of Ge at 11.1 keV where escape peak effects play a role. This recovers to essentially 100% efficiency within a few keV of this edge.

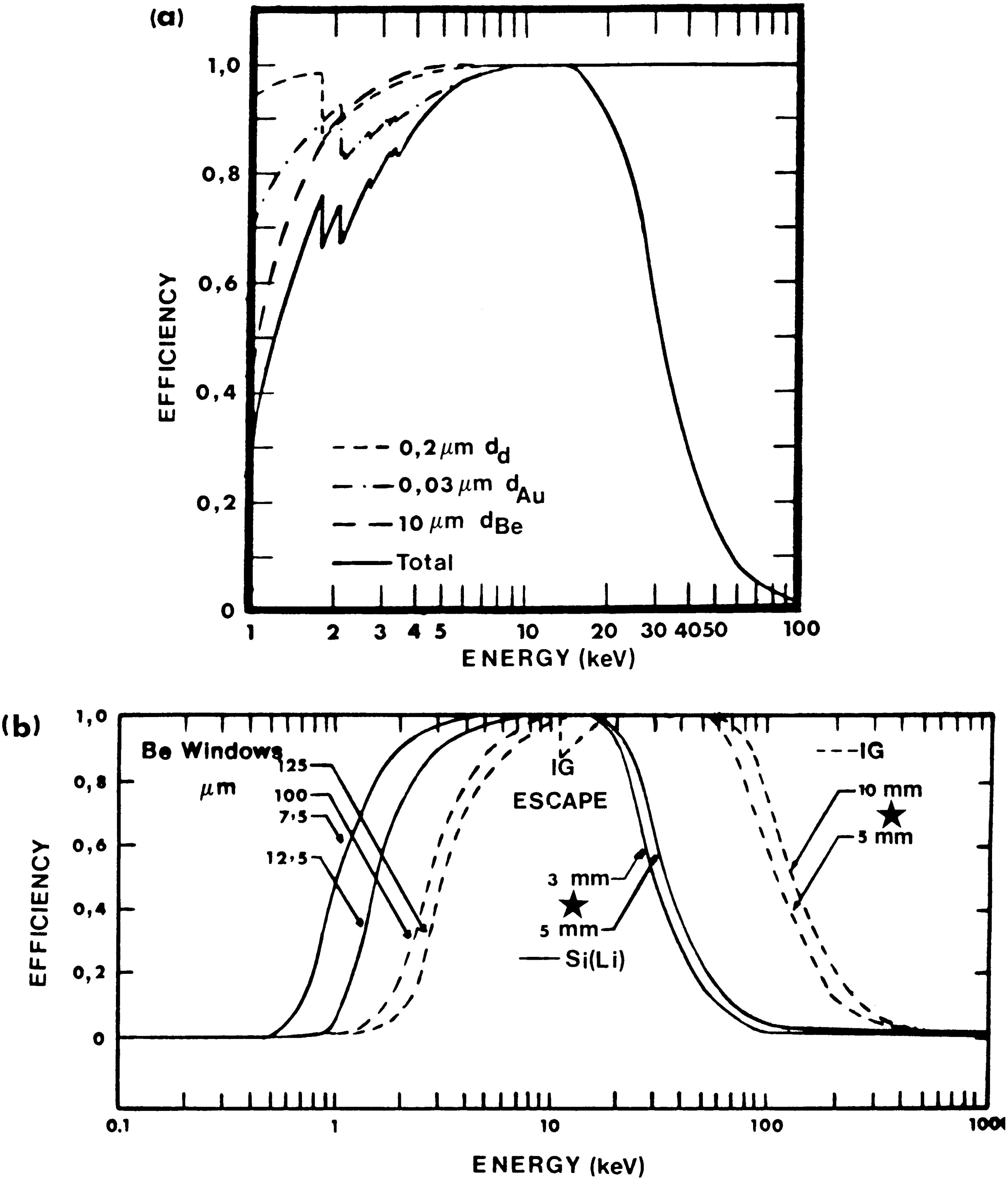

Fig. 5.1

Different contributions of physical properties to the efficiencies of silicon and germanium X-ray detectors

★ The drop in efficiencies at higher energies are determined by the sensitive depths of these detectors as indicated.

5.2.2 Geometry of detector crystal

Primary measurements concentrated on geometrical dimensions related to the exact size, shape and positioning of the sensitive volumes of the detectors with respect to their end cans.

The distance from the entrance window to the detector crystal was determined using an X-ray source and measuring the yield at different distances from the detector face and applying the inverse square law. In this case the relative yield of a specific peak, the 5,898 keV K_α peak from an ^{55}Fe X-ray source, was determined as a function of the distance between source and detector window (l). If the distance from the window to crystal is l_o then the yield N is given by

$$N = \frac{K}{(l + l_0)^2} \exp(-\mu_{air} l) = \frac{f(l)}{(l + l_0)^2} \qquad (5.5)$$

where N = number of counts under the K peak

K = constant of normalisation

μ_{air} = the linear absorption coefficient of a 5,898 keV photon in air (= 0,0253 mm^{-1}, corrected for 2 000 m altitude)

The correction applied for the X-ray absorption in air is essential and, if ignored, is sufficient to yield negative distances for l_o.

From (5.5) it is seen that if l is plotted versus $(f(l)/N)^{\frac{1}{2}}$ for different values of l, then the intersection of the straight line with the z-axis represents the distance l_o. The effective detection depth is obviously within the detector volume at a distance below the physical front surface of the detector given by the mean interaction depth Z(E) of photons of energy E which is [Ha73]

$$Z(E) = \frac{1 - \exp(-\mu_{Si}(E)D)(1 + \mu_{Si}(E)D)}{(1 - \exp(-\mu_{Si}(E)D)} \qquad (5.6)$$

for silicon (the equivalent mean interaction depth for germanium would be smaller). D is the sensitive thickness of the detector. This leads to a value in silicon of 0,03 mm for 6 keV photons, which represents a negligible depth correction.

The geometrical shape of the crystal was obtained using the same source, but collimated, to determine the response of the detector as a function of position on the detector face. The relative spatial response was measured by scanning this pencil beam of photons across the face of the detector. This measurement is similar to the measurement made with gamma rays described in Section 2.5, with the simplification that, in this measurement with low energy photons, there is virtually no transmission through the edges of thin tantallum metal collimators used to define source geometry. The experimental configuration used is shown in Fig. 5.2.

The diameter of the beam spot D_{max} is defined by

$$D_{max} = (D_d + D_s)(1 + \frac{v}{u}) - D_s \qquad (5.7)$$

where the different variables are indicated in Figure 5.2.

The need for such measurements to be performed on all new detectors purchased resulted in the design and fabrication of a task specific instrument which is shown in Figure 5.3.

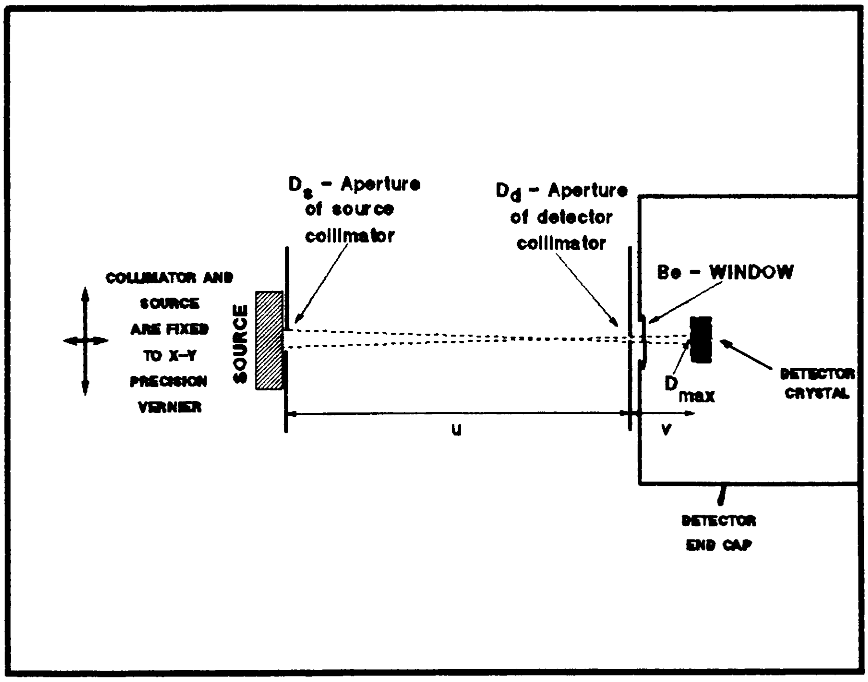

Fig. 5.2

Experimental configuration used for scanning of X-ray detector faces

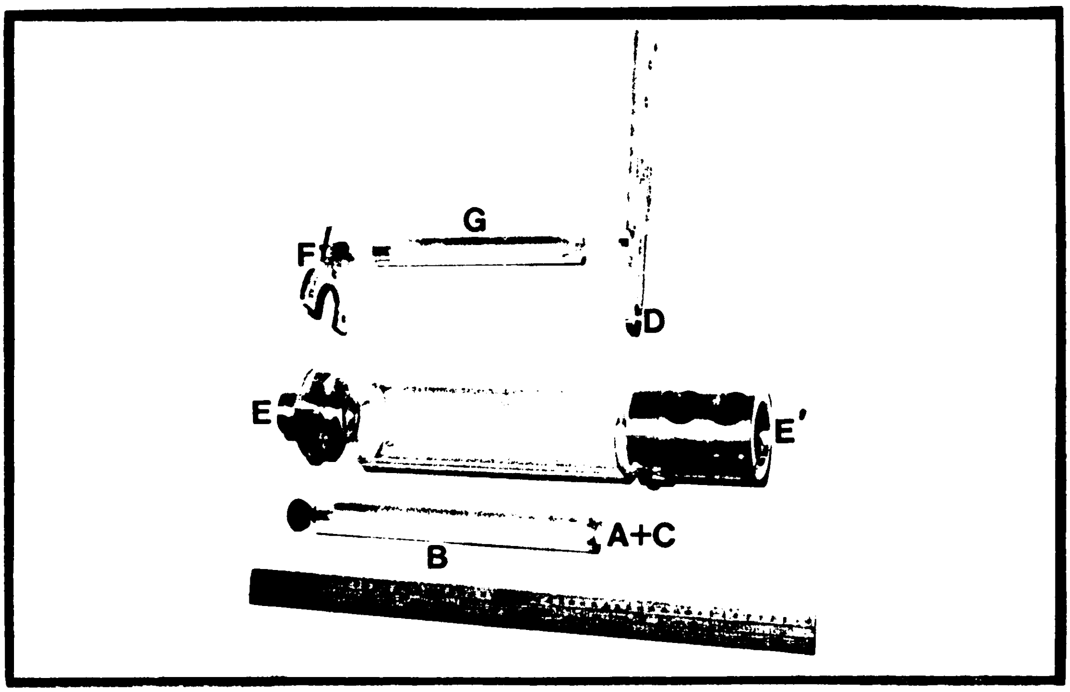

Fig. 5.3

Photograph of equipment used in determining physical properties of X-ray detectors

For the determination of the window to detector distance the source was fixed at position (A) behind a collimator (C) (with aperture D_s = 1 mm) to the piston (B). The piston is distance calibrated to define z and slides through the frame (E) which is clamped via a tube to (E') that fits tightly over the detector cap. When adapted for scanning the face of the detector (E) was clamped to support (F) which in turn was fixed to a precision X-Y vernier table. The piston could be varied to alter the distance u as needed but defined to an extent by the length of spacer (G) from the collimator (D). The source was thereby automatically aligned with the collimator having an aperture diameter of D_d = 0,2 mm.

Count rate and statistics are obviously determined by the distances v and u as well as the choice of aperture size of the collimators and source strength. The distances from source to detector and collimators were selected to maintain a constant effective beam spot size of 0,3 mm diameter on the detector crystal and corresponding count rate of approximately 1 kHz.

5.3 Results

Four X-ray detectors were studied, which included both intrinsic germanium (IG) and lithium drifted silicon (Si(Li)) detectors. These detectors were used routinely for different applications in the laboratory. The detectors used in this study are tabulated in Table 5.1 together with nominal physical parameters provided by the manufacturers.

Tabel 5.1

X-ray detectors used for study and nominal manufacturer provided parameters

#	Detector	Window-to-detector Distance (mm)	Active area (mm^2)	Sensitive depth (mm)
1	Si(Li) PGT	-	28	3
2	Si(Li) DSG	4	30	4
3	IG PGT 1	3,5	100	10
4	IG PGT 2	-	25	5

5.3.1 Sensitive depth of silicon detectors

The high energy intrinsic efficiencies of two silicon X-ray detectors (Si(Li) PGT, Si(Li) DSG) were obtained as a function of energy by using a variable fluorescent X-ray source having targets of Cu, Rb, Mo, Ag, Ba and Tb with associated K_α X-ray energies of 8,05; 13,39; 17,48; 22,16; 32,19 and 44,70 keV respectively. This efficiency response defines the sensitive depth of the detectors. The efficiencies of these detectors relative to an IG detector are plotted in Fig. 5.4 together with theoretical curves for sensitive thicknesses of 2 mm, 3 mm and 4 mm. The intrinsic efficiency of an IG detector is essentially unity at these energies, with the exception of the region between 11,1 keV and approximately 16 keV where it is less than 100 % due to escape peak effects as shown in Fig.5.1(b). The efficiencies of the silicon detectors were corrected for this drop in efficiency. Results were compared with nominal values as supplied by the manufacturers and it is clear that the Si(Li) DSG detector with nominal sensitive thickness of 4 mm was better represented by a value of 3 mm. The results for detector Si(Li) PGT compared favourably with the nominal value of 3 mm.

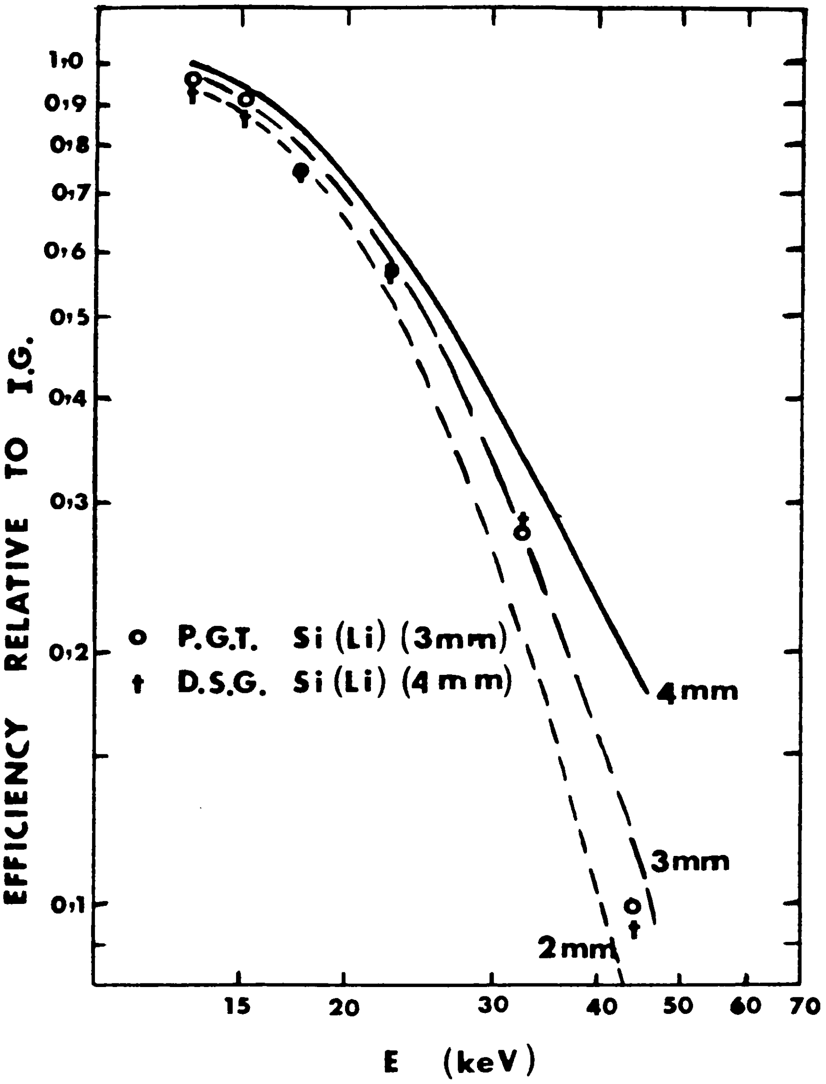

Fig. 5.4

Efficiencies of Si(Li) detectors relative to an IG detector

5.3.2 Distance from window to crystal

The technique described in 5.2.2 was applied to the four different X-ray detectors, with the results illustrated in

Figure 5.5 where data points are shown fitted to linear least squares fits. Coefficients of regression were typically 0,99. The distances for the different detectors 1, 2, 3 and 4 are 4,0 ± 0,2; 11,9 ± 0,3; 5,4 ± 0,2 and 4,0 ± 0,2 respectively. Errors quoted are based on a 90 % confidence limit.

When compared with nominal values supplied by the manufacturers in Table 5.1, these results show a major discrepancy in the case of detector Si(Li)DSG (11,9 mm compared with nominal 4 mm).

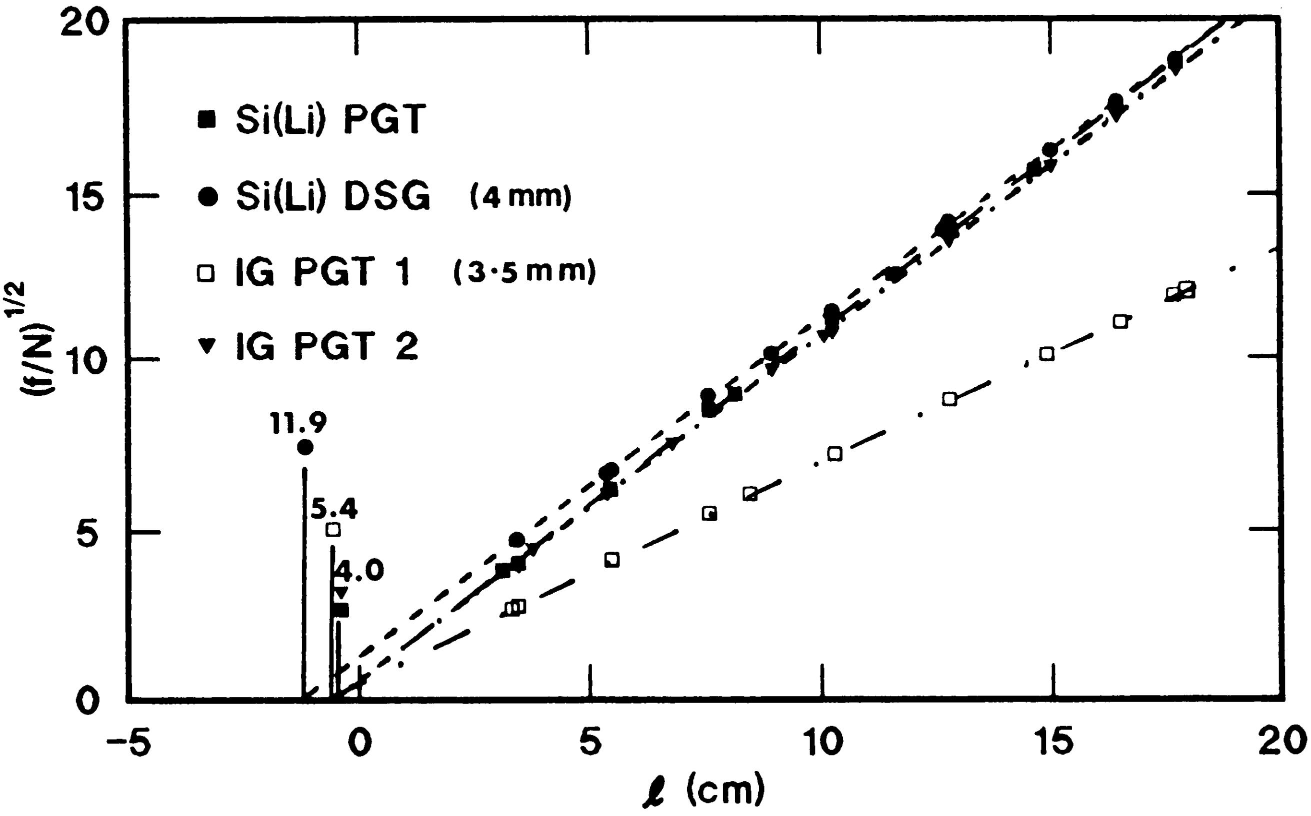

Fig. 5.5

Experimental results with straight lines fitted to window-detector distance measurement

5.3.3 Geometrical shape of detector

The relative X-Y spatial response of the detector as a function of position was determined and is illustrated in a three dimensional plot in Fig. 5.6 for detector 3 of Table 5.1. The sharp drop representing the edges of the crystal is a significant feature in these results, and from this the physical periphery of the detectors can be deduced. These measurements were made for all four detectors and the effective diameters of the detectors in two planes X and Y are shown in Fig. 5.7.

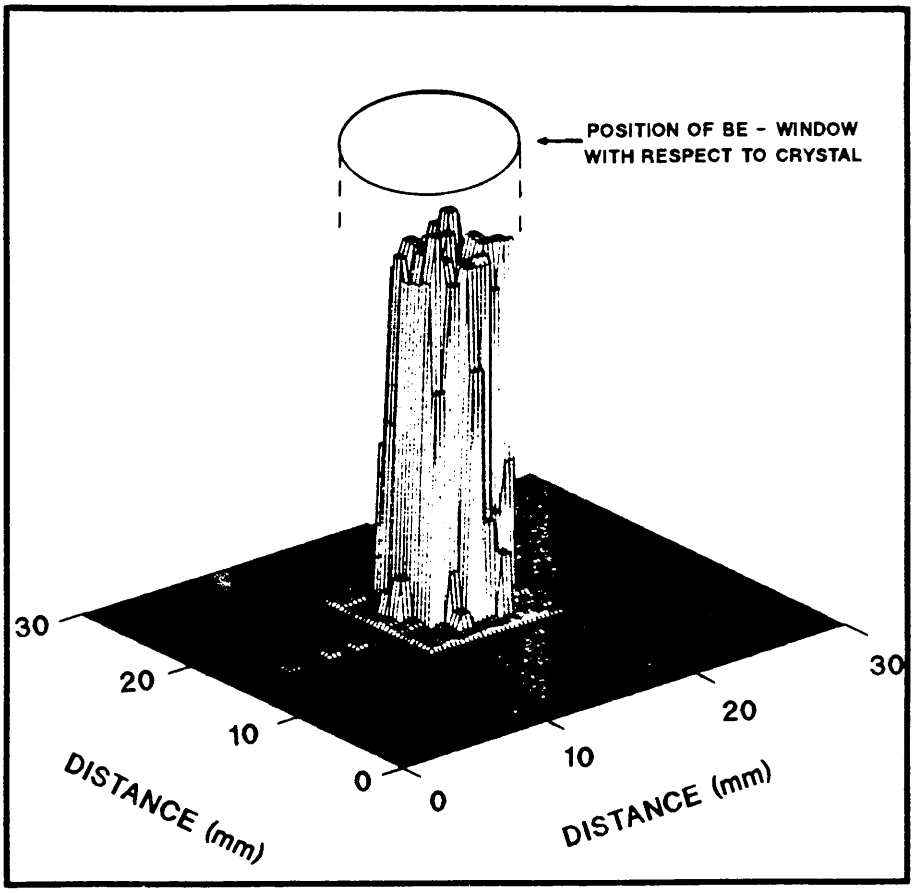

Fig. 5.6

3-D plot of response of detector as a function of position

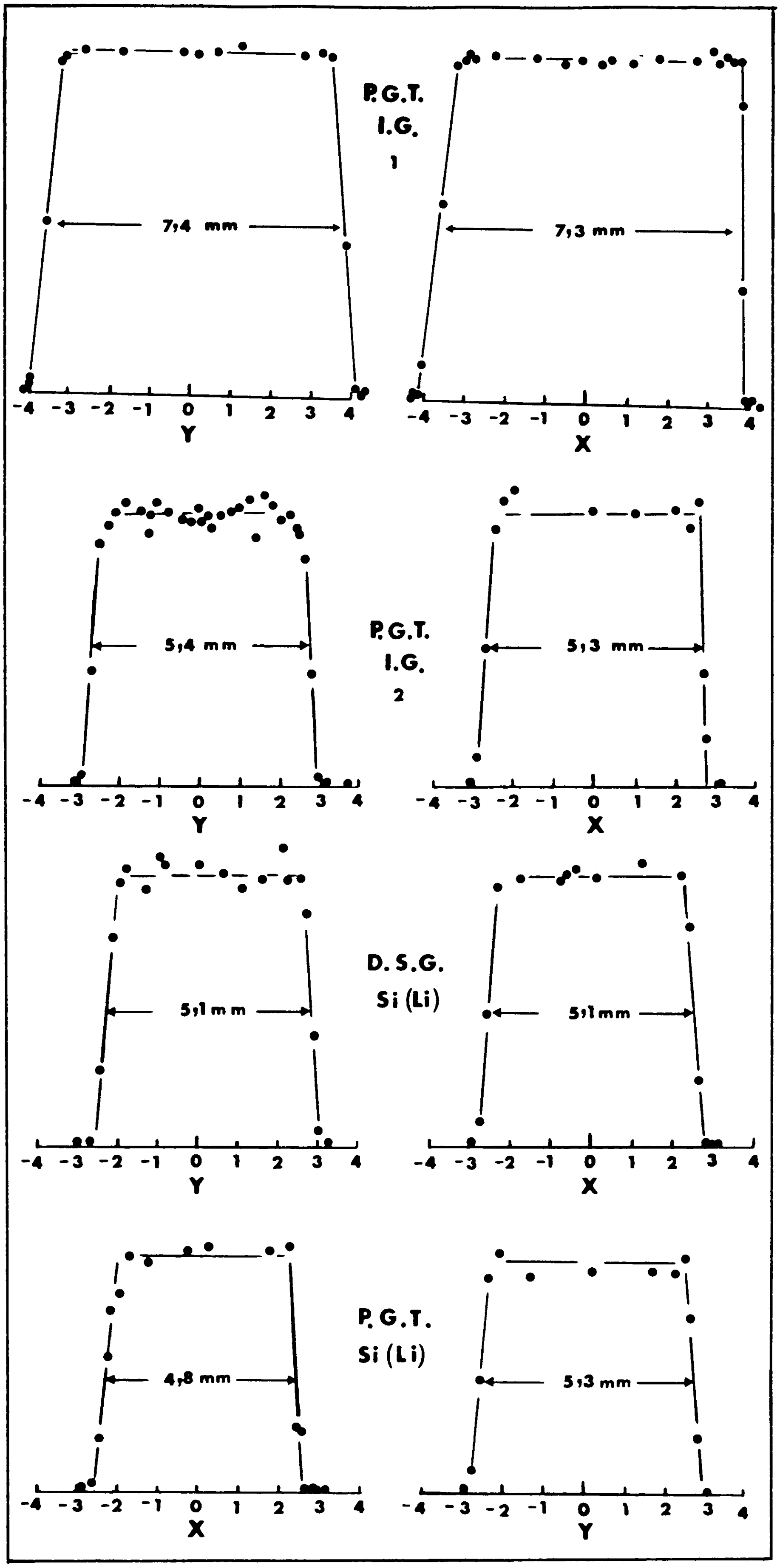

Fig. 5.7

Effective diameters of X-ray detectors in 2 planes

The results indicate that the physical geometry of the crystal is not necessarily circular. The differences in yield obtained in the plateau region were consistent within statistical errors, and thus no significant geometrical radial dependence was noted at outset in these cases, as was described in the measurement by Cohen et al[Co80].

The edges are defined by the position where the yield falls to half of the mean plateau value. A projection of edges onto the X-Y plane of Figure 5.6 allows the calculation of the active areas and shapes of these detectors. These effective sensitive shapes are illustrated in Fig. 5.8. Included in this figure are the manufacturer's nominal sensitive areas assuming perfect circular shapes. The comparison with nominal values reflected significant discrepancies in 3 of the 4 detectors tested and the sensitive area for detector 3 was found to be smaller by a factor 2 when compared with the manufacturer's specifications. Detector 3 was not run at full bias however, due to breakthrough problems owing to the age and associated neutron damage of this detector. All these scans showed however that the detectors were positioned centrally within 2 mm relative to the Be window position.

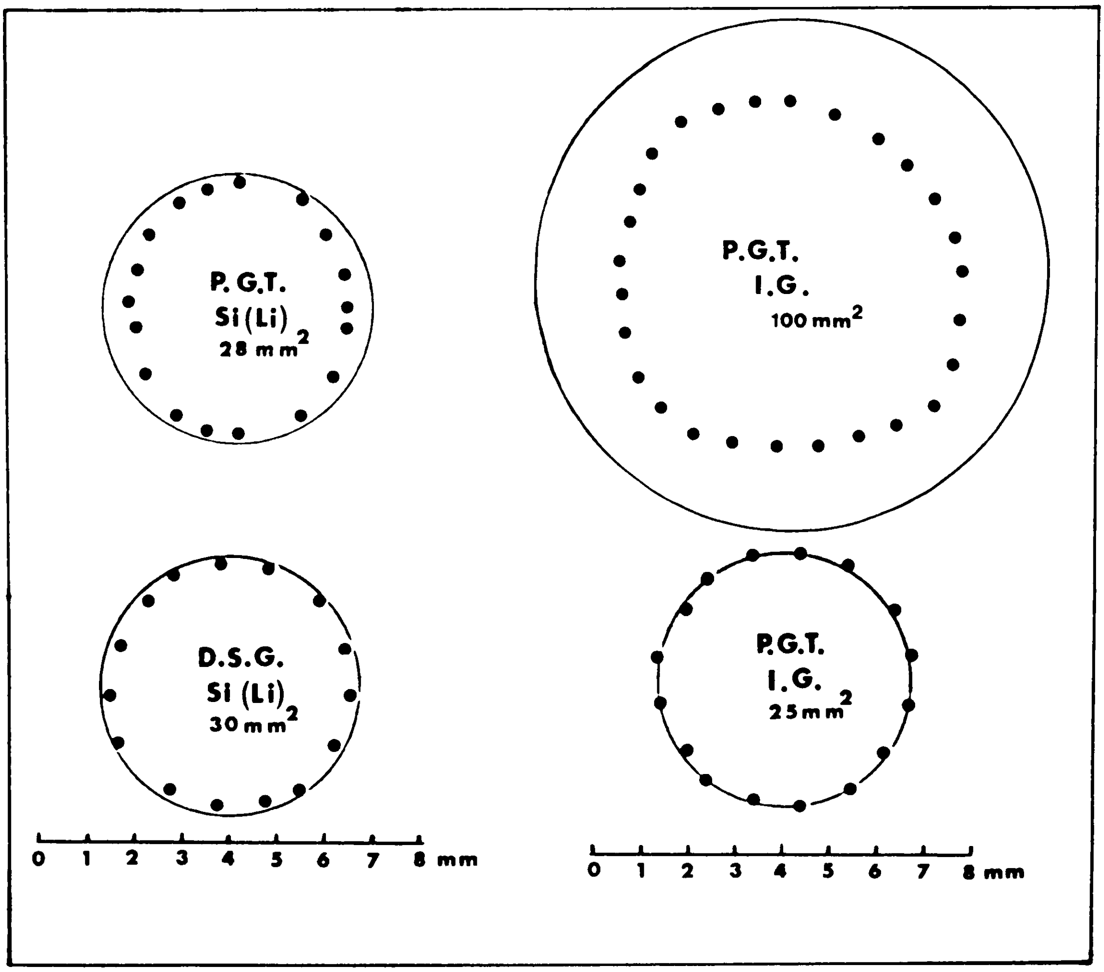

Fig. 5.8

Shape of active areas of four X-ray detectors

5.3.4 Charge collection efficiency in X-ray detectors

Detector 3, which was old, neutron damaged, and becoming steadily more defective, could not be operated at full bias voltage and was ideally suited to study spatially dependent charge collection characteristics. The energy spectrum responses obtained when scanning this detector face at different radial distances with a collimated photon beam are illustrated in Fig. 5.9. While the full energy peak remained well defined over the central region, it is obvious that the full charge collection efficiency has dropped significantly at a distance of 40 mm from the detector centre. When moving further outward more trapping of charged carriers occured and the low energy region was enhanced at the cost of the full energy (where full charged collection occurred) peak. The nominal area of 100 mm^2 corresponds to a diameter of 57 mm. At 60 mm from the centre of the crystal the physical edge of the crystal had not yet been reached, as there was some remnant response from the detector, although this response indicated only very limited charged collection and yield was only slightly higher than background yield.

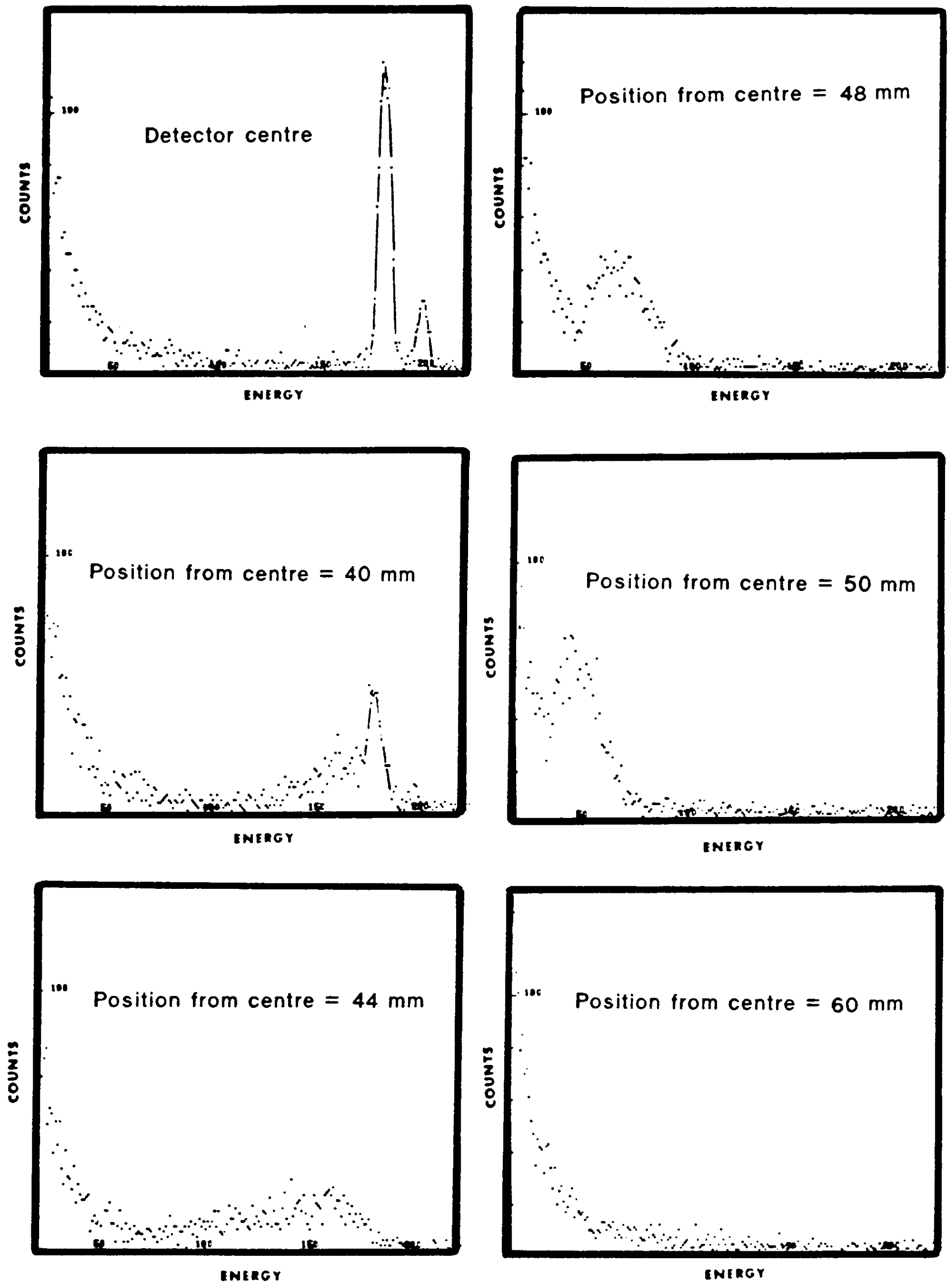

Fig. 5.9.

Charge collection efficiencies at different radial positions of IG X-ray detector number 3

Whereas the scanning measurements described in section 5.3.3 related only to the full energy peaks, it was appropriate in this case to choose a series of different energy regions and plot the yield obtained as a function of position. These results are shown in Fig 5.10 illustrating clearly the different components of the full energy range integrated yield where only the central plateau region can be used as a spectrometer.

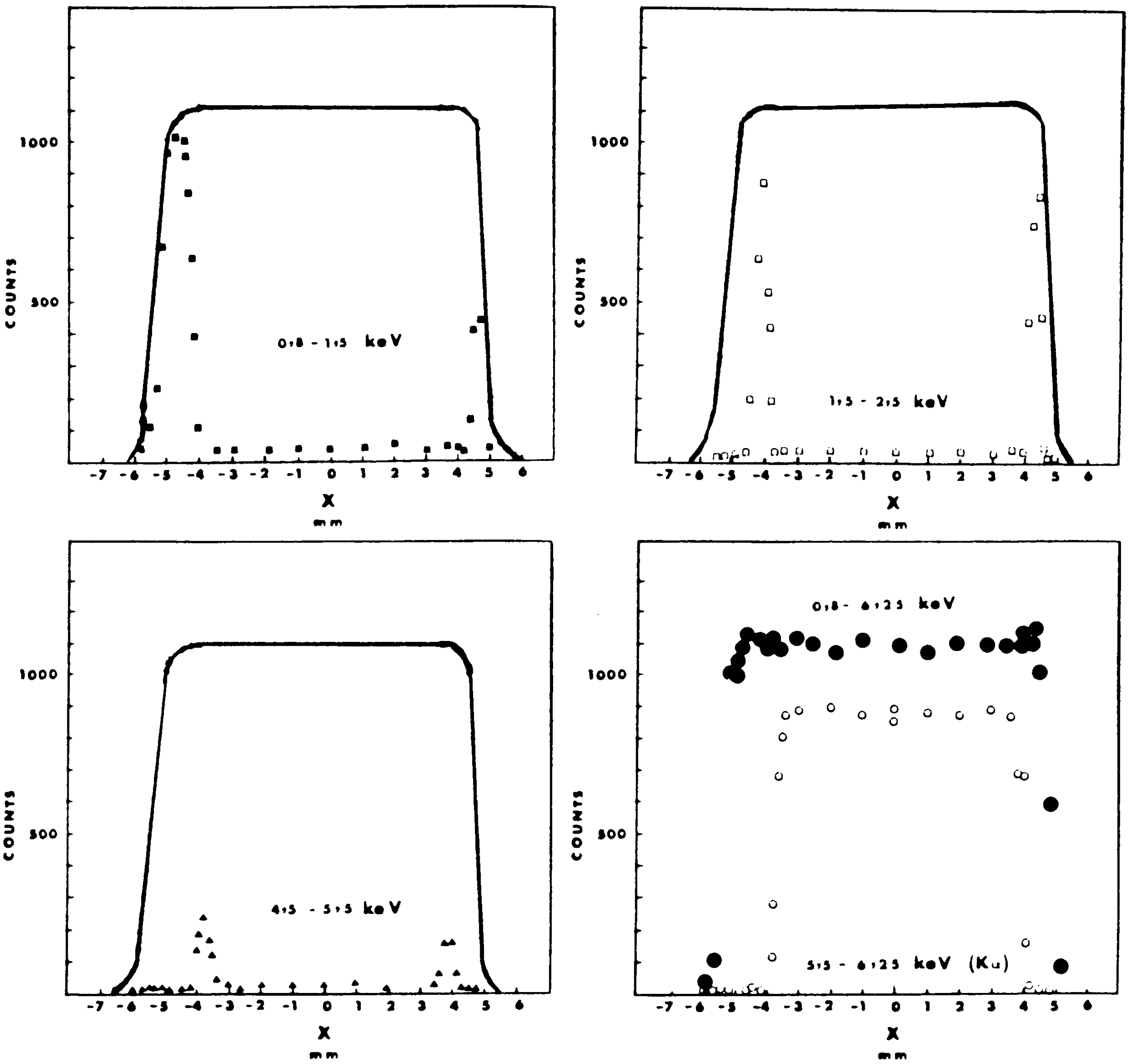

Fig. 5.10

Radial dependence of yield in different energy regions (■□▲○) compared with the integrated yield (solid line and ●)

The onset of non-complete charge collection in the energy region immediately below the full energy peak approximately 4 cm from the centre of the crystal is obvious, and this feature became more enhanced in the lower energy regions as the edge of the detector was reached. This indicates the importance of collimating of photon beams impinging on such X-ray detectors.

5.3.5 Summary of results

The results obtained from the various measurements discussed are summarised in Table 5.2.

Table 5.2

Physical properties of X-ray detectors

#	Detector	Distance:window-detector			Active area (mm^2)			Sensitive depth (mm)		
		Measured	Nominal	Diff.	Measured	Nominal	Diff.	Measured	Nominal	Diff
1	Si(Li)PGT	4,0±0,2	-	-	23,1±1,0	28	4,9	3	3	-
2	Si(Li)DSG	11,9±0,3	4	7,9	26,4±1,0	30	3,6	3	4	1
3	IG PGT(1)	5,4±0,2	3,5	1,9	51 ±3	100	-	-	-	-
4	IG PGT(2)	4,0±0,2	-	-	25,5±1,0	25	0,5	-	-	-

5.4 CONCLUSION

Spatial response properties of two silicon and two germanium X-ray detectors were measured and showed deviations, in many instances, from the specifications of the manufacturers. In general a smooth relative response was measured across the whole sensitive area of each detector with well defined edges. Radial dependence of efficiency was detected in one case relating to incomplete charge collection anomalies at the edges of the crystal. The drop in response at the edges of detector crystals was used to obtain the effective shapes and areas of the detectors.

The sensitive depths of the two silicon detectors were measured by comparing with the corresponding yield from an IG detector assuming the latter to be 100 % efficient in the energy range from 8 to 50 keV when corrected for escape characteristics.

In these measurements it was confirmed that the nominal values of physical parameters of X-ray detectors used as given by manufacturers were not necessarily accurate, that conventional acceptance of a circular sensitive area is far from wise, and that parameters should be measured experimentally as a routine check to monitor also detector degradation.

REFERENCES

Ad69 - F Adams and R Dams - J. Radioanal. Chem. 3(1969)99.

Ai62 - J H Aitken and W R Dixon - Phys. Letters 2(1962)152.

An71 - H R Andrews et al - AECL 3912(1971)35

An77 - H H Anderson and J F Ziegler - The stopping and ranges of ions in matter. Vol. 3 1977. Publ. Pergamon Press.

Ax65 - R C Axtmann and D Kedem - Nucl. Instr. and Meth. 32(1965)70.

Ba84 - K M Barfoot et al - Nucl. Instr. and Meth. B5(1984)534

Bi65 - P G Bizzeti et al - Nucl. Instr. and Meth. 34(1965)261.

Bo48 - J C Bowe et al - Phys. Rev. A73(1948)1219

Br84 - G Braun, A Bockisch and W Neuwirth - Nucl. Instr. and Meth. 224(1984)112

Ca84 - J L Campbell, R G Leigh and W J Teesdale - Nucl.Instr. and Meth. B5(1984)39

Ca86 - J L Campbell and P L McGhee - Nucl. Instr. and Meth. A248(1986)393

Co62 - L Colli et al - Phys. Letters 2(1962)12.

Co62A - L Colli et al - Phys. Letters 1(1962)120

Co63 - L Colli et al - Nucl. Phys. 43(1963)529.

Co80 - D D Cohen - Nucl. Instr. and Meth. 178(1980)481

Da88 - W Dabrowski and K Korbel - Nucl. Instr. and Meth. A271(1988)585

De79 - K Debertin - Nucl. Instr. and Meth. 158(1979)479.

Dr74 - J E Draper, N S P King and W G Wyckoff - Phys. Rev. 9(1974)948

Ei68 - E Eichler, P H Telson and J K Dickens - Nucl. Phys. A120(1968)622

En78 - P M Endt and C van der Leun - Nucl. Phys. A310(1978)240.

Er60 - T Ericson - Adv. in Phys. 9(1960)425.

Fi85 - E C Finch - Nucl. Instr. and Meth. 228A(1985)402.

Ge77 - R J Gehrke, R G Helmer and R C Greenwood - Nucl. Instr. and Meth. 147(1977)405

Gi74 - D R Gill et al - Nucl. Phys. A229(1974)397

Gr69 - S M Grimes - Nucl. Phys. A124(1969)369.

Gr85 - P W Gray and A Ahmad - Nucl. Instr. and Meth. A237(1985)577

Gu60 - E M Gunnerson and G James - Nucl. Instr. and Meth. 8(1960)173.

Ha73 - J S Hansen et al - Nucl. Instr. and Meth. - 106(1973)365

He78 - H Henschel and R Schmidt - Nucl. Instr. and Meth. 151(1978)529.

Hn79 - V Hnatowicz - Nucl. Instr. and Meth. 161(1979)151.

Ie72 - IEEE Standard 325-1971 - "Test Procedures for Germanium Gamma Ray Detectors" (ANSI N42.8 - 1972).

Il84 - K Ilakovac, V Horvat and N Ilakovac - Nucl. Instr. and Meth. 228(1984)210

Ja77 - Japan Progress Report NEANDC (J) - 51/u, September 1977

Jä87 - B Jäckel, W Westmeier and P Patzelt - Nucl. Instr. and Meth. A261(1987)543

Ka74 - S B Kaufmann et al - Nucl. Instr. and Meth. 115(1974)47

Ke55 - H W Kendall and M Deutsch - 36th Prog. Rep., Lab. for Nucl. Sci. MIT AECU - 3021(1955)51

Kr56 - J J Kraushaar, E Brun and W E Meyerhof - Phys. Rev. 101(1956)139

La76 - "Laboratoire de Métrologie des Rayonnements Ionisants" - Commissariat à l'Energie Atomique 25 March 1976.

Le78 - C M Lederer and V S Shirley - Table of Isotopes - Seventh edition 1978.

Li63 - J Lindhart, M Scharff and H E Schiott - Mat. Fys. Medd. 33 no. 14 (1963).

Li69 - D Lister and A B Smith - Phys. Rev. 183(1969)954

Li73 - H Liskien and A Paulsen - Nucl. Data Tables 11 - (1973)569.

Ma68 - I G Main et al - Phys. Lett. 26B(1968)295

Ma69 - P Marmier and E Sheldon - Physics of Nuclei and Particles, Volume I, 1969, Academic Press.

Mc49 - F K Mcgowan, S de Benedetti and J E Francis - Phys. Rev. 75(1949)1761

Me78 - R A Meyer - Lawrence Livermore Laboratory Report M-100 (1978)

Mi67 - R G Miller and R W Kavanagh - Nucl. Instr. and Meth. 48(1967)13.

Mi71 - D W Mingay, J P F Sellschop and P M Johnson - Nucl. Instr. and Meth. 94(1971)497.

Mi83 - D W Mingay and J P F Sellschop - S. Afr. J. Phys. 6(1983)51.

Mo60 - J Monahan - Fast neutron physics Part 1, Chapter 1.B. J B Marion and J C Fowler, Eds. IPI, New York (1960).

Mo66 - H Morgenstern, D Hilscher and J Scheer - Nucl. Phys. 83(1966)369.

Mo66A - H Morgenstern, D Hilscher and J Scheer - Nucl. Instr. and Meth 39(1966)347.

Mo78 - J B Moulton et al - Nucl. Instr. and Meth. 157(1978)325.

Ne76 - Neutron Cross Sections - BNL Vol II Jan 76.

Of88 - R Ofek, A Tsechanski and G Shani - Nucl. Instr. and Meth. A268(1988)229

Ro66 - J C Robertson and K J Zieba - Nucl. Instr. and Meth. 45(1966)179.

Sa65 - A R Sattler - Phys. Rev. 138(1965)A1815.

Sa87 - A F Sànchez-Reyes et al - Nucl. Instr. and Meth B28(1987)123

Sc69 - D G Schuster - Nucl. Instr. and Meth. 76 (1969)35.

Sh79 - K Shima - Nucl. Instr. and Meth. 165(1979)21

St78 - "Standard Method of Calibration of Germanium Detectors for Measurement of Gamma-ray Emission Rates of Radionuclides" - ASTM Designation : E522-78 p1106.

Ts84 - A Tsechanski and G Shani - Nucl. Sci. Eng. 89(1984)189

Wa72 - G Wallace and G J McCallum - Nucl.Phys. A184(1972)166.

Wa86 - E K Warburton and D E Alburger - Nucl. Instr. and Meth. A253(1986)38.

Wi71 - B D Wilkins et al - Nucl. Instr. and Meth. 92(1971)381.

Yo80 - Y Yoshizawa et al - Nucl. Instr. and Meth. 174(1980)133.